FACULTÉ DES ÉTUDES SUPÉRIEURES ET POSTOCTORALES

uOttawa

L'Université canadienne
Canada's university

FACULTY OF GRADUATE AND POSDOCTORAL STUDIES

Laura Elizabeth Downie
AUTEUR DE LA THÈSE / AUTHOR OF THESIS

M.Sc. (Physics)
GRADE / DEGREE

Department of Physics
FACULTÉ, ÉCOLE, DÉPARTEMENT / FACULTY, SCHOOL, DEPARTMENT

Pathways to Recovering Single-Bonded Nitrogen at Ambient Conditions: High Pressure Studies of Molecular and Ionic Azides

TITRE DE LA THÈSE / TITLE OF THESIS

Serge Desgreniers
DIRECTEUR (DIRECTRICE) DE LA THÈSE / THESIS SUPERVISOR

CO-DIRECTEUR (CO-DIRECTRICE) DE LA THÈSE / THESIS CO-SUPERVISOR

Zibgniew Stadnik

Ravi Bhardwaj

David Sinclair

Gary W. Slater
Le Doyen de la Faculté des études supérieures et postdoctorales / Dean of the Faculty of Graduate and Postdoctoral Studies

Pathways to Recovering Single-Bonded Nitrogen at Ambient Conditions: High Pressure Studies of Molecular and Ionic Azides

Laura E. Downie

Thesis submitted to the
Faculty of Graduate and Postdoctoral Studies
In partial fulfillment of the requirements for the degree of
Master of Science in Physics

Department of Physics
Faculty of Science
University of Ottawa

Library and Archives Canada

Published Heritage Branch

395 Wellington Street
Ottawa ON K1A 0N4
Canada

Bibliothèque et Archives Canada

Direction du Patrimoine de l'édition

395, rue Wellington
Ottawa ON K1A 0N4
Canada

Your file Votre référence
ISBN: 978-0-494-74182-5
Our file Notre référence
ISBN: 978-0-494-74182-5

NOTICE:

The author has granted a non-exclusive license allowing Library and Archives Canada to reproduce, publish, archive, preserve, conserve, communicate to the public by telecommunication or on the Internet, loan, distribute and sell theses worldwide, for commercial or non-commercial purposes, in microform, paper, electronic and/or any other formats.

The author retains copyright ownership and moral rights in this thesis. Neither the thesis nor substantial extracts from it may be printed or otherwise reproduced without the author's permission.

AVIS:

L'auteur a accordé une licence non exclusive permettant à la Bibliothèque et Archives Canada de reproduire, publier, archiver, sauvegarder, conserver, transmettre au public par télécommunication ou par l'Internet, prêter, distribuer et vendre des thèses partout dans le monde, à des fins commerciales ou autres, sur support microforme, papier, électronique et/ou autres formats.

L'auteur conserve la propriété du droit d'auteur et des droits moraux qui protège cette thèse. Ni la thèse ni des extraits substantiels de celle-ci ne doivent être imprimés ou autrement reproduits sans son autorisation.

In compliance with the Canadian Privacy Act some supporting forms may have been removed from this thesis.

While these forms may be included in the document page count, their removal does not represent any loss of content from the thesis.

Conformément à la loi canadienne sur la protection de la vie privée, quelques formulaires secondaires ont été enlevés de cette thèse.

Bien que ces formulaires aient inclus dans la pagination, il n'y aura aucun contenu manquant.

Canada

Abstract

Working towards the goal of recovering single-bonded nitrogen at ambient conditions, the approach taken in this work is to subject nitrogen-rich molecular and ionic azides (specifically, cyanuric triazide and ammonium azide) to high pressures to induce transitions to phases that contain single-bonded nitrogen. The samples were subjected to extreme pressures using a diamond anvil cell and subsequently studied using high-resolution synchrotron powder x-ray diffraction and vibrational Raman spectroscopy. The experimental results indicate that both cyanuric triazide and ammonium azide undergo a pressure-induced first order structural phase transition at 30 and 3.0 GPa, respectively. The analyses and characterizations of these dense energetic materials are discussed in detail, and will be used to explore the possibility of recovering single-bonded nitrogen at ambient conditions.

Statement of Originality

To the best of my knowledge, I certify that the research presented in this thesis is the original work of the author. Any contributions to this work made by others with whom I have worked are expressly indicated and acknowledged in the text.

Acknowledgements

First of all, I would like to thank Prof. Serge Desgreniers for his supervision over the past two years, and for giving me the opportunity to work on such a dynamic and interesting project.

I would also like to thank Dr. Ning Chen and Dr. Chang-Yong Kim, Hard X-ray MicroAnalysis beamline scientists at the Canadian Light Source for their help in carrying out x-ray diffraction experiments.

Of course there wouldn't have been much of a project if we didn't have the right starting materials. In this regard, I would like to acknowledge Prof. Muralee Murugesu (University of Ottawa, Department of Chemistry) and his graduate student Didier Savard for the chemical synthesis of cyanuric triazide and ammonium azide.

Heading up this project were Dr. Anguang Hu and Dr. Fan Zhang (Defence Research and Development Canada - Suffield) whose seemingly endless enthusiasm is certainly contagious. The theoretical calculations performed at DRDC not only provided the motivation for this work, but significantly helped in the interpretation of the experimental results. Their willingness and eagerness to help is certainly appreciated.

Last, but undoubtedly not least, I would like to sincerely thank my colleague Dr. Jesse Smith. If I ever needed anything or just had a "quick" question, he always made the time to help and was always happy to do so. For his many insights, his camaraderie during the long night shifts at the CLS, his incredible patience, and of course, for bringing humour to the lab, thank you does not begin to cover it, but it's a start. Thank you.

Table of Contents

List of Figures

List of Tables

Nomenclature

AA	ammonium azide
B_0	bulk modulus
B_0'	pressure derivative of bulk modulus
cg	cubic gauche
CL-20	hexanitrohexaazaisowurtzitane
CLS	Canadian Light Source
CTA	cyanuric triazide
d	spacing between lattice planes
DAC	diamond anvil cell
EDS	energy-dispersive x-ray spectroscopy
EOS	equation of state
f	compression
F	Helmholtz free energy
G	Gibb's free energy
HMX	1,3,5,7-tetranitro-1,3,5,7-tetraazacyclooctane
HXMA	Hard X-ray MicroAnalysis
I_{hkl}	intensity of (*hkl*) diffraction peak
λ	wavelength
P	pressure
PN	polymeric nitrogen
pXRD	powder x-ray diffraction
RDX	1,3,5-trinitrohexahydro-*s*-1,3,5-triazine
S	entropy

S_{hkl}	structure factor
SEM	scanning electron microscope
θ	angle of incidence/reflection
T	temperature
TNT	trinitrotoluene
TTZ	trans-2-tetrazene
V	volume
XRD	x-ray diffraction

Chapter 1

Introduction

The study and development of highly energetic materials has challenged scientists ever since the reported discovery of black powder by the Chinese in 200 AD. This simple mixture of saltpeter potassium nitrate (KNO_3), charcoal and sulfur has even been credited as one of the major inventions that marked the end of the Middle Ages. The current image of energetic materials that one might picture includes TNT or C-4 (whose active ingredient is known as RDX). However, given recent developments, a new class of materials based on polymeric nitrogen may soon take a leading role.

In its natural form, molecular nitrogen (N_2) is characterized by an extremely strong covalent triple bond. Under extreme pressure and temperature conditions ($P>110$ GPa, $T>2000$ K), a single-bonded form of nitrogen exists known as polymeric nitrogen (PN). There is an immense amount of energy stored in this single-bonded form (about 5 times as much as the current best energetic material) such that, if PN could be retained to ambient conditions, this energy could be readily released and harnessed upon the transformation back to molecular N_2. However, on reducing from the extreme synthesis conditions, it has been found that PN can only be retained to 42 GPa. Therefore, if single-bonded nitrogen is to be recovered at ambient conditions (room temperature and pressure), it will instead have to be part of a high nitrogen content material.

One class of such materials with substantial promise is based on the azide (N_3^-) anion (a linear chain formed from three nitrogen atoms linked together by what are essentially double bonds). It has been shown that by subjecting these azides (which are themselves energetic materials) to *extreme external pressures, structural transitions can occur to phases in which single-bonded* nitrogen is present. To that end, the present work examines the effect of pressure on two specific azides: cyanuric triazide, C_3N_{12}, and ammonium azide, NH_4N_3. The molecular structures of these two compounds are given below in Figure 1.1.

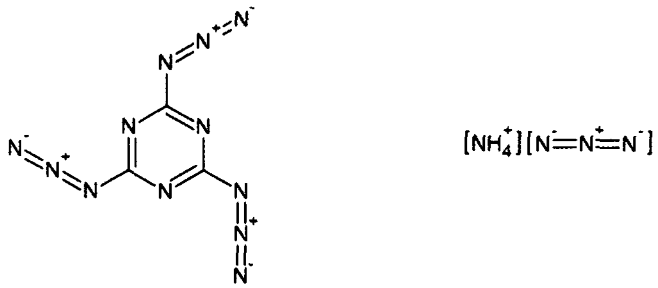

Figure 1.1: Molecular structures of the two azides studied in this work: cyanuric triazide (left) and ammonium azide (right).

By performing high pressure Raman spectroscopy and powder x-ray diffraction experiments on cyanuric triazide and ammonium azide, any changes in bonding arrangement (e.g., increased intramolecular interaction, or the formation of single-bonded nitrogen network) or changes in atomic structural arrangement (i.e., phase transitions) will be easily identified and characterized.

To generate the high pressures required for these experiments, a diamond anvil cell was used. At the heart of the cell are two opposed diamond anvils. Diamond is extremely hard and optically transparent so it can generate high pressures while providing near unobstructed access to the sample being studied. By applying a small force over a large area and concentrating it to a small area in contact with the sample, very high pressures can be achieved – as high as those in the core of the Earth. In order to facilitate the discussion of such large pressures, the unit used throughout this work is the gigapascal (GPa), which is roughly equal to 10,000 times atmospheric pressure. For a sense of scale, the diamond anvil cell, which is only about 5 cm in diameter and easily fits in the palm of one's hand, can easily attain 100 GPa, or one million times atmospheric pressure.

One technique used to study the sample material inside the cell and identify phase transitions is vibrational Raman spectroscopy, where if there is any discontinuity in the pressure evolution of a compound's characteristic vibrational frequencies, it would indicate a change in molecular bonding. Thus, Raman spectroscopy can relatively quickly provide an overview of the behaviour of the sample with increased pressure and identify structural phase transitions.

The structures and properties of these phases are then fully characterized using the technique of x-ray diffraction. In this work, all of the x-ray diffraction experiments were done using polycrystalline (powder) samples, were collected as a function of 2θ (angle-dispersive), and were performed using synchrotron radiation at the Hard X-ray MicroAnalysis (HXMA) 06ID-1 beamline at the Canadian Light Source (CLS).

Chapter 2

Literature Review and Motivation

The following chapter will present an introduction to energetic materials, followed by a pertinent literature review of the quest to synthesize and recover single-bonded nitrogen. The motivations for studying cyanuric triazide and ammonium azide will also be presented, along with an introduction of the thermodynamics behind studying materials at high external pressures and how it can be used to extract certain properties of the material.

2.1 Energetic Materials

2.1.1 A brief introduction to energetic materials

Energetic materials form a broad family of materials which store vast amounts of chemical energy that can be controlled relatively easily. Their primary purpose is to quickly release that energy upon ignition (i.e., detonate), and are thus of distinct military and industrial interest. The most common and widely used modern energetic materials generate their energies through the oxidation of their carbon backbone. Examples of these include nitroglycerine, TNT (trinitrotoluene), HMX (1,3,5,7-tetranitro-1,3,5,7-tetraazacyclooctane), and RDX (1,3,5-trinitrohexahydro-*s*-1,3,5-triazine); the molecular structures of which are given in Figure 2.1. More recently, two new classes of energetic materials have emerged, those which derive their energy from ring or cage strain (CL-20 (hexanitrohexaazaisowurtzitane), for example), and those with very large nitrogen contents (up to 85% N). The latter possess very high heats of formation due to their large number of inherently energetic N-N and C-N bonds.

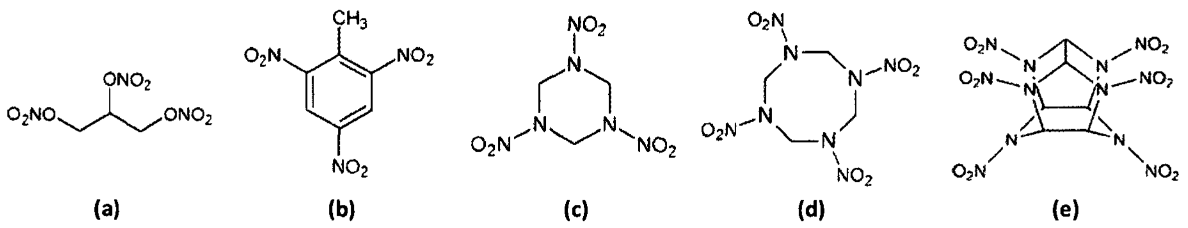

Figure 2.1: Molecular structure of some commonly used energetic materials: (a) nitroglycerine, (b) TNT, (c) RDX, (d) HMX, and (e) CL-20

2.1.2 Development of new energetic materials

The development of new energetic materials is a very active and constantly evolving field, and the resulting products have certainly come a long way since the invention of black powder. The main driving force of this field is to increase the performance of energetic materials, a property that depends on many factors, most of which are intrinsically related to their crystalline structures [1]. One key performance benchmark is the detonation velocity. Since to first order, this velocity is proportional to the density [1], the densest material is preferred. Furthermore, the use of a dense material ensures the most efficient use of the available space. This has spurred the development of a wide variety of other high density materials including caged nitramine compounds, such as CL-20 (Figure 2.1e), as these multicyclic compounds can achieve much higher densities than their monocyclic counterparts [2].

In addition to increased performance, new energetic materials have taken environmental concerns into consideration. The current energetic materials and their detonation products have proven to be quite toxic [3 - 5], which has been attributed to the presence of organo-nitro (C-NO_2) groups [6]. Therefore, a large number of newly reported energetic materials have high nitrogen contents (up to 85%) and derive their energy from their bonds instead of relying on these toxic nitro groups. By using nitrogen-rich compounds, the primary by-product of detonation becomes molecular N_2, a harmless gas, minimizing the release of environmentally hazardous compounds. Many of these high nitrogen content energetic materials are based on tetrazoles; a class of organic compounds characterized by a five-member heterocycle with a single carbon atom and four nitrogen atoms with intrinsically energetic bonds. While there are many reports of these tetrazole-based energetic materials (see references [7 - 13] and references therein for recent examples), it has yet to be seen if they will ever replace the currently used nitramine-based materials.

This type of tetrazole-based chemical synthesis approach is typically based on deductive reasoning as to how the chemical composition and bonding will affect the overall material properties. This can be a real trial-and-error exercise, but modern computing capabilities have made numerous and significant contributions to this process. There is a unique symbiosis between the synthetic chemists and theoreticians; the theoreticians can first identify possible candidates with desirable properties that the experimentalists can then create, or a newly synthesized material can then be computationally analyzed to determine its value as an energetic material. Excellent and comprehensive reviews of these synthetic techniques and the resulting products are beyond the scope of this discussion, but can be found in references [14 - 17], for example.

2.1.3 Energetic materials at extreme conditions

Studying energetic materials at high pressures (P) and/or temperatures (T) has become increasingly important as these P,T conditions (up to 50 GPa and 6000 K [1]) are frequently seen during the detonation processes. The experimental data collected at these conditions can be used to verify and improve the accuracy of theoretical models of the behaviour of energetic materials. This in turn can lead to better predictive capabilities, reducing the time and cost associated with the production of new materials.

Exploring the P,T phase diagrams of these materials is also of great value. Many of the properties of energetic materials are dependent on their structure, and so by identifying and characterizing the different crystalline structures (polymorphs), it may be found that some have more desirable properties (e.g., higher density) than others. By thermodynamically synthesizing specific polymorphs, the performance of a material can be easily tuned. As an example, only one polymorph of HMX is permitted to be used in munitions, the other three crystalline forms are too sensitive and can easily detonate unintentionally [18]. Having control over pressure and temperature can also be used to affect the stability of a material. During transitions between polymorphs, defects can form within the crystal, and as the number of defects increases, the material becomes less stable. By repeatedly cycling through a phase transition, one can make the material very sensitive and easy to initiate; again allowing for the fine-tuning of energetic materials [18].

2.2 Single-Bonded Nitrogen

In its natural form, molecular nitrogen (N_2) is an inert diatomic gas characterized by an exceptionally strong and stable triple covalent bond. It is of particular interest as an energetic material due to the distinctively large difference between the N-N single bond (160 kJ/mol) and the N≡N triple bond (954 kJ/mol) [19], such that if a metastable allotrope of nitrogen exists with an extended single-bonded network, it would be able store an incredible amount of energy (158 kJ/mol, or 2.3 eV/atom). This proposed high energy density material would have the highest energy content of any known nonnuclear material [20]. Upon release of this energy, the only by-product would be molecular nitrogen; making it a compact, environmentally friendly high energy density material which would be ideally suited as rocket fuel or a propellant, for example. The prospect of harnessing such a "green" and near-ideal energetic material presents a major research motivation.

2.2.1 Theoretical predictions of polymeric nitrogen

In 1985, it was predicted by McMahan and LeSar [21] that by subjecting N_2 to large external pressures, the intramolecular interaction between nitrogen atoms could become competitive with the intermolecular interactions, which would allow for the formation of a three-dimensional single-bonded nitrogen network (commonly known as polymeric nitrogen, or PN for short). This diatomic-to-monatomic transition was calculated to occur below 100 GPa, well within the available experimental capabilities (namely, diamond anvil cell techniques). This original calculation predicted a metallic simple cubic structure for the single-bonded form; however, it was subsequently shown to be an unstable structure [22].

In 1992, extensive local density functional total-energy calculations using nonlocal *ab initio* pseudopotentials were performed by Mailhiot *et al.* [23] for both polymeric and molecular phases of nitrogen. The candidate structures were based on the high pressure-stabilized phases seen in the heavier group-V elements (phosphorus, arsenic, antimony, and bismuth) [24 - 27]; simple cubic (sc), or rhombohedral distorted simple cubic (A7). Two other distortions to the simple cubic structure were used as candidate structures: an orthorhombic distortion as seen in the ambient black-phosphorus (BP) phase of phosphorus, and a cubic gauche (cg) distortion characterized by all gauche (~60°) dihedral angles. The fully optimized cg phase was found to be the lowest-energy structure of the proposed polymeric forms as shown in Figure 2.2, and was predicted to become thermodynamically stable at a transition pressure of 50±15 GPa. The stability of this unusual cubic gauche structure of nitrogen (cg-N, space group $I2_13$) was confirmed by several theoretical studies and its properties were extensively computationally predicted [28 - 32].

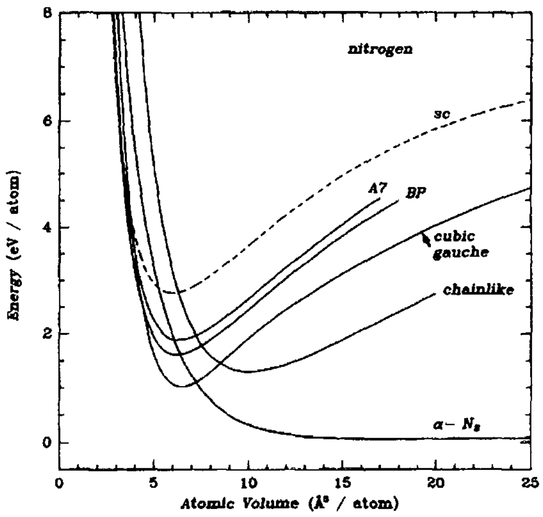

Figure 2.2: Calculated total energies per atom for several candidate structures of single-bonded nitrogen compared to molecular nitrogen, showing the stability (lowest energy) of the cubic gauche structure at small atomic volumes (high pressures). Figure reprinted from ref. [23].

2.2.2 Experimental confirmation

Almost immediately after the original predictions were published, experimentalists got to work in searching for this polymeric phase of nitrogen. Pure nitrogen was taken up to pressures of 140 GPa [33] and 180 GPa [34] at ambient temperature, far above the predicted transition pressure of 50±15 GPa, but both failed to indicate the presence of a single-bonded network. As pressure was increased the samples went opaque, but they retained the characteristic vibrational Raman band associated with the stretching mode of molecular nitrogen. It was hypothesized that the molecular phase has a large hysteresis and is metastable up to these high pressures, a phenomenon which is quite common for covalent solids [35].

The first instance of a transformation to a nonmolecular form of nitrogen was realized in 2000 by Goncharov *et al.* [36] and was later confirmed by Eremets *et al.* in 2001 [37]. This transformation occurred at 190 GPa and low temperatures (80 - 300 K), and was marked by the disappearance of the molecular nitrogen vibrational mode. Optical studies of this nonmolecular phase indicated that it is amorphous [36 - 38] and first-principles calculations identified the structure as a disordered network of single- and double-bonded nitrogen atoms [32, 38]. While not the predicted polymeric phase, it was certainly a significant step in the right direction.

The first successful experimental synthesis of nitrogen with an extended single-bonded covalent network was reported in 2004 by Eremets *et al.* [39]. Pure molecular nitrogen was studied in a specially designed diamond anvil cell. The pressure on the sample was increased to 140 GPa at ambient temperature and the sample was observed to have darkened (now known to be the nonmolecular η phase of nitrogen [40]). The sample was subsequently heated using a laser heating arrangement combined with a 1 μm thick boron plate inside the sample chamber to act as an absorber of the incident laser radiation, and consequently as a heat diffuser. As the temperature was increased on the sample at 140 GPa, the intensities of Raman peaks characteristic of triple-bonded nitrogen at about 2400 cm^{-1} decreased and the sample darkened further, until 1980 K where areas of the sample became transparent and the Raman modes disappeared. At higher temperatures (>2500 K) the transparent area spread, the pressure was reduced to 115 GPa, and a new vibrational Raman mode appeared at 840 cm^{-1} along with a weak doublet centered at 963 cm^{-1}. These new Raman bands were in very good agreement with the theoretically calculated spectrum associated with the cg-N structure [28, 41] and are shown in Figure 2.3.

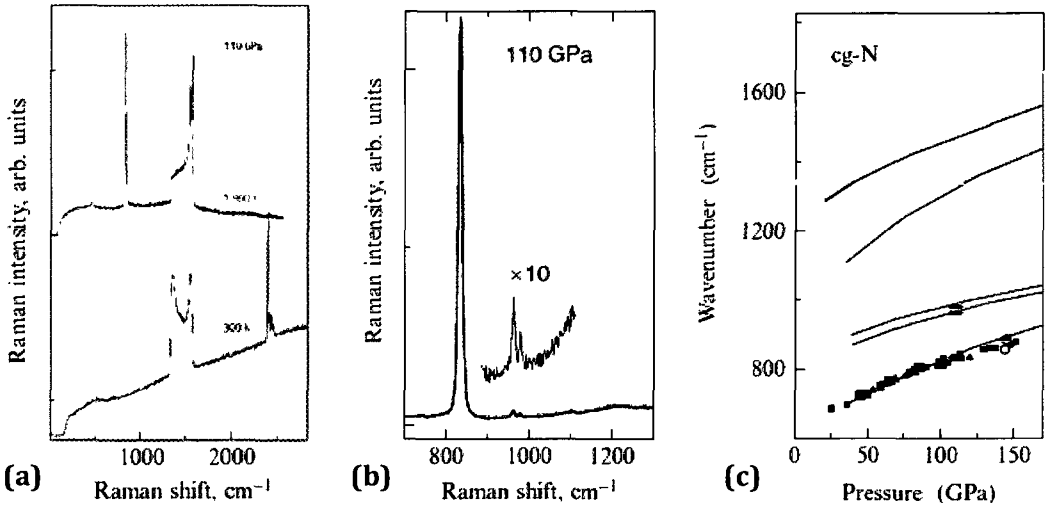

Figure 2.3: Raman spectroscopy results showing (a) the distinct change that occurs upon heating (the band between 1300 - 1550 cm^{-1} is the Raman signal due to diamond), (b) a magnified view of the new Raman bands, and (c) the comparison between experimental (dots) and theoretical (lines) mode frequencies (the shaded region indicates the width of the diamond Raman band). Figure (a) reprinted from ref [39], figures (b) and (c) reprinted from ref. [42].

While the Raman spectroscopic results were indicative of the cubic gauche structure, it needed to be confirmed using x-ray diffraction (XRD). The powder XRD experiments [39] showed that, at pressures above 110 GPa and temperatures above 2000 K, nitrogen undergoes a transition to a transparent phase that indeed results from a high-symmetry structure perfectly consistent with the predicted cubic gauche (cg-N) structure. This structure was further confirmed using single-crystal x-ray diffraction [43], a method better suited for the determination of atomic configuration. The cg-N structure, shown in Figure 2.4, is comprised of a network of three-coordinate nitrogen atoms bound by single covalent bonds of equal lengths.

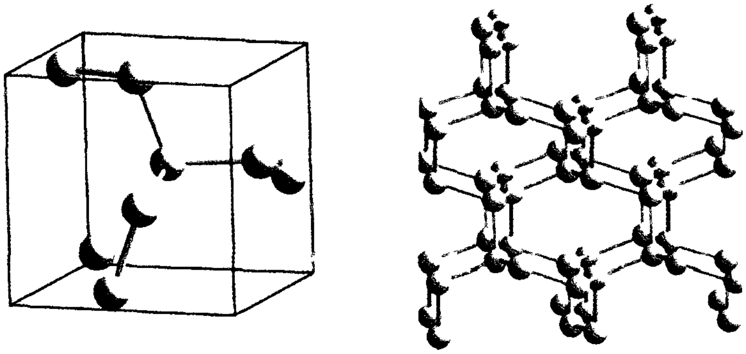

Figure 2.4: The cubic gauche structure of nitrogen (cg-N) showing the unit cell (left) and the extended single-bonded three-dimension network (right). Figure reprinted from ref. [39].

2.2.3 Recovery to ambient conditions

In order to be a functional energetic material, the single-bonded polymeric phase of nitrogen needs to be metastable at ambient conditions and must be able to be easily recovered at these conditions from the extreme synthesis conditions. When transitions occur that drastically change the lattice and volume, they are usually associated with a large hysteresis and are metastable [20]. The archetypical example is the graphite-diamond transition ($\Delta V \approx 26\%$ [44]) where the large zero-pressure kinetic barrier ($\Delta E \approx 0.33$ eV/atom) allows diamond to be recovered at ambient conditions [45]. Calculations on cg-N performed by Mailhiot *et al.* [23] show that the corresponding kinetic barrier for the transformation of cg-N to molecular nitrogen ($\Delta V \approx 22\%$ [42]) at zero-pressure is approximately 0.9 eV, which suggest that cg-N may be metastable at ambient pressure conditions.

Experimental recovery of cg-N has proven extremely difficult as, upon decreasing pressure, the diamond anvil cell gasket that holds the sample frequently weakens and ruptures due to plastic deformation [46]. To date, cg-N has only been retained to 42 GPa, below which it transforms back to the molecular form under weak laser illumination [39]. It is interesting to note that the amorphous nonmolecular phase was successfully recovered at ambient pressures, but only at low temperatures (below 100 K) [37], and thus recovery of the cg-N structure may be possible using a similar thermodynamic path.

Recovery of a single-bonded nitrogen phase to ambient conditions remains a highly sought-after feat. Recently, focus has shifted from retaining pure cg-N to other synthesis and recovery methods such as searching for additional polymeric phases of nitrogen which could be metastable (see refs. [47 - 53] for most recent examples), using dopants to act as polymer stabilizers [19, 39, 54], and synthesizing single-bonded nitrogen starting from high nitrogen content compounds, a topic covered in greater detail in the following section.

2.3 High Pressure High Nitrogen Content Materials as Sources of Single-Bonded Nitrogen

By subjecting materials with high nitrogen contents to high external pressure, it is proposed that as the material is compressed, intramolecular interactions between the nitrogen atoms making up these compounds will become competitive and the formation of an extended single-bonded network of nitrogen will be energetically favourable. One class of compounds well suited to these experiments are based on the N_3^- (azide) anion. This anion is a linear chain formed from three nitrogen atoms linked together by what are essentially double bonds [55]. These bonds are much weaker than those in molecular N_2 and thus N_3^- may form single bonded nitrogen extended networks more easily. To date, the only high pressure experiments of azides reported are of two alkali metal azide ionic salts, sodium and lithium azide (NaN_3 and LiN_3, respectively), and are discussed in the following subsections.

An additional pathway of recovering single-bonded nitrogen is to stabilize the cg-N phase of nitrogen using dopants. Quantum mechanical calculations have shown that the recovery of cg-N upon decompression is hindered by an "unravelling" of the polymeric structure [32] and that a dopant molecule such as hydrogen or ammonia can passivate any reactive terminal ends responsible for this unravelling [56]. The role of hydrogen in stabilization of the single-bonded nitrogen phase has been thoroughly investigated and is briefly summarized in Section 2.3.3.

2.3.1 Sodium azide

The ambient crystal structure of NaN_3, known as the β phase, has a rhombohedral unit cell and is composed of N_3^- layers separated by layers of Na^+ ions. The N_3^- groups are parallel to each other and perpendicular to the Na^+ layers [55, 57]. At very low pressures ($P < 1$ GPa), NaN_3 transforms to a monoclinic structure (α phase) where the N_3^- molecules are tilted [58 - 60]. As greater pressures are applied, the N_3^- molecules are brought closer together and it is expected that with sufficient pressure, these molecules will interact strongly enough to produce a polymeric network of single-bonded nitrogen. By monitoring the characteristic vibrational modes of the molecular form of N_3^-, the formation of a nonmolecular network can be easily identified by the disappearance of these modes.

The high pressure experiments on sodium azide were reported by Eremets *et al.* in 2004 [61]. They found that at about 50 GPa the sample darkened and three new vibrational modes appeared. This new phase was labelled phase II (phase I being a new uncharacterized molecular phase which occurs between 19 and 50 GPa). With increasing pressure, the sample continued to darken and was completely black above 120 GPa. By 120 GPa, the characteristic N_3^- mode had nearly disappeared and by 160 GPa was completely absent, leaving the vibrational spectrum with only two very broad bands. These results lead to the interpretation of the formation of a nonmolecular, amorphous state, which bears a striking resemblance to the black, amorphous state of pure nitrogen. Since the crystalline form of cg-N was only achieved upon heating amorphous nitrogen, the amorphous state of NaN_3 was also heated.

By heating the NaN_3 sample to temperatures above 3000 K, the broad bands dramatically changed into sharp, pronounced peaks [61], characteristic of an amorphous to crystalline transition. None of the newly observed modes could be attributed to the azide ion, which suggests that this nonmolecular high pressure, high temperature form (phase II) likely features a polymeric nitrogen network. Furthermore, the observed modes were similar to, and showed nearly identical pressure evolutions as, those associated with the cg-N phase of pure nitrogen [62]. However, since x-ray diffraction measurements have not been performed, this conclusion is not yet definitive. The observed nonmolecular phase II has a very large hysteresis; upon decompression, it is retained to very low pressures (< 1 GPa) but, upon the full release of pressure, does transform back to the ambient β-NaN_3 molecular phase. If phase II sodium azide is indeed characterized by cubic gauche single-bonded nitrogen, it would represent a much lower starting transition pressure (50 GPa, as opposed to 110 GPa for pure nitrogen); but, like cg-N, could not be recovered at ambient conditions.

2.3.2 Lithium azide

With the success of sodium azide, the natural progression of research was to expand the study to include other alkali azides. In 2009, Medvedev *et al.* [63] reported the ambient temperature study of lithium azide (LiN_3) up to pressures of 62 GPa. At ambient pressure and temperature conditions, LiN_3 has monoclinic crystal lattice and is isostructural to the α phase of NaN_3 [64]. However, in contrast to the rich polymorphism of NaN_3 below 50 GPa, the monoclinic phase of LiN_3 remained stable up to at least 62 GPa. Of course, this by no means indicates that polymeric nitrogen cannot be formed from LiN_3; experiments at higher pressures and/or high temperatures are required.

2.3.3 N_2-H_2 mixtures

While not technically high nitrogen content materials, mixtures of pure nitrogen and hydrogen have produced interesting and promising results. Mixtures of pure N_2 and H_2 in a ratio of 2:1 were studied up to 83 GPa at room temperature using vibrational spectroscopy by Ciezak *et al.* [19, 65, 66]. The mixture solidified at approximately 6 GPa as translucent single crystals (see Figure 2.5a). At about 30 GPa phase separation into two distinct phases was seen (see Figure 2.5b); phase A (pale yellow) and phase B (transparent), separated by a dark red interface. Upon further increase of pressure, phase A darkened to a deep red colour, phase B remained transparent, and the interface became much less pronounced (see Figure 2.5c).

Figure 2.5: Photomicrographs of N_2/H_2 mixtures taken at (a) 6.3 GPa showing the homogeneous alloy, (b) 30 GPa showing phase separation into two phases labelled A and B, and (c) 75 GPa showing the effect of pressure on the colour of phase B. Figure from ref. [19].

Vibrational spectroscopy experiments indicated that phase A is relatively amorphous, and it was proposed that the red colour that develops arises from a partial conversion of molecular N≡N nitrogen to clusters of conjugated N-N=N-N bonds, a form thought to be a possible precursor of cg-N [67].

Phase B was found to be rich in both nitrogen and hydrogen as evidenced by the observation of their characteristic vibrational modes. With increasing pressure, new vibrational modes appeared with increasing intensities, a feature consistent with an increasing concentration of single-bonded nonmolecular nitrogen. Also with increasing pressure, the modes associated with molecular N_2 and H_2, and N-H bonds decreased in intensity. However, since they are still present even at the highest pressure (83 GPa), the transformation to a pure single-bonded network was incomplete.

Decompression studies were reported as inconclusive, but it was shown that a small quantity of the high pressure nonmolecular phase was retained to 7 GPa.

2.4 Motivation and Scope of This Work

2.4.1 Cyanuric triazide

To build upon the previous studies using alkali metal azides as sources of single-bonded nitrogen at high pressures, the first compound to be studied in this work is cyanuric triazide or CTA for short. First-principles density functional theory calculations were performed by Hu and Zhang [68] and showed that CTA could act as a precursor to the formation of a C_3N_{12} solid that is characterized by an extended network of strong covalent N-N and C-N single bonds, not unlike polymeric cg-N.

As previously mentioned in Section 2.1.2, many new high nitrogen content energetic materials are based on five-membered CN_4 rings known as tetrazoles. In the case of cyanuric triazide, if the azide chains form a closed-ring structure, the tritetrazole isomer of CTA is produced, as shown in Figure 2.6. Due to the aromaticity of the triazine ring in the CTA structure, it is calculated to be more favourable than the tritetrazole structure by 0.072 eV/atom in the gas phase [69] and 0.022 eV/atom in the condensed phase [68] at ambient conditions.

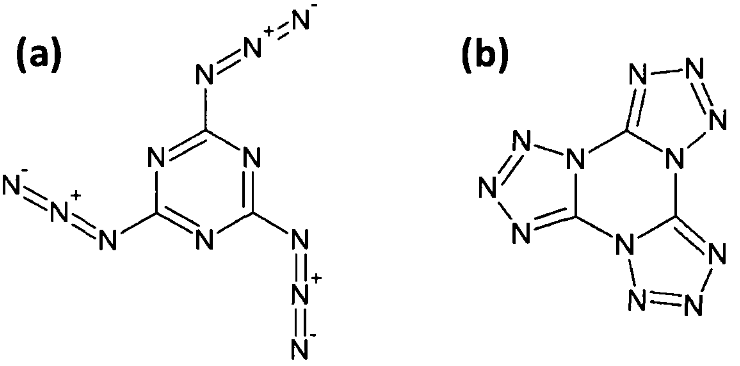

Figure 2.6: Structural isomers of C_3N_{12}: (a) cyanuric triazide and (b) tritetrazole.

With increased pressure, the calculations showed [68] that the enthalpy of the tritetrazole structure drops below that of cyanuric triazide above 8 GPa, and that the enthalpy of the C_3N_{12} solid drops below that of CTA and tritetrazole at 27 and 30 GPa, respectively, as seen in Figure 2.7.

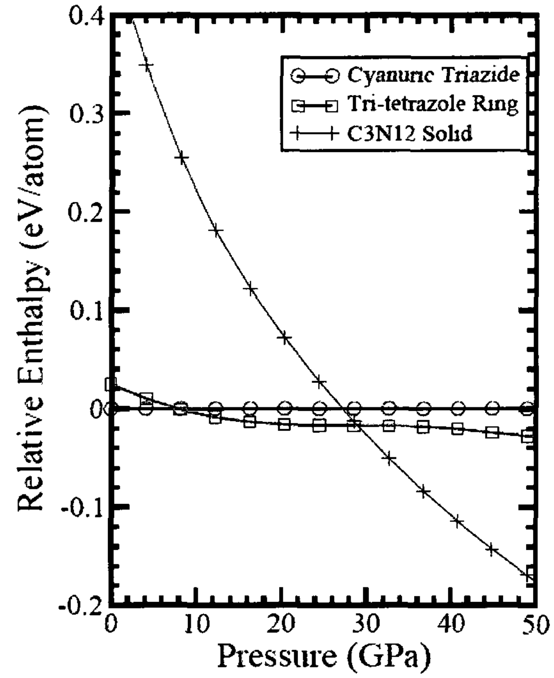

Figure 2.7: The calculated relative enthalpy with respect to cyanuric triazide as a function of pressure. The open circles (black), the open squared (red), and the plus symbols (green) represent the cyanuric triazide, tritetrazole, and C_3N_{12} solid isomers, respectively. Results and figure were provided by Hu and Zhang [68].

Upon further compression, the calculations [68] identified a direct transformation from the tritetrazole to the C_3N_{12} solid at approximately 100 GPa, as seen in Figure 2.8. However, no such direct transformation was observed between cyanuric triazide and the C_3N_{12} solid, at least up to 160 GPa.

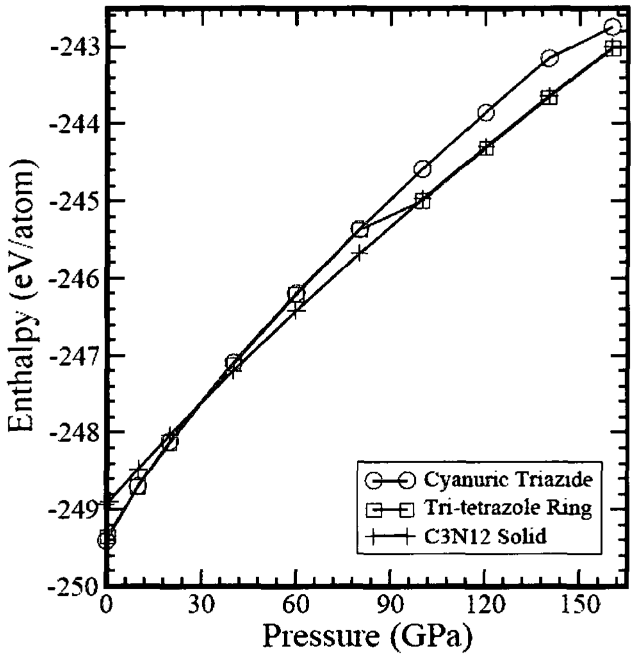

Figure 2.8: The calculated enthalpy phase diagram for cyanuric triazide (black open circles), tritetrazole (red open squares), and C_3N_{12} solid (blue plus symbols). A transition between tritetrazole and C_3N_{12} is directly observed at approximately 100 GPa. Results and figure were provided by Hu and Zhang [68].

In comparing the transformation to the C_3N_{12} solid starting from CTA and tritetrazole, it is clear that the orbital bonding of the carbon atoms and electron cyclization plays a crucial role in the formation of the carbon nitride network. The non-aromatic single-bonded triazine ring in the tritetrazole structure is more active under pressure and results in sp^2 to sp^3 orbital transformation of the carbon atoms (three-coordinate to four-coordinate).

It was also computationally found [68] that this sp^2 to sp^3 transformation can occur directly from cyanuric triazide at 80 GPa and 2000 K, and thus by combining high temperatures with high pressures, the tritetrazole isomer precursor for transformation into the C_3N_{12} solid form becomes unnecessary.

Regardless of which isomer of C_3N_{12} acts as the originator, the formation of a C_3N_{12} solid would be of distinct experimental interest. It is calculated [68] to have a monoclinic unit cell (space group *P*2) where the nitrogen atoms form a single-bonded network with sp^3 carbon atoms at the boundaries, as seen in Figure 2.9. By replacing the substantially weaker intermolecular interactions in CTA with a strong intramolecular covalent network, the C_3N_{12} solid exhibits a large activation barrier towards the reverse transformation. And indeed, molecular dynamics simulations [68] have shown this C_3N_{12} solid structure to be metastable at ambient conditions. Furthermore, at these same ambient conditions, the C_3N_{12} solid is calculated to have an energy density of more than 3 times that of TNT.

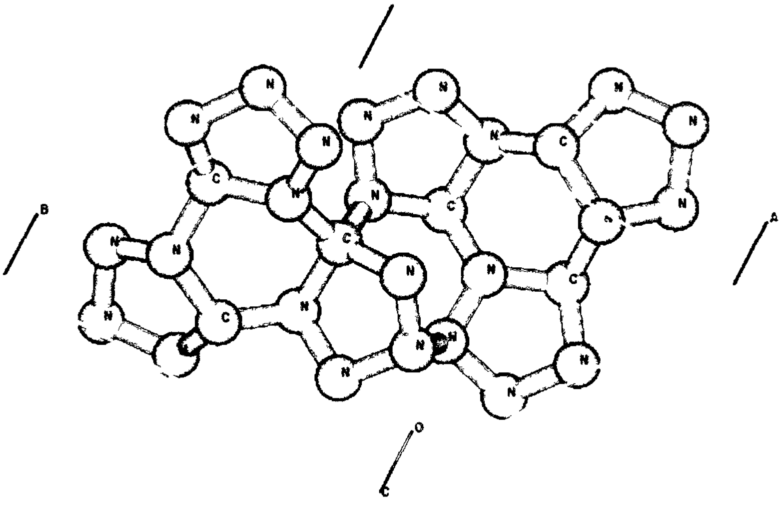

Figure 2.9: Theoretically predicted monoclinic crystal structure of the C_3N_{12} solid. Figure provided by Hu and Zhang [68].

Cyanuric triazide has shown to be a possible precursor to the formation of a nitrogen-rich carbon nitride solid which is characterized by a covalent single-bonded network and has been further calculated to be metastable at ambient conditions. Thus, cyanuric triazide presents a theoretically predicted pathway to recovering a material containing a single-bonded nitrogen network at ambient conditions. To explore this pathway, this work will present a high pressure study of cyanuric triazide.

2.4.2 Ammonium azide

To complement both the work done on other azide salts as well as the N_2 - H_2 mixtures at high pressures, the second compound to be studied in this work is the non-metallic salt ammonium azide ($NH_4^+N_3^-$) or AA for short. First-principles density functional theory calculations were performed by Hu and Zhang [70] and showed that AA could act as a precursor to the formation of a hydronitrogen solid with a composition of $(NH)_4$ that is characterized by single-bonded zigzag nitrogen chains.

In order to find the lowest enthalpy structures of hydronitrogen systems, *ab initio* evolutionary searches were performed by Hu and Zhang [70]. In the range of 30 - 100 GPa, these searches uncovered three stable structures with N_4H_4 stoichiometries, namely, the known ambient pressure structures of ammonium azide (AA) and its covalently bonded isomer, trans-2-tetrazene (TTZ), along with a $(NH)_4$ hydronitrogen solid.

The $(NH)_4$ hydronitrogen solid is composed of one-dimensional, single-bonded, hydrogen-caped nitrogen zigzag chains arranged in a monoclinic unit cell (space group $P2_1/m$), as seen in Figure 2.10. The stability of this solid arises from the separation of the electron lone pairs of neighbouring nitrogen atoms.

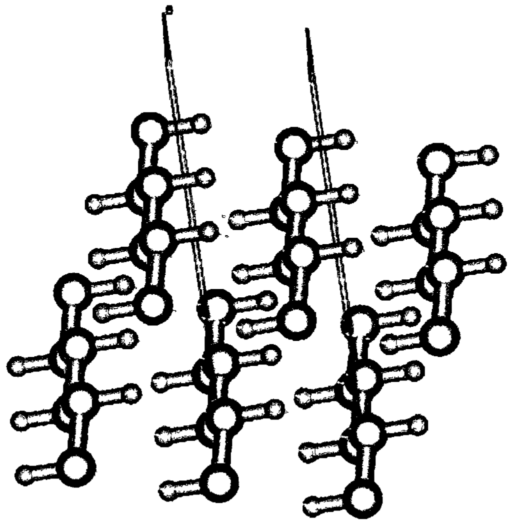

Figure 2.10: Calculated crystal structure of the monoclinic $(NH)_4$ hydronitrogen structure. Figure provided by Hu and Zhang [70].

At high pressures, this stability results in a calculated enthalpy [70] much lower than that of the molecular forms (AA and TTZ), as shown in Figure 2.11, for example. And indeed, based on calculated phase diagrams [70], the predicted equilibrium (zero temperature) transformation pressure for the hydronitrogen solid is about 36 GPa from ammonium azide and 75 GPa from trans-2-tetrazene.

Further simulations were performed [70] to investigate the transformations from AA and TTZ to the hydronitrogen solid at ambient temperature (298 K). The results show that a hydronitrogen chain can be formed by compressing TTZ up to 220 GPa. This pressure is far above the predicted equilibrium pressure (75 GPa) due to a large thermal barrier. Simulations starting from the AA structure showed formation of hydronitrogen fragments, but were always mixed with ammonia (NH_3) or hydrazoic acid (N_3H) molecules, which prevented further transformations to the $(NH)_4$ zigzag chains. The calculated energy barriers following the transformation path of ammonium azide to the hydronitrogen solid are shown in Figure 2.12.

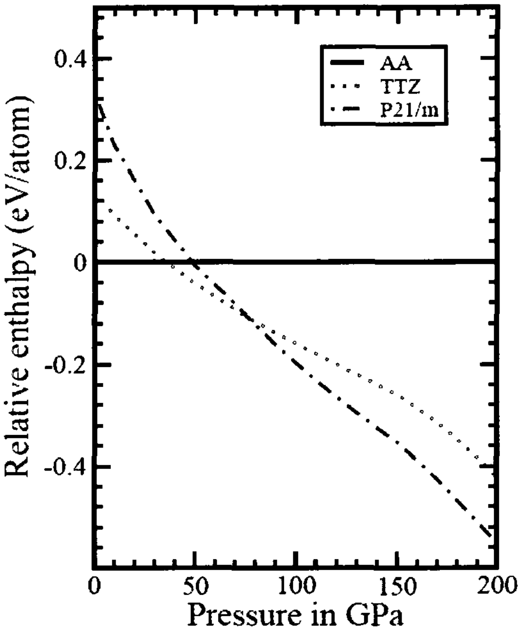

Figure 2.11: The calculated relative enthalpy with respect to ammonium azide as a function of pressure. The black solid, red dotted, and blue dot-dashed lines represent ammonium azide, trans-2-tetrazene, and hydronitrogen solid, respectively. Results and figure were provided by Hu and Zhang [70].

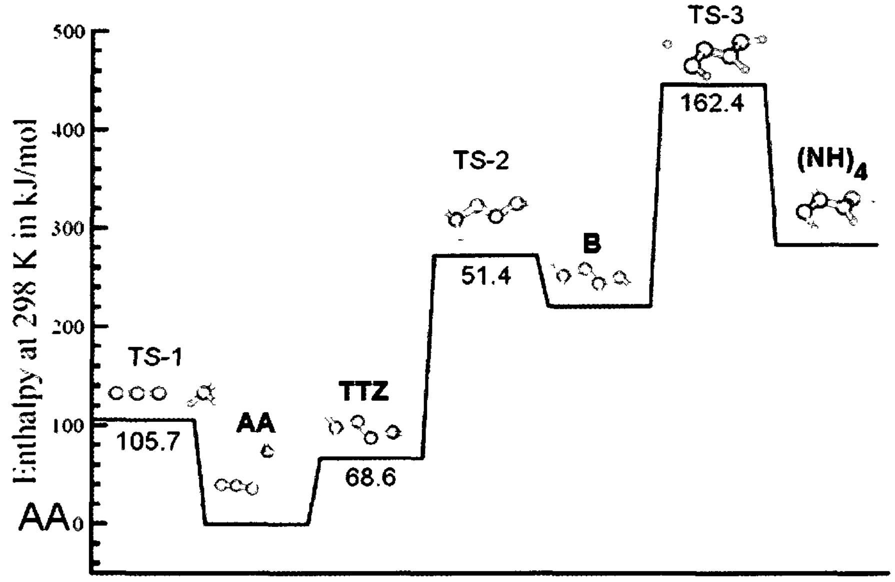

Figure 2.12: Calculated enthalpies of AA, TTZ, $(NH)_4$, molecular phase B, and transition states TS-1, TS-2, and TS-3 at room temperature and pressure. Results and figure were provided by Hu and Zhang [70].

Due to the large thermal barrier of the hydrogen migration (between the B and $(NH)_4$ states as seen in Figure 2.12), the hydronitrogen solid should be quite stable at ambient conditions. Indeed, molecular dynamics calculations [70] have shown this hydronitrogen solid structure to be metastable at room temperature and pressure.

In brief summary, ammonium azide has shown to be a possible precursor to the formation of a hydronitrogen solid that is characterized by single-bonded nitrogen zigzag chains, which has further been calculated to be metastable at ambient conditions. Thus, ammonium azide also presents a theoretically predicted pathway to recovering single-bonded nitrogen at ambient conditions. To explore this pathway, this work will present a high pressure study of ammonium azide.

2.5 Studying Materials at High External Pressures

Subjecting materials to high external pressures using diamond anvil cell techniques has recently been of very keen interest to scientists in almost every discipline; in the past few months alone, the materials studied range from pure elements [71] to bacteria [72]. No matter what the motivation, the application of pressure is used as a valuable tool to study the properties of the material, and in most cases, to change these properties. In this work, pressure is used in an attempt to induce transitions, and acts to probe the existence of novel phases of the material of interest. The transitions can be as simple as slight distortions to a crystal structure or as drastic as turning an insulator into a semiconductor or even a metal.

The following sections outline the presence and stabilities of phases of a material based on their thermodynamic properties, and how the evolution of these phases with applied pressure can be used to extract certain characteristics of the material.

2.5.1 Phase stability and phase transitions

The specific form taken by a material is called the phase, which can be described in terms of thermodynamic state variables. There are two types of these variables, intensive (generalized forces such as pressure *P* and temperature *T*) and extensive (generalized displacements such as volume *V* and entropy *S*). These quantities are commonly found as pairs in which the product has the dimension of energy (for example, PV and TS). The energy of the system can be expressed as various different potentials, each with different state quantities as independent variables. To be useful, a formulation is needed where the only independent variables are those which can be controlled and measured. Thus, for high pressure studies, the system energy is best described in terms of the Gibbs free energy, *G*, a potential that is a function of pressure and temperature. The exact differential is given as:

$$dG = -SdT + VdP \tag{2.1}$$

allowing the extensive variables *S* and *V* to be defined as partial differentials:

$$S = -\left(\frac{\partial G}{\partial T}\right)_P \tag{2.2}$$

$$V = \left(\frac{\partial G}{\partial P}\right)_T \tag{2.3}$$

The Gibbs free energy of every possible configuration of a material has a unique dependence on pressure and temperature. Like almost every other known system, it is driven by energy minimization. Therefore, at a given set of *P*,*T* conditions, the configuration with the minimal value of *G* will be the observed phase. As either (or both) of these intensive quantities is varied, it may be that a different configuration becomes more energetically favourable, and a phase transition is observed. This is illustrated below in Figure 2.13 for the case of isothermal compression, as is performed in this work.

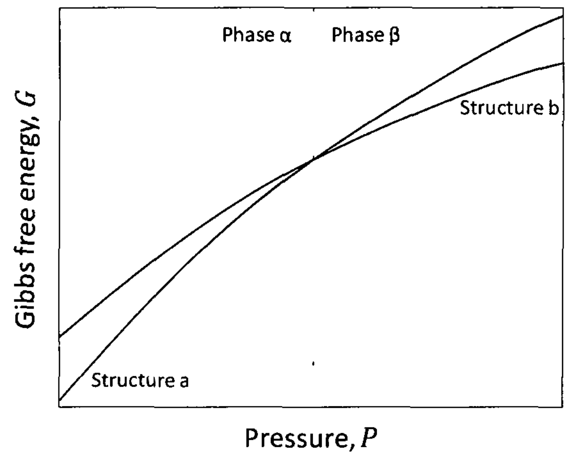

Figure 2.13: Evolution of the Gibbs free energy during isothermal compression for two configurations, structure a in red and structure b in blue. At low pressures structure a is most stable resulting in the observed phase α, but undergoes a pressure-induced phase transition at the intersection of curves (marked by the dashed line) to phase β, characterized by structure b.

Across a pressure-induced phase transition, there is no change in either temperature or pressure, and therefore no change in the Gibbs free energy (that is, d*G* = 0). However, its isothermal change in first derivative with respect to pressure (i.e., volume) is non-zero. This is represented by Figure 2.14 and Equation 2.4 [73].

$$\left(\frac{\partial G_\beta}{\partial P}\right)_T - \left(\frac{\partial G_\alpha}{\partial P}\right)_T = V_\beta - V_\alpha = \Delta_{trs} V \qquad (2.4)$$

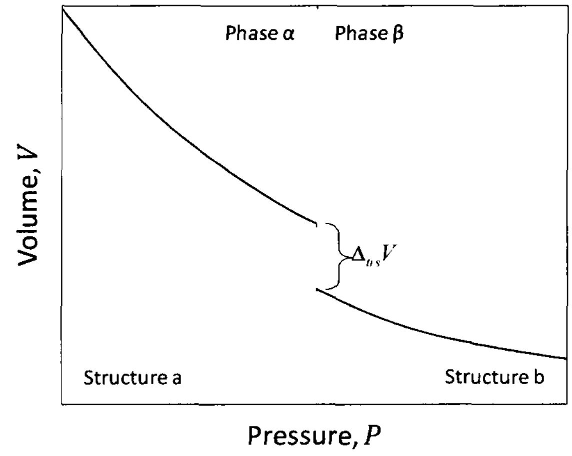

Figure 2.14: Evolution of the first derivative of the Gibbs free energy with respect to pressure (volume) during isothermal compression showing a finite discontinuity (volume collapse) *across the phase transition*

Since this is a discontinuity in the first derivative of the thermodynamic potential, this type of transition is classified as a first order phase transition [74]. In the solid state, pressure-induced first order phase transitions are typically accompanied by a rearrangement of the constituent atoms, and sometimes, a change in the bonding between these atoms. By studying the structure of a material as a function of pressure (and/or temperature), phase transitions can be easily identified and may lead to the discovery of novel dense phases, unexpected bonding patterns, changes in optical, electronic, mechanical properties, etc. As one of many examples, at very high pressures (>96 GPa) oxygen transforms to a metallic state [75].

2.5.2 Isothermal equations of state

Along with the generation of the phase diagram, the properties of the observed phases can be determined by modeling their unique relationships between volume and pressure. There are two parameters which characterize these relations and describe the properties of the material.

The first is the isothermal bulk modulus, B_0, a quantity which describes the stiffness of a material where the larger the value, the more incompressible the material is. It is expressed as:

$$B_0 = -V\left(\frac{\partial P}{\partial V}\right)_{P=0} \tag{2.5}$$

where $P = 0$ and the subscript 0 signify ambient pressure. The second parameter describes how the stiffness changes with pressure, and is given by the first derivative of the bulk modulus with respect to pressure:

$$B_0' = \left(\frac{\partial B_0}{\partial P}\right)_{P=0} \tag{2.6}$$

The larger the value of B_0' the more rapidly the material stiffens with applied pressure.

For high pressure studies, the experimental P,V curves (similar to Figure 2.14) must be modeled using an appropriate parameterization of B_0 and B_0', known as an equation of state (EOS). The resulting equation will give the volume as a function of pressure for a particular phase in terms of B_0 and B_0', which are fit to the observed data. The simplest equation of state one can imagine is generated by assuming the bulk modulus is constant, that is $B_0' = 0$. In this case the volume is related directly to the pressure through the definition of the bulk modulus (Equation 2.5). Integration leads to an EOS given by

$$V = V_0 \exp\left(\frac{-P}{B_0}\right) \tag{2.7}$$

where V_0 is the volume at ambient pressure [76]. While this EOS correctly models the volume evolution at very small pressures, it very quickly and significantly deviates from the observed relationships. With increased external pressures and decreased volumes, the repulsions between atoms increase accordingly, resulting in an increasing bulk modulus over the range of applied pressures [77]. Thus, to take into consideration the pressure dependence of B_0, Murnaghan proposed a local effective bulk modulus for the case of infinitesimal strains [78], given by:

$$B_0 = \frac{1}{3}(3\lambda + 2\mu + P_0) \tag{2.8}$$

where λ and μ are pressure-dependent elastic constants. If they are assumed to be linear functions of the initial pressure, P_0, then the Murnaghan integrated linear equation of state can be generated:

$$P(V) = \frac{B_0}{B_0'}\left[\left(\frac{V_0}{V}\right)^{B_0'} - 1\right] \tag{2.9}$$

Further improvements to the equation of state can be made by incorporating finite strain assumptions (as opposed to infinitesimal strain for the above EOS), where the volume of the compressed state relative to the initial volume is related to the compression, f.

$$f = \frac{1}{2}\left[\left(\frac{V_0}{V}\right)^{2/3} - 1\right] \tag{2.10}$$

The compression is also related to the Helmholtz free energy, F, as

$$9B_0V_0 = \lim_{P\to 0}\left(\frac{1}{f}\frac{\partial F}{\partial f}\right)_t \tag{2.11}$$

which is, in turn, related to the previously defined Gibbs free energy, G, and the pressure, P, by:

$$G = F - TS \tag{2.12}$$

$$P = -\left(\frac{\partial F}{\partial V}\right)_t \tag{2.13}$$

In order to generate an equation of state from this finite strain theory, the Helmholtz free energy is expanded in terms of the compression, f

$$F = a(T)f^2 + b(T)f^3 + c(T)f^4 + \ldots \tag{2.14}$$

If *F* is truncated to second order in *f*, then the above formulation results in the second-order Birch-Murnaghan equation of state [79, 80], given by:

$$P(V)=\frac{3}{2}B_0\left[\left(\frac{V_0}{V}\right)^{7/3}-\left(\frac{V_0}{V}\right)^{5/3}\right] \tag{2.15}$$

By further expanding the Helmholtz free energy to the third order in *f*, the third-order Birch-Murnaghan equation of state [81] is generated and is given by:

$$P(V)=\frac{3}{2}B_0\left[\left(\frac{V_0}{V}\right)^{7/3}-\left(\frac{V_0}{V}\right)^{5/3}\right]\left[1+\frac{3}{4}(B_0'-4)\left(\left(\frac{V_0}{V}\right)^{2/3}-1\right)\right] \tag{2.16}$$

Detailed developments of the above equations of state can be found in several references, such as in [76, 82].

While certainly not the only EOS, the isothermal third-order Birch-Murnaghan EOS (Equation 2.16) is the most commonly used in the field of high pressure research, and the one used in this work. It is parameterized by three variables: V_0, B_0 and B_0', which are determined by fitting the experimental P,V data using a χ^2-minimization routine. It is important to note that if there are a limited number of data points, it may not be possible to fit all three parameters. In that case, B_0' is kept fixed and typically given a value of 4, which is equivalent to using a second-order Birch-Murnaghan EOS (even when it is possible to extract the proper value, most solids have a B_0' value very close to 4).

References

[1] F.P.A. Fabbiani and C.R. Pulham, *Chem. Soc. Rev.* **35**, 932 (2006).

[2] J.C. Oxley, A Survey of the Thermal Stability of Energetic Materials. In P.A. Politzer and J.S. Murray (Eds.) *Energetic Materials, Part 1. Decomposition, Crystal and Molecular Properties* (Elsevier B.V., Amsterdam, The Netherlands, 2003).

[3] P.Y. Robidoux, P. Gong, M. Sarrazin, G. Bardai, I. Paquet, J. Hawari, C. Dubois, and G.I. Sunahara, *Ecotoxicol. Enviro. Safety* **58**, 300 (2004).

[4] P.Y. Robidoux, G.I. Sunahara, K. Savard, Y. Berthelot, S. Dodard, M. Martel, P. Gong, and J. Hawari, *Enviro. Toxicol. Chem.* **23**, 1026 (2004).

[5] J.A. Steevens, B.M. Duke, G.R. Lotufo, and T.S. Bridges, *Enviro. Toxicol. Chem.* **21**, 1475 (2002).

[6] D. Fournier, A. Halasz, J. Spain, R.J. Spanggord, J.C. Bottaro, and J. Hawari, *Appl. Enviro. Microbio.* **70**, 1123 (2004).

[7] N. Fischer, K. Karaghiosoff, T.M. Klapötke, and J. Stierstorfer, *Zeit. Anorgan. Allge. Chem.* **636**, 735 (2010).

[8] P.K. Swain, H. Singh, and S.P. Tewari, *J. Mol. Liq.* **151**, 87 (2010).

[9] T. Abe, G.H. Tao, Y.H. Joo, R.W. Winter, G.L. Gard, and J.M. Shreeve, *Chem. Euro. J.* **15**, 9897 (2009).

[10] T.M. Klapötke and C.M. Sabaté, *New J. Chem.* **33**, 1605 (2009).

[11] T.M. Klapötke, C.M. Sabaté, and M. Rasp, *J. Mater. Chem.* **19**, 2240 (2009).

[12] T.M. Klapötke, C.M. Sabaté, and J. Stierstorfer, *New J. Chem.* **33**, 136 (2009).

[13] T.M. Klapötke, New Nitrogen-Rich High Explosives. In T.M. Klapötke (Ed.) *High Energy Density Materials* (Springer-Verlag, Heidelberg, Germany, 2007).

[14] T.M. Klapötke (Ed.) *High Energy Density Materials* (Springer-Verlag, Heidelberg, Germany, 2007).

[15] L.E. Fried, M. Riadd Manaa, P.F. Pagoria, and R.L. Simpson, *Ann. Rev. Mater. Res.* **31**, 291 (2001).

[16] D.M. Budgujar, M.B. Talawar, S.N. Asthana, and P.P. Mahulikar, *J. Haz. Mater.* **151**, 289 (2008).

[17] F. Zhang, S. Alvari, A. Hu, T.K. Woo, First Principles Molecular Simulation of Energetic Materials at High Pressures. In H. Yasuyuki (Ed.) *Library of Shock Wave Science and Technology Reference Library, Volume 3: Solids II* (Springer-Verlag, Heidelberg, Germany, 2009).

[18] D.I.A. Miller, W.G. Marshall, I.D.H. Oswald, and C.R. Pulham, *Crys. Rev.* **16**, 115 (2010).

[19] J.A. Ciezak, Army Research Laboratory Technical Report No. **ARL-TR-4478** (2008).

[20] M.I. Eremets, I.A. Trojan, A.G. Gavriliuk, and S.A. Medvedev, Synthesis of High-Nitrogen Energetic Material. In S.M. Peiris and G.J. Piermarini (Eds.) *Static Compression of Energetic Materials* (Springer-Verlag, Heidelberg, Germany, 2008).

[21] A.K. McMahan and R. LeSar, *Phys. Rev. Lett.* **54**, 1929 (1985).

[22] R.M. Martin and R.J. Needs, *Phys. Rev. B* **34**, 5082 (1986).

[23] C. Mailhiot, L.H. Yang, and A.K. McMahan, *Phys. Rev. B* **46**, 14419 (1992).

[24] H. Iwasaki and T. Kikegawa, In C. Homan, R.K. MacCrone, and E. Whalley (Eds.) *High Pressure in Science and Technology*, Vol. III (North-Holland, New York, 1984).

[25] B. Morosin and J.E. Schriber, *Solid State Comm.* **10**, 249 (1972).

[26] D. Schiferl, D.T. Cromer, and J.C. Jamieson, *Acta Crys. B* **37**, 807 (1981).

[27] R.M. Brugger, R.B. Bennion, and T.G. Worlton, *Phys. Rev. Lett.* **24A**, 714 (1967).

[28] T.W. Barbee III, *Phys. Rev. B* **48**, 9327 (1993).

[29] L. Mitas and R.M Martin, *Phys. Rev. Lett.* **72**, 2438 (1994).

[30] E.S. Yakub, *Physica B* **265**, 31 (1998).

[31] M.M.G. Alemany and J.L. Martins, *Phys. Rev. B* **68**, 024110 (2003).

[32] W.D. Mattson, *The Complex Behavior of Nitrogen Under Pressure: Ab Initio Simulation of the Properties of Structures and Shock Waves*, Ph.D. thesis, University of Illinois, Urbana-Champaign (2003).

[33] R. Reichlin, D. Schiferl, S. Martin, C. Vanderborgh, and R.L. Mills, *Phys. Rev. Lett.* **55**, 1464 (1985).

[34] P.M. Bell, H.K. Mao, and R.J. Hemley, *Physica B&C* **139&140B**, 16 (1986).

[35] F.P. Bundy, *J. Geophys. Res.* **85**, 6930 (1980).

[36] A.F. Goncharov, E. Gregoryanz, H.K. Mao, Z. Liu, and R.J. Hemley, *Phys. Rev. Lett.* **85**, 1262 (2000).

[37] M.I. Eremets, R.J. Hemley, H.K. Mao, and E. Gregoryanz, *Nature* **411**, 170 (2001).

[38] K. Nordlund, A. Krasheninnikov, N. Juslin, J. Nord, and K. Albe, *Europhys. Lett.* **65**, 400 (2004).

[39] M.I. Eremets, A.G. Gavriliuk, I.A. Trojan, D.A. Dzivenko, and R. Boehler, *Nature Mat.* **3**, 558 (2004).

[40] E. Gregoryanz, A.F. Goncharov, C. Sanloup, M. Somayazulu, H.K. Mao, and R.J. Hemley, *J. Chem. Phys.* **126**, 184505 (2007).

[41] R. Caracas, *J. Chem. Phys.* **127**, 144510 (2007).

[42] I.A. Trojan, M.I. Eremets, S.A. Medvedev, A.G. Gavriliuk, and V.B. Prakapenka, *Appl. Phys. Lett.* **93**, 091907 (2008).

[43] M.I. Eremets, A.G. Gavriliuk, and I.A. Trojan, *Appl. Phys. Lett.* **90**, 171904 (2007).

[44] M.I. Eremets, T. Takemura, H. Yusa, D. Goldberg, Y. Bando, V.D. Blank, Y. Sato, and K. Watanabe, *Phys. Rev. B* **57**, 5655 (1998).

[45] J. Furthmueller, J. Hafner, and G. Kresse, *Phys. Rev. B* **50**, 15606 (1994).

[46] M.I. Eremets, *High Pressure Experimental Methods* (Oxford University Press, New York, 1996).

[47] X. Wang, F. Tian, L. Wang, T. Cui, B. Liu, and G. Zou, *J. Chem. Phys.* **132**, 024502 (2010).

[48] C.J. Pickards and R.J. Needs, *Phys. Rev. Lett.* **102**, 125702 (2009).

[49] Y. Ma, A.R. Oganov, Z. Li, Y. Xie, and J. Kotakoski, *Phys. Rev. Lett.* **102**, 065501 (2009).

[50] J. Hooper, A. Hu, F. Zhang, and T.K. Woo, *Phys. Rev. B* **80**, 104117 (2009).

[51] J. Kotakoski and K. Albe, *Phys. Rev. B* **77**, 144109 (2008).

[52] Y. Yao, J.S. Tse, and K. Tanaka, *Phys. Rev. B* **77**, 052103 (2008).

[53] R. Caracas and R. J. Hemley, *Chem. Phys. Lett.* **442**, 65 (2007).

[54] W.L. Vos, L.W. Finger, R.J. Hemley, J.Z. Hu, H.K. Mao, and J.A. Schouten, *Nature* **358**, 46 (1992).

[55] P. Botschwina, *J. Chem. Phys.* **85**, 4591 (1986).

[56] W.L. Vos, L.W. Finger, R.J. Hemley, J.Z. Hu, H.K. Mao, and J.A. Schouten, *Nature* **358**, 46 (1992).

[57] C.S. Choi and E. Prince, *J. Chem. Phys.* **64**, 4510 (1976).

[58] Z. Iqbal, *J. Chem. Phys.* **59**, 1769 (1973).

[59] G.J. Simonis and C.E. Hathaway, *Phys. Rev. B* **10**, 4419 (1974).

[60] L.B. Kanney, N.S. Gillis, and J.C. Raich, *J. Chem. Phys.* **67**, 81 (1977).

[61] M.I. Eremets, M.Y. Popov, I.A. Trojan, V.N. Denisov, R. Boehler, and R.J. Hemley, *J. Chem. Phys.* **120**, 10618 (2004).

[62] M. Popov, *Phys. Lett. A* **334**, 317 (2005).

[63] S.A. Medvedev, I.A. Trojan, M.I. Eremets, T. Palasyuk, T.M. Klapötke, and J. Evers, *J. Phys.: Condens. Matter* **21**, 195404 (2009).

[64] G.E. Pringle and D.E. Noakes, *Acta Crys. B* **24**, 262 (1968).

[65] J.A. Ciezak and T.A. Jenkins, Metastable Polymeric Nitrogen From N_2/H_2 Alloys, *Proceedings of the Army Science Conference (26th),* Orlando, Florida (December 2008).

[66] J.A. Ciezak, T.A. Jenkins, and R.J. Hemley, *AIP Conf. Proc.* **1195**, 1291 (2009).

[67] M.J. Lipp, J.P. Klepeis, B.J. Baer, H. Cynn, W.J. Evans, V. Iota, and C.S. Yoo, *Phys. Rev. B* **76**, 014113 (2007).

[68] A. Hu and F. Zhang, *A nitrogen-rich C_3N_{12} solid transformed from cyanuric triazide under high pressure and temperature*, manuscript in preparation (2010).

[69] A. Hammerl, T.M. Klapötke, R. Rocha, *Eur. J. Inorg. Chem.* **2006**, 2210 (2006).

[70] A. Hu and F. Zhang, *A hydronitrogen solid: high pressure ab initio evolutionary structure searches*, manuscript in preparation (2010).

[71] P.M. Celliers, P. Loubeyre, J.H. Eggert, S. Brygoo, R.S. McWilliams, D.G. Hicks, T.R. Boehly, R. Jeanloz, and G.W. Collins, *Phys. Rev. Lett.* **104**, 184503 (2010).

[72] P.M. Oger, I. Daniel, and A. Picard, *Ann. N.Y. Acad. Sci.* **1189**, 113 (2010).

[73] P. Atkins and J. De Paula, *Physical Chemistry*, 8th ed. (Oxford University Press, New York, 2006).

[74] P. Ehrenfest, *Commun. Kamerlingh Onnes Lab., Leiden Suppl.* **75b**, (1933).

[75] S. Desgreniers, Y.K. Vohra, and A.L. Ruoff, *J. Phys. Chem.* **94**, 1117 (1990).

[76] J. Poirier, *Introduction of the Physics of the Earth's Interior*, 2nd ed. (Cambridge University Press, New York, 2000).

[77] R.A. Angel, Some Practical Aspects of Studying Equations of State and Structural Phase Transitions at High Pressure. In A. Katrusiak and P. McMillan (Eds.) *High-Pressure Crystallography (NATO Science Series II. Mathematics, Physics and Chemistry, Volume 140)*, (Kluwer Academic Publishers, Dordrecht, The Netherlands, 2004).

[78] F.D. Murnaghan, *Finite Deformation of an Elastic Solid* (Dover, New York, 1967).

[79] F. Birch, *J. Appl. Phys.* **9**, 279 (1938).

[80] F. Birch, *Phys. Rev*, **71**, 809 (1947).

[81] F. Birch, *J. Geophys. Res.* **57**, 227 (1952).

[82] W.B. Holzapfel, *Z. Kristallogr.* **216**, 473 (2001).

Chapter 3

Experimental Methods

The following sections will outline the experimental techniques used in the current work to study cyanuric triazide and ammonium azide at high pressure. The discussion will include the generation and measurement of high pressures, vibrational Raman spectroscopy, and high-resolution angle-dispersive powder x-ray diffraction.

3.1 Diamond Anvil Cell

3.1.1 Introduction and overview

To generate the high pressures required for these experiments, a diamond anvil cell is used, the core components of which are depicted in Figure 3.1. The design is based on two opposed diamond anvils with a metallic gasket pressed between them. The gasket contains a small hole acting as a compression chamber to hold the sample being studied. The diamonds are typically about ¼ - ⅓ carat, and are specially selected among natural stones for their low levels of dislocation densities and chemical impurities. They have a large flat top surface (table) and a very small bottom surface (culet) such that, by applying even a moderate force to the anvil table and concentrating it to the small area of the culet, extreme pressures can be achieved. While the basics of the original design introduced in 1959 [1, 2] have largely remained the same, many improvements and tweaks introduced throughout the years have pushed the boundaries of the maximum attainable pressure. Pressures of up to a megabar (1 Mbar = 100 GPa) are now regularly achieved, and multi-megabar pressures are becoming increasingly common. All of this from a beautifully simplistic design that fits in the palm of one's hand.

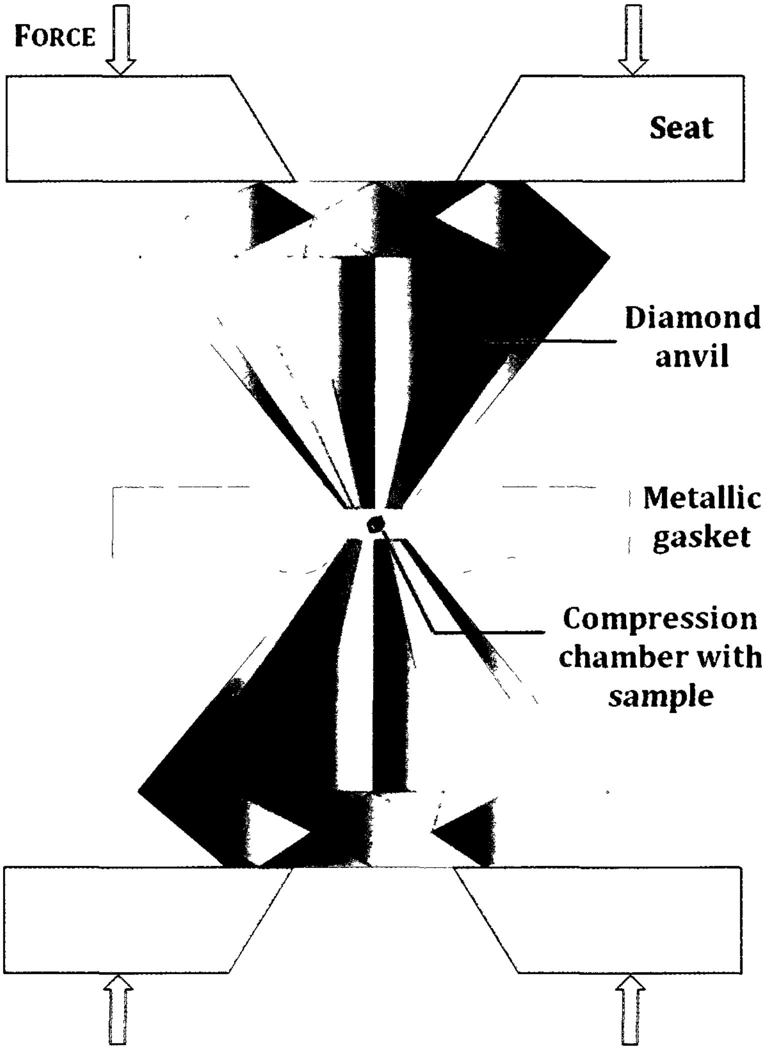

Figure 3.1: Schematic of the core components of the diamond anvil cell: the opposed diamond anvils, the metallic gasket, the compression chamber that houses the sample, and the seats. The direction of applied force is also shown. Figure courtesy of S. Desgreniers.

3.1.2 Anvils

Diamond has many properties which make it the ideal material for high pressure studies. First of all, it is the hardest known natural material, meaning it can withstand repeated exposure to very high forces and stresses without failure. Along with the ability to generate high pressures, pure diamond also allows for a near unobstructed, *in situ* view of the sample. Transparency to a wide range of wavelengths, including light in the UV, visible, and IR spectral ranges, allows for a large variety of spectroscopic probes of the sample through the diamond anvils. Diamond is also well-suited to x-ray measurements as it is transparent to hard x-rays (short wavelengths) above about 20 keV and offers minimal absorption due to its low atomic (Z) number.

The diamonds used in the cell are specially selected for their specific properties, based on the types of measurements to be performed. There are two types of diamond that are commonly used in DACs, type Ia and type IIa. The type IIa diamonds are essentially free of any impurities and thus offer a very low luminescence, a property very useful for optical studies. However, they are exceptionally rare. The much more common type Ia diamonds are characterized by a >0.3% nitrogen impurity with the nitrogen atoms occurring in pairs [3]. The anvils used in the current work were gemstone quality type Ia diamonds that had been specifically selected for their low luminescence and low dislocation density (any defect present, especially at the culet surface, can become a nucleation site for cracks under high pressure conditions).

Once the type of diamond has been selected, they need to be cut and sized appropriately. To create the anvil, the tip of the common brilliant cut stone is ground and polished down to create an octagonal or 16-sided culet (Figure 3.2). The dimensions of the culet depend on the required pressure range; in this work 300 μm diameter culets were used where pressures of 60-70 GPa were easily attainable. It is important to note that many other cuts and shapes of anvils can be, and are, widely used. For example, to reach very high pressures (>100 GPa), bevelled anvils with a two-stage culet (Figure 3.3) are typically used.

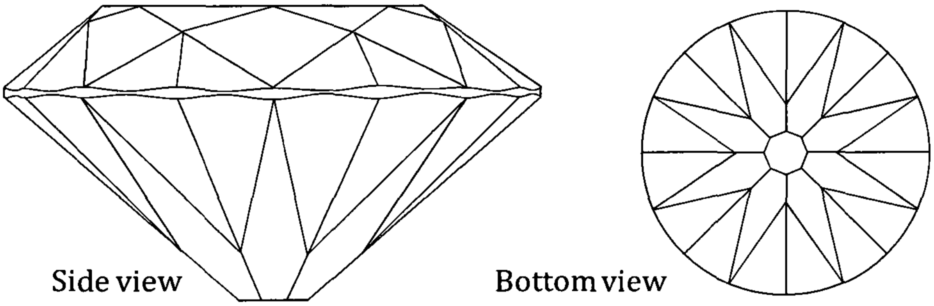

Figure 3.2: Side and bottom views of the brilliant cut gemstone with a ground octagonal culet surface. The size of the culet is determined by the pressure requirements.

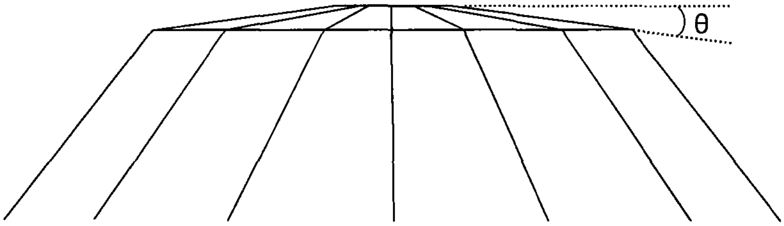

Figure 3.3: Side view of the design of the bevelled anvil culet used to generate pressures greater than 100 GPa. The optimal bevel angle has been determined to be θ ≈ 7-8° [3].

While diamond is ideal for high pressure studies in many ways, it can sometimes be obstructive. For example, when performing Raman spectroscopy experiments (to be discussed in Section 2.3) with the diamond anvil cell, the first and second order Raman bands of the diamond itself can be a real nuisance. Because the Raman spectroscopic data from a 50 μm thick sample is being collected through about 2 mm of diamond for each anvil, the intensity of the diamond Raman modes can be orders of magnitude more intense and can mask any Raman signal in that region arising from the material being studied. If that spectral region contains important information, or in extraordinary circumstances, the only Raman spectroscopic information, it becomes necessary to use a different type of anvil material.

One increasingly popular alternative anvil material is man-made single-crystal moissanite (6H-SiC) [4, 5]. The desirable properties of diamond are mirrored quite well with moissanite; it is very hard (second after diamond), transparent to visible light, and transparent to x-rays above 25 keV. The main advantage over other diamond replacements is its maximum attainable pressure. The use of other anvils such as cubic zirconia and sapphire has resulted in pressures of 16.7 GPa and 25.8 GPa, respectively [6, 7], while the moissanite anvil cell has achieved 58.7 GPa [5]. Being a binary solid, moissanite has several more Raman modes than diamond; however, none of these overlap with the Raman mode of diamond (see Table 3.1). By collecting Raman data using both the DAC and its moissanite-equivalent, the entire spectral range can be covered and all sample peaks would be observed.

Table 3.1: Comparison of the first and second order Raman bands for diamond and moissanite anvils at ambient conditions.

Anvil	**First order Raman modes (cm^{-1})**								**Second order modes (cm^{-1})**
Diamond	1333 (vs)								2300-2700 (w)
Moissanite	142.8 (w)	149.6 (s)	265.5 (w)	504.7 (w)	514.6 (w)	766.9 (s)	788.4 (vs)	964.7 (s)	1398.3-1702.8 (w)

vs = very strong, s = strong, w = weak

3.1.3 Gasket and sample chamber

The primary role of the gasket is to act as a vessel for the sample to be studied; however, the structure itself provides some benefits, such as radial support for the diamond anvils. To be able to withstand high pressures, the gasket material is selected for a high strength, but it must also be ductile and non-brittle. If too brittle, the gasket can develop cracks and rupture, making it impossible to hold pressure in the sample. In this work, fully hardened ANSI T301 stainless steel gaskets were used for low pressure studies ($P < 25$ GPa), while rhenium was used for the majority of experiments as it can easily withstand high pressures without failure.

The first step to preparing a gasket for use is to make an indentation. This initial compression is crucial to further cold work the material so to provide a stable compression chamber. In this work, to make the indentation, the gasket was placed in a noted orientation on one diamond anvil, and was supported and made level using reusable putty. The two anvils were then brought together and the gasket material was allowed to flow plastically under the action of the anvils, until the desired indentation thickness was reached. The extruded material served as a lateral support for the anvils, as can be generally seen in Figure 3.1. Gaskets used in this work had initial thicknesses of 250 μm and were compressed to give final indentation thicknesses ranging from 50 to 100 μm, as measured with a fine-tipped micrometer (1 μm accuracy). The gasket was then removed to allow the compression chamber to be drilled.

The sample chamber is drilled as close to the center of the indentation as possible. Since the diamond culets are small (300 μm) the chambers have to be even smaller (75 - 125 μm, typically). To make these tiny holes, specialized tungsten carbide (WC) drill bits were required. Drilling of the stainless steel gaskets was done mechanically using a high-precision drill press, where the WC bit was sitting in a v-groove and spun using an o-ring attached to both a small motor shaft and the bit. However, attempts at mechanically drilling rhenium gaskets would simply result in dulling, or breaking, the drill bits and no actual drilling; it is too hard of a material. The solution to this problem is to use spark erosion, or electrical discharge machining. In this work, the WC drill bit was used as an electrode and was still in a v-groove and spun with a motor shaft, but instead carried a large positive potential with respect to the rhenium gasket. The bit was lowered by motorized stages controlled by LabView code. When the separation became small enough to create a sufficiently large electric field, an electrical discharge (spark) occurred and eroded the gasket material, until eventually enough material had eroded to create a hole. The intense heat generated during this process required the use of a dielectric fluid (typically mineral oil), which also served to flush away any loose particles. Each spark was generated with enough energy to erode the material, but not enough to blast the material. The result was a smooth, but slow, cutting action. An example of a resulting drilled gasket is shown below in Figure 3.4.

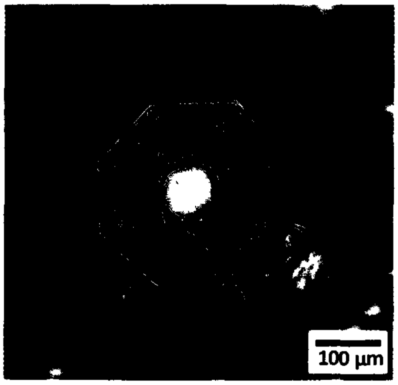

Figure 3.4: Rhenium gasket which has been preindented showing the shape of the diamond culet and drilled using electrospark erosion. The dark material surrounding the compression chamber is comprised of small molten globules of rhenium produced from the drilling process.

Once the gasket was prepared with the sample chamber drilled, it was placed back on the diamond in the same noted orientation used for indentation, ready to be loaded with a sample.

3.1.4 Seats

To couple the diamond anvils to the rest of the cell, they are mounted onto seats. These seats support the table of the diamond, where high stresses can easily cause failure [8, 9], but also restrict the view into the diamond (see Figure 3.1). Consequently, there is a balance between reducing the stress on the diamond table and leaving a large enough aperture through which to conduct experiments. The size of the aperture is also dependent on the material used to construct the seats, and the material, in turn, is dependent on the requirements of the experiments to be performed. Optical experiments require a large opening and so seats made of a very hard and rigid material such as tungsten carbide are used. However, x-ray measurements require the seats to be made of an x-ray transparent material such as beryllium, but since these materials are significantly softer they must support more of the anvil, which results in small apertures. In this work, both optical and x-ray experiments were performed and so the natural solution was to have one beryllium seat and one tungsten carbide seat.

Since the seats are the points of attachment for the anvils, they serve another very important purpose: alignment of the cell. One anvil is attached to a rectangular seat that allows for translational and rotational alignment of the diamonds, while the opposing anvil is attached to a hemispherical seat. This design provides fine-tuning of the tilt to ensure parallelism of the two culets. The translational and rotational alignment was done in the current work by direct viewing using a microscope. However, the parallelism was assessed interferometrically using a sodium lamp by bringing the anvils close together and observing the resultant Fizeau fringes, and the appropriate adjustments were made until no fringes were observed. Well-aligned diamonds were a crucial component of the generation of high pressures, and exceptional care was taken to ensure the best possible stable alignment.

3.1.5 Cell body

Finally, what holds everything together and acts as a small press to apply the required force, is the cell body, the piece with by far the most variability in design. An excellent review of the different design types is given by Jayaraman [10]. Regardless of the specifics, the body provides a steady support for the seats which hold the anvils, and provides a mechanism for bringing the anvils together in a controlled, reproducible manner. In this work, a precisely machined piston-cylinder cell design was used, as shown in Figure 3.5, where the piston is pulled into the cylinder using four screws in order to apply pressure. When assembled, the entire housing is only about 5 cm in diameter and easily fits in the palm of one's hand, which puts an interesting connotation to the common idiom that good things come in small packages.

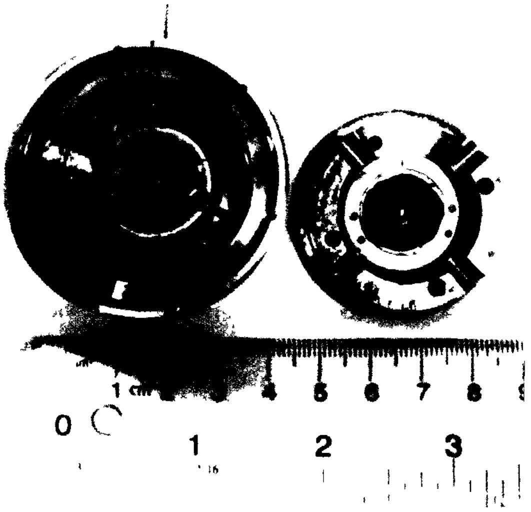

Figure 3.5: One of the diamond anvil cells used in this work showing the cylinder on the left and the piston on the right. The reusable putty (blue) seen around the piston anvil is used to support the gasket (not shown).

3.2 Measuring Pressure

The pressure exerted on the sample by the diamond anvil cell is most commonly determined using the R-line luminescence of ruby (α-Al_2O_3:Cr^{3+}). The Cr^{3+} impurities in the alumina structure introduce several electronic states, including the $^4A_2$ state and the ^2E and $^4T_2$ excited states [11]. The R transition occurs between the first excited state and the ground state ($^4A_2 \leftarrow {}^2E$). The ^2E energy level is further split by both a lowering of the Al^{3+}/Cr^{3+} site symmetry through spin-orbit coupling and crystal-field trigonal distortion caused by the repulsion between neighbouring cations, resulting in the characteristic R_1, R_2 ruby luminescence doublet (Figure 3.6) used in pressure measurement.

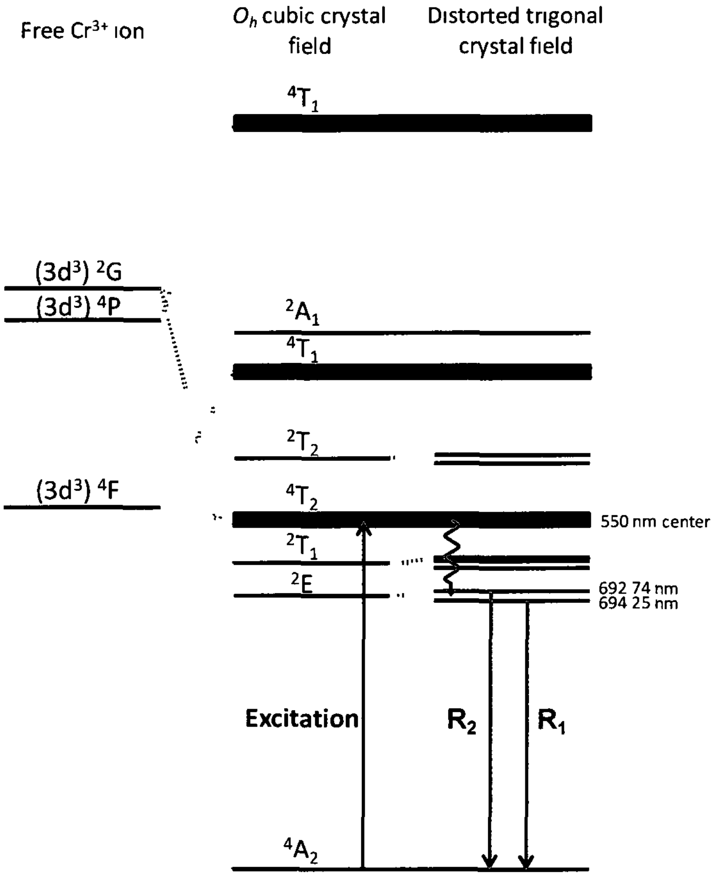

Figure 3.6: Electronic states of Cr^{3+} in ruby (after [11]) showing the R_1, R_2 luminescence doublet used in pressure calibration resulting from laser excitation of the $^4T_2$ excited state.

To observe the R_1, R_2 doublet, the ^2E energy level is populated by exciting the higher $^4T_2$ level which undergoes fast non-radiative decay to the ^2E levels as shown in Figure 3.6. The $^4T_2$ level is centered at 18200 cm^{-1} (550 nm) and is thus easily pumped using, for instance, a doubled Nd:YAG 532 nm laser.

The frequency of this characteristic ruby luminescence changes markedly upon the application of pressure, allowing ruby to be used as an optical pressure calibrant [12]. At moderate pressures ($P < 20$ GPa) the R_1-line fluorescence varies approximately linearly with pressure [12, 13] according to the following relationship:

$$\Delta P(GPa) = 2.740(16) \cdot \Delta\lambda(nm) \tag{3.1}$$

However, at higher pressures, the pressure dependence deviates from linearity and thus a new calibration curve is required. By loading samples containing small ruby crystals along with the powdered form of four metals (Ag, Cu, Mo, and Pd), Mao *et al.* [14] have correlated the ruby R_1-fluorescence with pressures up to 100 GPa derived by the well established equations of state of the standard metals, resulting in the following empirical pressure calibration:

$$P(GPa) = \frac{A}{B}\left[\left(\frac{\Delta\lambda}{\lambda_0} + 1\right)^B - 1\right] \tag{3.2}$$

where A = 1904 GPa, B = 5, λ_0 is the measured wavelength of the ruby R_1 line at ambient pressure, and $\Delta\lambda$ is the measured shift in the wavelength. This relationship remains the standard for non-hydrostatic condition pressure calibration, and is the one used throughout this work. The effect of pressure on the ruby R_1-fluorescence is shown in Figure 3.7.

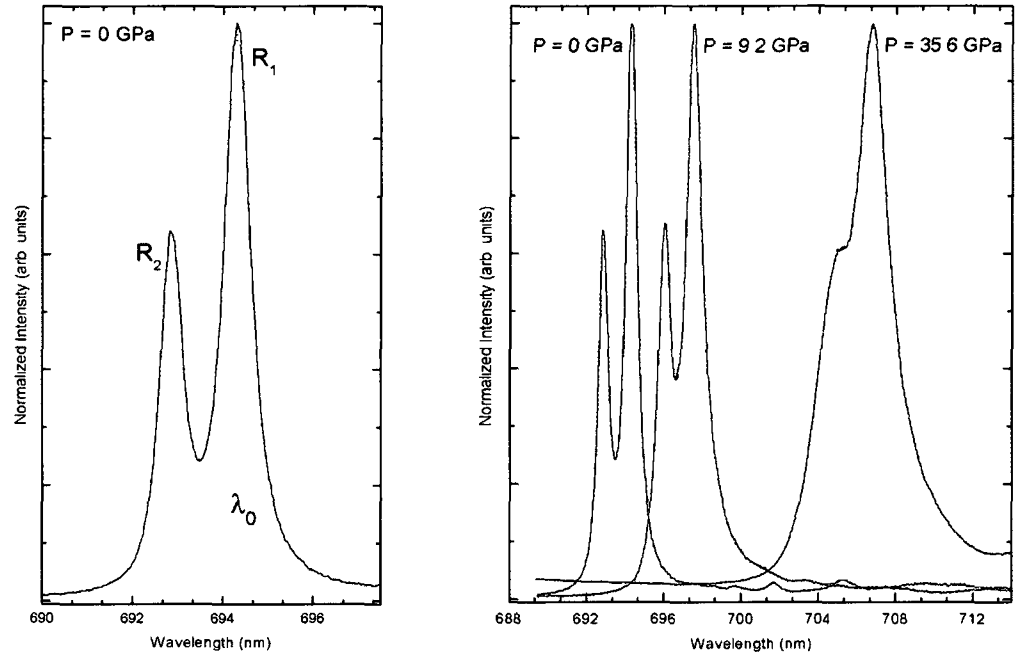

Figure 3.7: Left: The R$_1$, R$_2$ luminescence doublet of ruby at ambient pressure showing λ_0. Right: The intensity-normalized evolution of the doublet with pressure, highlighting the difficulties with strain broadening due to non-hydrostatic pressure conditions.

In 1986, Mao *et al.* [15] presented an improved calibration curve for use with hydrostatic conditions (samples loaded with a pressure transmitting medium), where now in Equation (3.2) the parameter A remains 1904 GPa while B becomes 7.665.

Recently, several more hydrostatic calibration relationships have been proposed to try and better model the curvature of the pressure shift at high pressures (P > 100 GPa). One of the more popular expressions was introduced by Holzapfel in 2005 [16]:

$$P(GPa)=\frac{A}{B+C}\left[\exp\left(\frac{B+C}{C}\left(\left(\frac{\Delta\lambda}{\lambda_0}\right)^{-C}\right)\right)-1\right] \qquad (3.3)$$

where A = 1845 GPa, B = 14.7, and C = 7.5. In the limit that $C \to 0$, Equation (3.3) reduces to the hydrostatic case of Equation (3.2). A comparison of the four presented pressure calibration models over the range of pressures used in this work is given below in Figure 3.8.

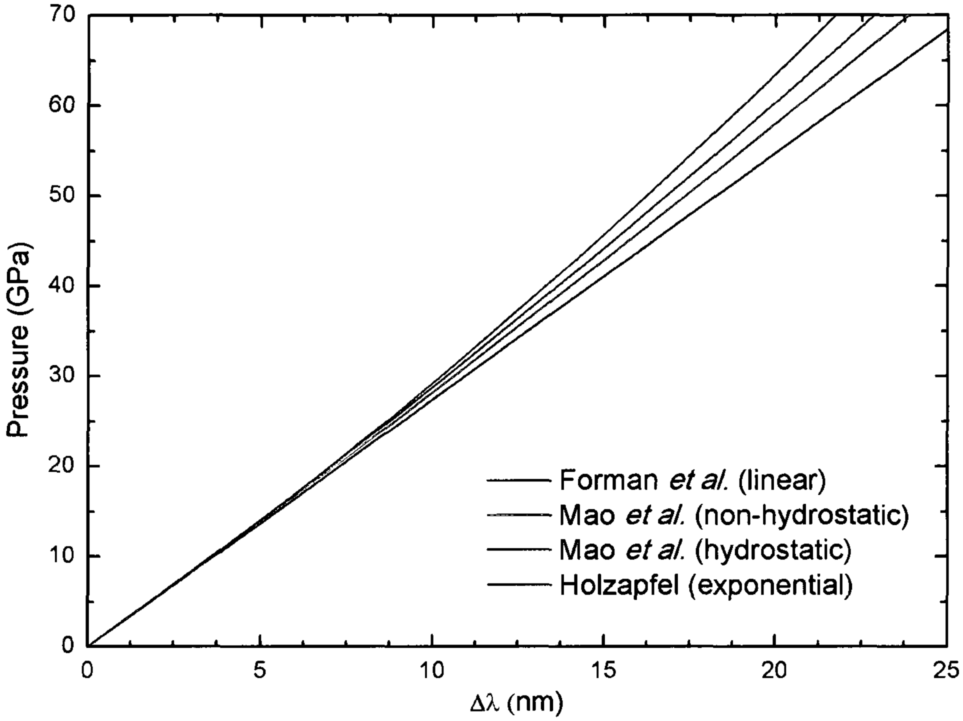

Figure 3.8: A comparison of four common relationships describing the pressure shift of the R_1-fluorescence line of ruby $(\lambda_0 = 694.25nm)$ over the range of pressures used in this work.

Along with some debate over the best calibration curve to use, there are some additional complexities associated with using ruby as a pressure calibrant. Firstly, at high pressures the R_1 and R_2 lines can become severely broadened due to both non-hydrostatic conditions and non-uniform stress, as seen in Figure 3.7. In this work, micro ruby spheres (diameters < 15 μm) were used, and so one can imagine that at high pressures, the strain at the two poles closest to the anvils would be considerably higher than at the equator in the middle of the sample chamber. This resulted in a significant shift in the R_1-line frequency depending on where on the ruby sphere the luminescence was recorded. So despite being able to measure the frequency accurately, the measurement was limited by the precision (variations of up to 10% were seen at pressures of about 60 GPa). At high pressures, it is generally seen that not only do the R-lines become broadened, they also become considerably weaker. The $^4T_2$ energy level used to populate the ^2E levels blue-shifts with pressure such that, at high pressures, excitation with the doubled Nd:YAG 532 nm laser becomes increasingly inefficient [11]. This causes a decrease in emission intensity where, eventually, at about 100 GPa, excitation can no longer be done using the green laser. In that case, the shorter wavelength Ar ion laser (488 nm) should be used.

3.3 Vibrational Raman Spectroscopy

One important tool that is well adapted for the study of materials at high pressure is vibrational Raman spectroscopy. This provides a measure of the characteristic vibrational frequencies of the bonds and molecular groups that make up the chemical compound. With applied pressure, if there is a discontinuity in the pressure evolution of these modes, it would indicate a change in the molecular bonding. Thus, Raman spectroscopy can relatively quickly provide an overview of the behaviour of the sample with increased pressure and identify structural phase transitions which can then be studied further using powder x-ray diffraction. This section will outline the process of Raman scattering and the experimental setup used to acquire the Raman spectra presented in this work.

3.3.1 Raman scattering

When subjected to monochromatic radiation, a sample can interact with the incident photons through many different processes, including scattering. This scattering can either be elastic (no energy being transferred) or inelastic (energy being transferred), known as Rayleigh or Raman scattering, respectively. While much less infrequent (only about 1 event in 10^6), Raman scattering gives important information about the material with which the incident photons interact. During inelastic scattering events in crystalline materials, the incident photons can either gain energy through absorption of a phonon (anti-Stokes radiation) or lose energy through emission of a phonon (Stokes radiation). The energy exchanged is independent of the incident wavelength used, and is given by the phonon energies, which are a direct measure of the characteristic vibrational modes of the material. The conservation of energy gives the following relationship:

$$h\nu_S = h\nu_I \pm h\nu_{vib} \tag{3.4}$$

where ν_I is the incident photon frequency, ν_S is the scattered photon frequency after interaction with a phonon, and ν_{vib} is a characteristic vibrational frequency of the material. The top (+) sign represents the anti-Stokes radiation, while the bottom sign (-) represents the Stokes radiation. These two processes are illustrated below in Figure 3.9.

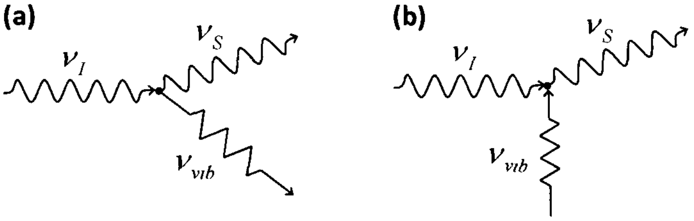

Figure 3.9: Raman scattering diagrams of the incident photon of frequency ν_I interacting with the material by (a) emission of a phonon of frequency ν_{vib} (Stokes) and (b) absorption of a phonon of frequency ν_{vib} (anti-Stokes).

Classically, the vibrational Raman effect is explained by the interaction of a molecule with an electric field. The electric field component of the incident electromagnetic radiation induces a dipole moment in the molecule which is given by

$$\vec{\mu}_{ind} = \vec{\alpha} \cdot \vec{E} \tag{3.5}$$

where $\vec{\alpha}$ is the polarizability tensor characteristic of the molecule and $\vec{E}$ is the electric field felt by the molecule. The magnitude of the electric field can be expressed as

$$E = E_0 \sin(2\pi \nu_l t) \tag{3.6}$$

The internal vibrational motion of the molecule couples to the oscillating induced dipole, resulting in a modulated polarizability, given by

$$\alpha = \alpha_0 + \alpha_1 \cos(2\pi \nu_{vib} t) \tag{3.7}$$

where α_0 is the static polarizability and α_1 is the derivative of the polarizability with respect to the vibrational motion. Together this gives an induced dipole moment of

$$\begin{aligned} \mu_{ind} &= \alpha E = \left(\alpha_0 + \alpha_1 \cos(2\pi \nu_{vib} t)\right)\left(E_0 \cos(2\pi \nu_l t)\right) \\ &= \alpha_0 E_0 \cos(2\pi \nu_l t) + \frac{\alpha_1 E_0}{2}\left[\cos\left(2\pi(\nu_l - \nu_{vib})t\right) + \cos\left(2\pi(\nu_l + \nu_{vib})t\right)\right] \end{aligned} \tag{3.8}$$

Now it can be easily seen that the presence of the Raman Stokes lines $(\nu_l - \nu_{vib})$ and anti-Stokes lines $(\nu_l + \nu_{vib})$ is directly dependent on how the molecule's polarizability changes with the vibrational motion (α_1). If α_1 is 0, there will be no Raman scattering, only the ν_l Rayleigh scattering will be present. Thus, the number of vibrational modes that are Raman-active is solely determined by the number of atoms and the symmetry of the molecule. However, the specific frequencies and intensities of these modes are much more complex as they depend on a wide variety of parameters such as state populations, polarizability derivatives, vibrational partition functions, differential scattering cross sections, etc. [17].

The collection of vibrational modes (the Raman spectrum) of a material provides a wealth of information about the bonding arrangement of the molecules, which can provide a clue to the overall crystal structure. As pressure is applied to the crystal, the system energy is increased which typically leads to increased vibrational frequencies. The evolution of the Raman spectrum with increased pressure gives an indication of how the molecules are being affected by pressure. If any drastic changes are seen (appearance or disappearance of modes) it would suggest either a change in molecular symmetry or the creation or destruction of bonds within the molecule. And thus, Raman spectroscopy can give a quick indication of a phase transition which can then be corroborated and further studied using x-ray diffraction. Furthermore, in principle, an analysis of the polarization of the Raman scattered photons from an oriented single crystal can lead to the determination of the crystal symmetry.

3.3.2 Experimental setup

Raman spectroscopy measurements were performed in the current work by exciting the sample with a Centennia TD5 532 nm doubled Nd:YAG continuous wave laser. The laser was typically run at 200 mW, but a series of optical filters were used in order to maintain a power level of approximately 5 mW at the focal point to avoid photo-induced reaction of the sample. The laser was focussed on the sample using an Olympus BH-2 microscope with a 50X (N.A 0.42) Mitutoyo objective with a long working distance. To make sure the laser was incident and focussed on the sample, the diamond anvil cell was mounted in a holder which was then attached to an x,y,z-stage to allow for micrometric positional adjustments. The positioning was done using a CCD video camera connected to a viewing monitor.

The Raman data were collected in a 180° backscattering geometry, meaning the scattered light was coaxial to the incident laser and was collected and focussed using the same 50X objective used to focus the laser. The focussed scattered light was then passed through a beam splitter, a laser line rejection filter, then steered using various highly reflective coated mirrors and finally focussed onto an optical fibre. This fibre carried the scattered light to an Andor Shamrock SR-303i spectrograph where it was dispersed using an 1800 grooves/mm grating. This grating gave a resolution of 0.05 nm, or 1.5 cm^{-1} at 575 nm. The dispersed light was then collected with an Andor iDus DU401-BRDD CCD camera, and the resulting Raman spectrum was acquired using Andor Solis software. Spectral calibration was performed using a third-order polynomial fit of known Ne emission lines to within ±1 cm^{-1}. The experimental configuration described above is shown below in Figure 3.10.

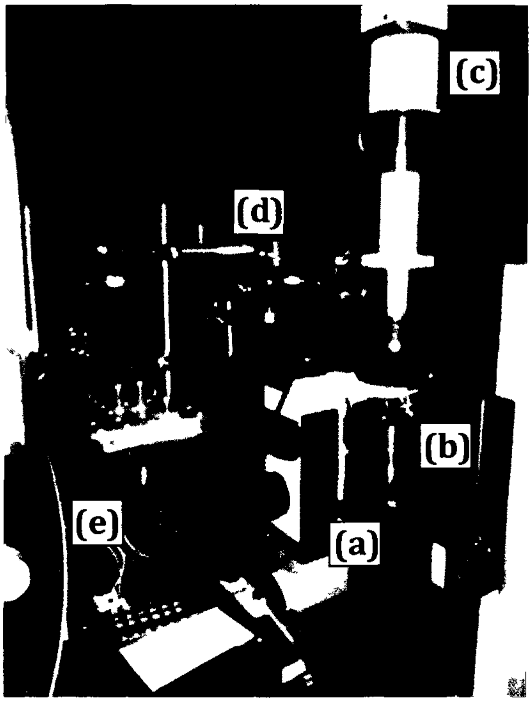

Figure 3.10: Raman spectroscopy experimental setup showing (a) the diamond anvil cell mounted in a holder attached to a 3-way stage, (b) the 50X objective to focus the incident laser and collect the scattered light, (c) the CCD video camera for sample viewing, (d) the arrangement of steering and focussing optics, and (e) the optical fibre carrying the Raman signal to the spectrograph (not shown).

3.4 Angle-Dispersive Powder X-Ray Diffraction Using Synchrotron Radiation

Another tool that is vital to the study of materials at high pressure is x-ray diffraction. While some information about the occurrence of phases is determined from Raman spectroscopy, the full pressure-volume (P,V) phase diagram is constructed using x-ray diffraction. The acquired characteristic diffraction patterns are used to extract the structures and properties of the phases. In this work, all of the x-ray diffraction experiments were done using polycrystalline (powder) samples, were collected as a function of 2θ (angle-dispersive), and were performed using synchrotron radiation at the Hard X-ray MicroAnalysis (HXMA) beamline at the Canadian Light Source (CLS). In the following section, a brief introduction to x-ray diffraction is given, followed by an outline of the experimental setup used at the CLS, and the acquisition and analysis techniques used to extract the required information from the observed diffraction images.

3.4.1 A brief introduction to x-ray diffraction

X-ray diffraction is an elastic scattering process where the incoming x-rays interact with electrons surrounding the nuclei that make up a crystal. The crystal is a structured array of atoms or ions (lattice) constructed of periodically repeated building blocks (unit cells). The unit cell, which describes the overall crystal symmetry, is described using six lattice parameters - three cell lengths (a, b, and c) and three angles (α, β, and γ), as shown in Figure 3.11. Based on the symmetries of these parameters, the unit cells are classified into 14 different groups called Bravais lattices.

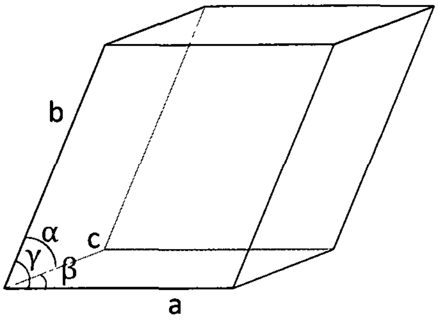

Figure 3.11: A generalized unit cell showing the six lattice parameters - the cell lengths a, b, and c, along with the three angles α, β, and γ between (**b** and **c**), (**a** and **c**), and (**a** and **b**), respectively.

When monochromatic x-rays are incident upon a periodic crystal they are scattered, and under certain special conditions they can constructively interfere. The condition of constructive interference is described by Bragg's law:

$$2d\sin\theta = n\lambda \qquad (3.9)$$

where d is the lattice plane separation, θ is the angle between the plane and the incident x-rays, n is an integer, and λ is the x-ray wavelength. If the path length travelled by the x-rays ($2d\sin\theta$) is equal to an integer multiple of the x-ray wavelength, the x-rays will be reflected (Bragg reflection). This is described graphically in Figure 3.12.

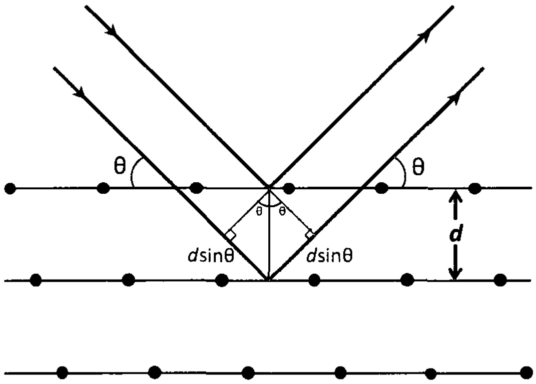

Figure 3.12: Graphic illustration of Bragg's law. Incident x-rays are scattered off of crystal planes separated by a distance *d*, and will only constructively interfere if the incident angle is such that the path difference (2*d*sinθ) is an integer multiple of the incident x-ray wavelength.

In the above figure, only one set of planes is shown, but there are many different ways to arrange the lattice into planes, and each would have a corresponding *d*-spacing and a resulting diffraction angle (note that relative to the incident x-rays, the diffracted x-rays actually occur at 2θ). Within a crystal the sets of planes are described by where they intersect the unit cell edges. If a plane intercepts **a**, **b**, and **c** at a/*h*, b/*k*, and c/*l*, respectively, then that plane is labelled as {hkl} where the values, known as Miller indices, are scaled to give integer values (for example {½10} would be reported as {120}). The fully generalized value of the d-spacing for a plane {hkl} is given by

$$\begin{aligned} d_{hkl} = V\ \big[&h^2b^2c^2\sin^2\alpha + k^2a^2c^2\sin^2\beta + l^2a^2b^2\sin^2\gamma \\ &+ 2hlab^2c(\cos\alpha\cos\gamma - \cos\beta) + 2hkabc^2(\cos\alpha\cos\beta - \cos\gamma) \\ &+ 2kla^2bc(\cos\beta\cos\gamma - \cos\alpha)\big]^{-1/2} \end{aligned} \tag{3.10}$$

where *V* is the volume of the unit cell, given by

$$V = abc\sqrt{1-\cos^2\alpha - \cos^2\beta - \cos^2\gamma + 2\cos\alpha\cos\beta\cos\gamma} \tag{3.11}$$

Thus, the set of lattice parameters that uniquely describes the unit cell (a, b, c, α, β, and γ) defines the set of all theoretically possible Bragg reflections and their corresponding 2θ values. The resulting diffraction peaks are typically referred to as reflections, and are indexed as (*hkl*) according to the Miller indices of the originating planes.

For a single crystal, the diffraction condition is only satisfied when a plane is in the proper orientation with respect to the incident beam. This leads to individual Bragg spots corresponding to the different planes. Single crystal x-ray diffraction is thus a very powerful technique for solving the crystal structure, however, it is not always possible to obtain a single crystal and the majority of high pressure x-ray diffraction is performed using powders, including in this work. A powder is made up of many tiny crystallites with, ideally, completely random orientations such that the Bragg condition will be satisfied for each possible *d*-spacing (as long as $2d > \lambda$). The result is that one single sample orientation in a fixed x-ray beam will give the entire set of possible Debye diffraction cones which are imaged two-dimensionally as Debye rings. The radius of each ring will be the 2θ value corresponding to a particular (*hkl*) reflection.

It has been clearly shown that the positions of the diffraction peaks (given by either *d*-spacings or 2θ values for a given incident wavelength) are solely dependent on the lattice parameters and therefore, the geometry of the unit cell. However, the intensities of these diffraction peaks depend on many more factors, including the composition of the unit cell - the type, number, and positions of all atoms or ions. The effect of the composition on the scattering process is described by a quantity, S_{hkl}, known as the structure factor [18]. This quantifies the diffraction intensity attenuation of the (*hkl*) reflection due to interference from identical atoms within the unit cell, and is given by

$$S_{hkl} = \sum_{j=1}^{N} f_j e^{2\pi i\left(hx_j + ky_j + lz_j\right)} \tag{3.12}$$

where f_j is the atomic form factor for atom *j*, and x, y, and z are fractional positional coordinates of atom *j* in the unit cell. The overall integrated intensity of the (*hkl*) diffraction peak is proportional to the square of the absolute value of S_{hkl}, that is $I_{hkl} \propto | S_{hkl} |^2$ and its full form [19] is given by

$$I_{hkl} = I_p K \lambda^2 V^{-2} m_{hkl} P L v \left|S_{hkl}\right|^2 \tag{3.13}$$

where I_p is the beam intensity; *K* is a factor dependant on the type of diffraction (neutron or x-ray) performed; m_{hkl} is the multiplicity of the (*hkl*) reflection; *P* is a polarization factor given by

$$P = \frac{1+\cos^2\theta \cdot \cos^2\theta_m}{1+\cos^2\theta_m} \tag{3.14}$$

where θ_m is the Bragg angle of the monochromator; L is the Lorentz factor and for a random powder is given by

$$L = \left(\cos\theta \sin^2\theta\right)^{-1} \tag{3.15}$$

and finally, v is the effective diffracting volume of the sample. While complex, the intensities of the peaks making up the diffraction pattern can be used to extract the atomic positions constituting the unit cell which is first determined using the peak positions.

The peak intensities hold a lot of valuable structural information, but can unfortunately be quite problematic for powder diffraction. For example, if two planes have very similar *d*-spacings their Debye rings will overlap and the intensities of two reflections may not be able to be correctly partitioned. Furthermore, the sample being studied might not always be a perfectly isotropic powder; there may be one orientation that is favoured over the others, a phenomenon known as preferred orientation. This can cause the integrated intensities to be very misleading, and can even prevent certain reflections from being observed. While this may not impact the ability to determine the unit cell, it can certainly become a complex problem when trying to solve the full structural solution. Despite such challenges, powder x-ray diffraction remains an extremely useful tool for the characterization of materials.

3.4.2 Necessity of synchrotron radiation use

Synchrotron radiation is generated by accelerating particles (typically positrons or electrons) through magnetic and electric fields to very near the speed of light. This radiation, when arising in the right part of the electromagnetic spectrum, is both beneficial and necessary to perform x-ray diffraction measurements with a diamond anvil cell. For any x-ray measurement, the incident and reflected x-rays have to pass through a pair of nearly 2 mm-thick diamond anvils. Since diamond only becomes transparent to x-rays at high energies, the radiation produced by conventional lab sources, such as a copper x-ray tube, will actually be almost entirely absorbed by the anvils. However, one important property of synchrotron radiation is that the wavelength is easily tuneable with the use of monochromators, which allows the selection of hard (high energy, small wavelength) x-rays which are almost entirely transmitted through the anvils. The x-ray transmission curve of diamond is shown in Figure 3.13.

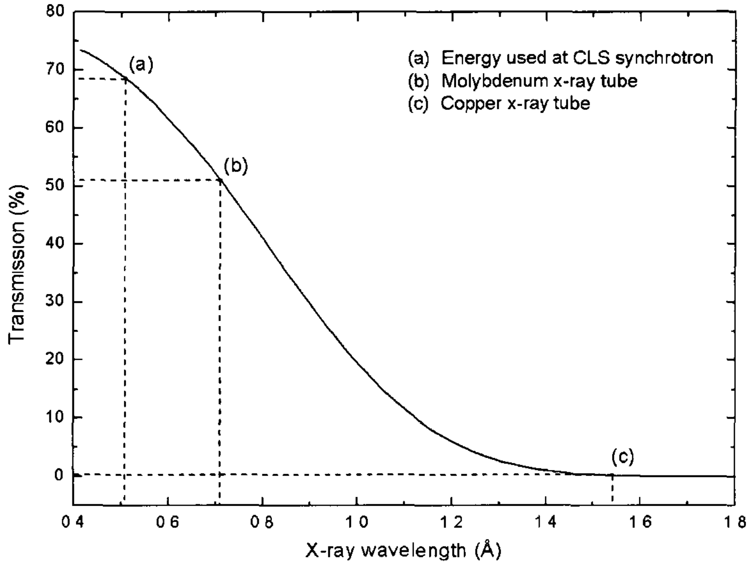

Figure 3.13: X-ray transmission through 4 mm of diamond as a function of x-ray wavelength showing the need for a high energy (small wavelength) x-ray source [20].

The synchrotron generation of hard x-rays has an additional benefit. According to Bragg's law (Equation 3.9), with increased x-ray energy (decreased wavelength) the *d*-spacings will decrease. The aperture created by the anvil seats (see Figure 3.1) limits the observable 2θ range to a maximum of approximately 30°, which then limits the accessible range of *d*-spacings. For a good structural determination, a minimum *d*-spacing of at least 1.5 Å is needed, and in some cases, 1 Å *d*-spacings are required. For the synchrotron radiation used in this work (24.350 keV, or 0.509176 Å) a 1.5 Å *d*-spacing corresponds to 19.5° 2θ, which is easily observable with the diamond anvil cell (DAC). However, if a typical copper x-ray tube (8.042 keV, or 1.5418 Å) is used, a 1.5 Å *d*-spacing would correspond to 61.9° 2θ. In fact, for the copper source the minimum *d*-spacing that can be observed in the DAC is 2.98 Å, which would most certainly preclude any definite structural solution.

The benefits of using hard x-rays (including high transmission through diamond and large range of accessible *d*-spacings) can also be achieved, to some extent, with the higher energy x-ray tubes, such as one with a molybdenum target. However, one major difference between synchrotron and laboratory sources is the sheer number of photons produced. The most common way to quantify this is through the measure of brilliance, the peak flux density in phase space where the photon flux is the number of photons emitter per second, per mrad, per 0.1% bandwidth (BW) [21]. The lab source sealed x-ray tubes have a brilliance on the order of 10^8 photons/s/mm^2/mrad^2/0.1%BW [22, 23], while the synchrotron source used at the CLS is on the order of 10^{17} photons/s/mm^2/mrad^2/0.1%BW [24]. Since the compression chamber of the pressure cell is small (typically 75 μm in diameter and 75 μm thick) there is a very limited amount of sample to scatter off of, and thus having a high-brilliance x-ray beam is exceptionally beneficial.

Due to the ultrarelativistic nature of the electrons travelling in the storage ring, the synchrotron radiation produced has a very low divergence in the plane of travel (on the order of 0.1 mrad). This allows for very small, parallel x-ray beams, a property that is very useful when working with microscopic-sized samples as the unwanted radiation incident on the surrounding metallic gasket is minimal. While for many reasons the use of synchrotron radiation for x-ray diffraction measurements is necessary, it also has several additional properties that contribute to its many advantages.

3.4.3 Experimental configuration at the Hard X-ray MicroAnalysis Beamline of the Canadian Light Source

All of the x-ray diffraction experiments presented in this work were performed at the Hard X-ray MicroAnalysis (HXMA) 06ID-1 beamline at the Canadian Light Source (CLS) in Saskatoon, Saskatchewan. The CLS is a third generation synchrotron source with electrons accelerated to a final energy of 2.9 GeV. The HXMA beamline uses an alternating 63-pole, 2 Tesla superconducting wiggler insertion device which provides the acceleration needed to produce synchrotron electromagnetic radiation (hard x-rays) from the high energy electron beam.

To focus and collimate the generated radiation and to select the desired x-ray energy, the beam passes through a mirror-mono-mirror configuration. The two mirrors are specially designed to reflect and focus high energy x-rays in both the horizontal and vertical planes. Between the two mirrors is a double crystal monochromator. It uses a pair of silicon (111) or (220) single crystals which selects the desired wavelength, and therefore energy, by changing the angle of the crystals (for a fixed *d*-spacing the Bragg condition is a simple relationship between the angle of incidence and the wavelength).

The beam is then collimated further using a sequence of motorized slits. This allows some extraneous scattering to be absorbed while maintaining a high photon flux. The beam then enters an ion chamber where the scattering is recorded and used to measure the intensity of the beam. This ion chamber signal is crucial to energy calibration. In this work a thin foil of palladium was inserted in the beam path. The monochromator crystal angle is then scanned and the resulting x-ray absorption spectrum of Pd is recorded using the ion chamber signal. This allows the Si (111) monochromator to select the precise energy of 24.350 keV, given by the known K-edge of Pd [25].

After the ion chamber, the energy calibrated x-ray beam enters a beam pipe. This pipe is filled with helium to reduce unwanted scattering from air, and surrounds the beam up to the experimental table (see Figure 3.14 and Figure 3.15).

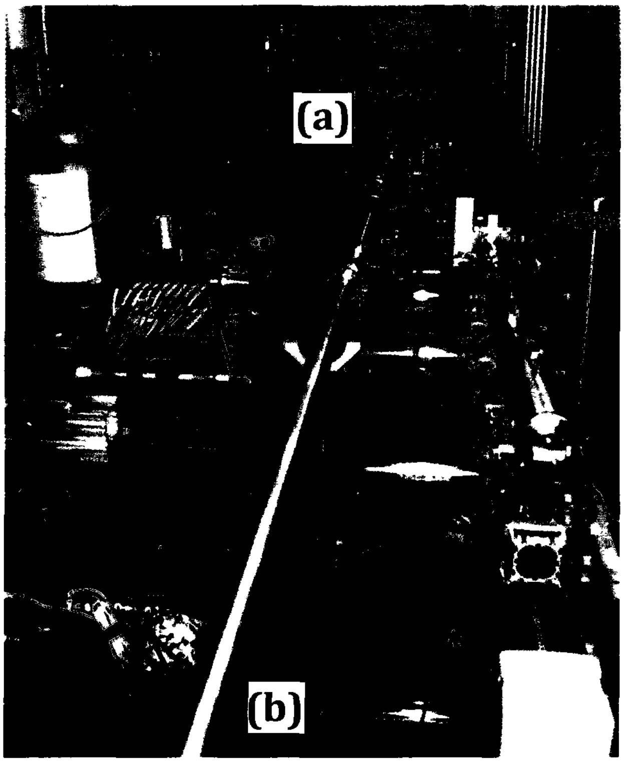

Figure 3.14: Experimental configuration at the HXMA beamline showing (a) the ion chambers used for energy calibration, and (b) the helium-filled beam pipe that provides a minimal-scattering environment for the x-ray beam.

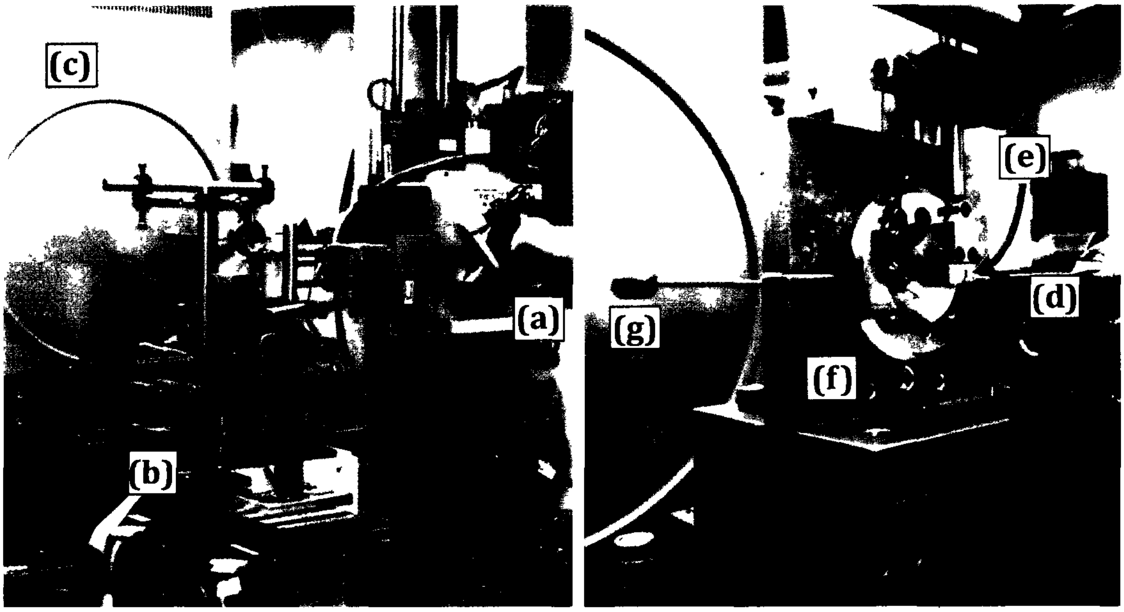

Figure 3.15: Experimental table setup used at HXMA showing (a) the end of the beam pipe, (b) the sample goniometer, (c) the mar345 imaging plate detector, (d) the collimator, (e) the cleanup aperture, (f) the diamond anvil cell in a holder, and (g) the beamstop assembly.

Once at the experimental table, the beam size was reduced by passing through a custom 30x30 μm^2 square aperture tungsten carbide collimator. The beam was further refined using a cleanup aperture made from indented rhenium 120 μm thick, with a 60 μm hole drilled through the center. The thickness of the rhenium was such that it absorbed stray scattering so that the beam was only incident upon the sample, reducing the diffraction signal from the gasket material. The beam then passed through the diamond anvil cell which was mounted on a goniometer constructed from five high-precision motorized stages (four translational and one rotational). The resultant diffracted beam then encountered a beamstop to prevent saturation and damage to the detector from the transmitted (non-diffracted) beam. The brass beamstop assembly seen in Figure 3.15 contained a lead plug to block the beam as well as a small silicon PIN diode used to measure the intensity of the transmitted beam. And finally, the diffraction from the sample was collected on a Marresearch mar345 imaging plate detector characterized by a large (345 mm diameter) detection area and a high-resolution readout (100x100 μm^2 pixel size). All this apparatus, while seemingly cumbersome, allowed for a relatively straightforward process for the collection of high-resolution angle-dispersive powder x-ray diffraction images. Further details are presented by Smith and Desgreniers [26].

3.4.4 Data acquisition and processing

The experiments in this work were performed in a transmission geometry, as shown below in Figure 3.16. To generate a typical diffraction pattern from a two-dimensional diffraction image, the intensities were integrated over the Debye rings and the positions of the acquired rings were converted to their corresponding 2θ values. To do so, an accurate value of the sample-to-detector distance had to be known.

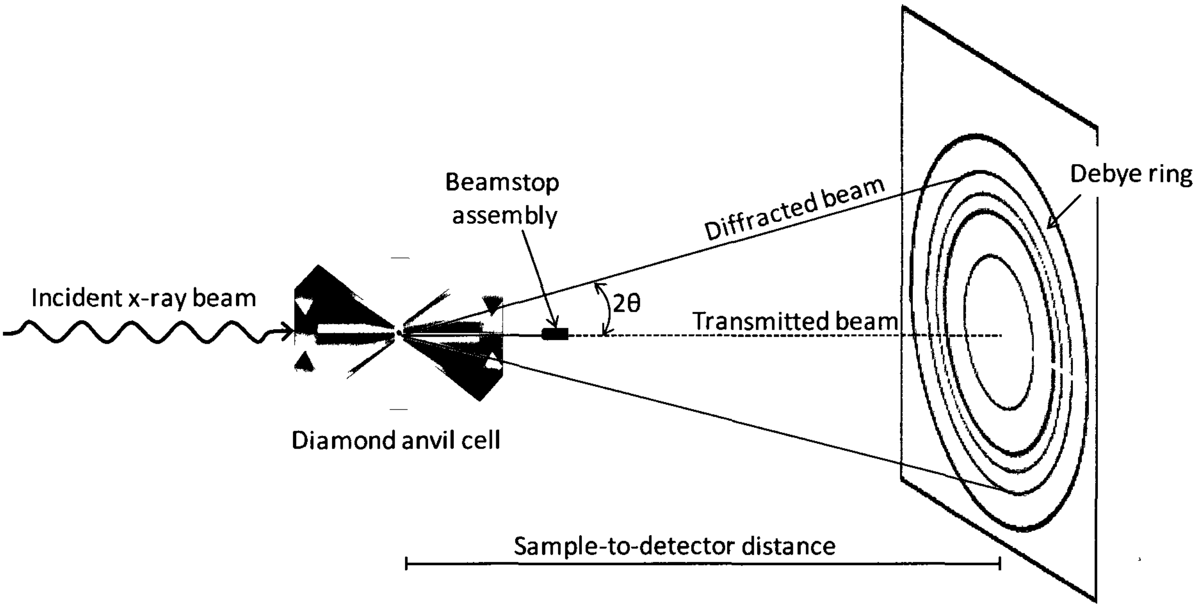

Figure 3.16: Transmission geometry used to collect angle-dispersive x-ray diffraction data at the HXMA beamline at the Canadian Light Source.

To determine this distance and calibrate the collected images, diffraction from a lanthanum hexaboride, LaB_6, standard was used (National Institute of Standards and Technology, Reference Material 660a). The Debye rings of the standard were integrated using Fit2D software [27] and the resulting diffraction peaks were compared to the known positions in order to calculate the sample-to-detector distance. Furthermore, since the transmitted beam was not necessarily centered on, or perpendicular to, the area detector, the resulting eccentricity of the Debye rings of LaB_6 was used by the software to define the beam center and to correct for tilt and rotation of the area detector with respect to the incident beam. This calculated set of integration parameters was then used to calibrate the subsequent images, assuming the area detector remained fixed with respect to the beam; however, the sample needed to be placed at the same position as the standard for the calibration to be applicable. This was achieved by passing beam through the center of the sample, which was placed at the center of rotation of the goniometer.

The holders for the standard and the diamond anvil cells were custom-built to ensure a roughly constant sample position, while the positioning was finely tuned using the motorized stages making up the goniometer. The motion of these stage motors was controlled by specialized LabView codes, and gave a positioning accuracy and repeatability to within 1 μm. Once the sample was placed on the goniometer it was centered by scanning the sample through the fixed beam and monitoring the transmitted intensity recorded by the silicon PIN diode. Since the sample and the gasket have different x-ray absorption characteristics, the sample chamber was easily identified (see Figure 3.17).

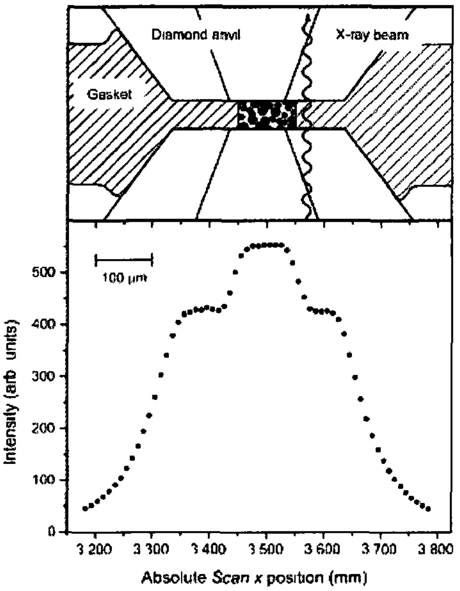

Figure 3.17: Transmitted intensity profile resulting from moving the diamond anvil cell through the incident beam, easily identifying the sample position within the DAC. Figure courtesy of S. Desgreniers.

Once the sample stage was positioned such that the beam passed through the center of the sample chamber, the rotation center of the sample was determined. This was done by recording the transmitted intensity profiles at three different sample rotation angles. The difference in profiles over these angles allowed for the calculation of the center of rotation [26].

Placing the sample at the center of rotation also allowed for rocking of the sample during data acquisition, where the sample was rotated through a small angle about the center of rotation. This process was exceptionally useful as it substantially improved the data quality [26]. As the sample was rotated, the incident x-ray beam encountered a greater number of crystallite orientations. This had two major benefits. Firstly, the counting statistics were improved, producing a more uniform intensity distribution along the Debye rings, which served to improve the resolution of the resulting diffraction peaks. Constantly changing the orientation of the crystallites also reduced the amount of detector saturation, which provided a more accurate integrated intensity.

Once the best possible diffraction images were acquired and the appropriate calibration parameters were determined, the previously mentioned Fit2D software was used to integrate the intensity of the Debye rings to give a traditional diffraction pattern displaying intensity versus 2θ. The relation between the image and the resulting pattern is shown in Figure 3.18. The integrated diffraction profiles were then exported and ready to be analyzed.

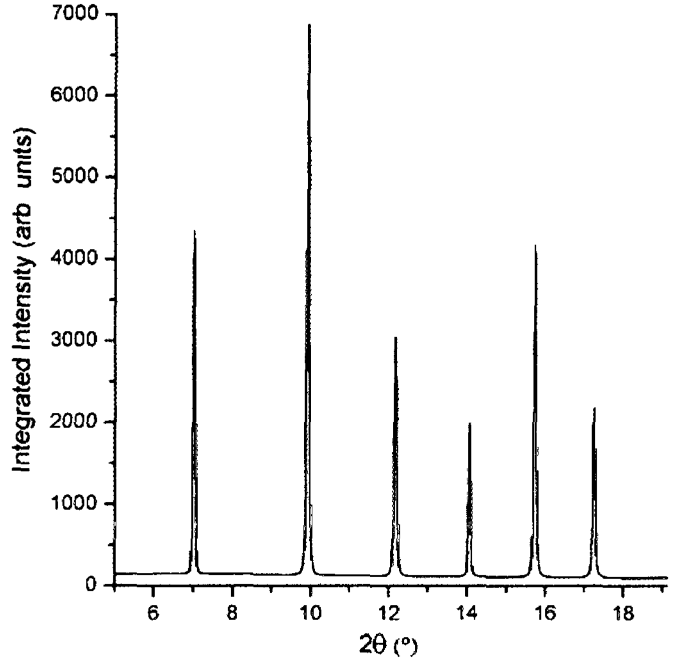

Figure 3.18: Section of the integrated diffraction pattern of LaB_6 clearly showing the relationship between the acquired Debye rings (background) and the integrated pattern (foreground).

3.4.5 Diffraction pattern analysis

To extract properties of the material being studied, the unit cell must first be determined from the diffraction pattern by assigning the observed peaks their correct Miller indices. To do so, the integrated data is opened in an indexing program, XRDA [28], where the peaks are first fit to Gaussian profiles, creating a list of observed *d*-spacings. If the crystal structure of the sample is known (for example, if it has been well-characterized at ambient conditions), then the unit cell information (Bravais lattice and lattice parameters) is entered into the XRDA program. Based on that information, the set of expected reflections with their respective *d*-spacings is generated and superimposed on the experimental data. The observed diffraction peaks can then easily be given the proper set of (*hkl*) values, and a least-squares fitting routine is performed to extract the experimental lattice parameters.

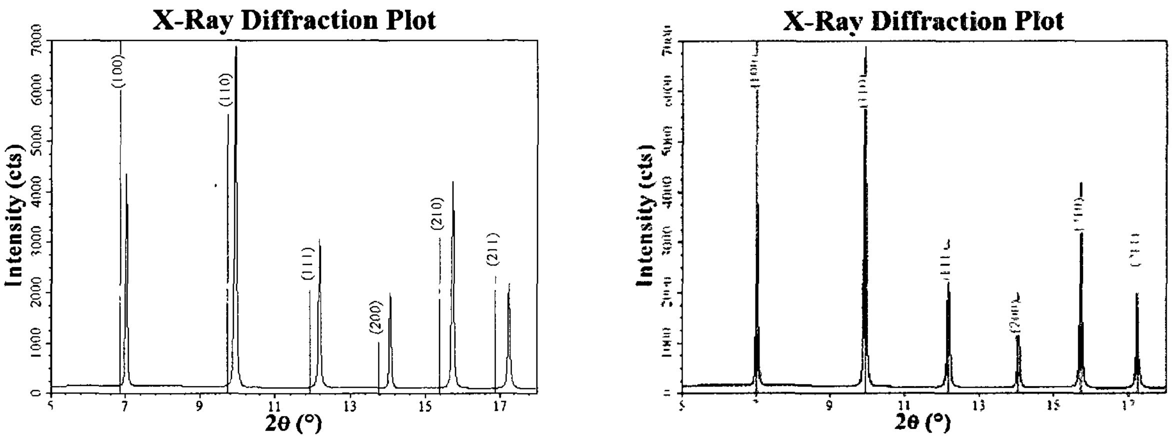

Figure 3.19: Example of the unit cell indexing and fitting procedure using the first few peaks of LaB_6. The plot on the left shows the calculated *d*-spacings for an initial unit cell guess. The plot on the right shows the result of the least-squares fit of the observed peaks, showing the calculated *d*-spacings arising from the refined unit cell parameters.

In most cases, especially when phase transitions are encountered, no information is known about unit cell prior to the experiment, and identifying a Bravais lattice, let alone a unit cell, is virtually impossible by merely observing the diffraction pattern. In this case, trial-and-error approach is needed, and can be quite arduous. This process can be aided by using an indexing software package such as CRYSFIRE [29] that can be used to generate possible unit cells and volumes. CRYSFIRE presents a comprehensive collection of software tools which use specialized algorithms to search through a large number of unit cells in order to identify structures that can best match the observed *d*-spacings. The candidate structures are ranked by figure of merit, a numerical representation factoring in how well the calculated and observed peak positions agree as well as the number of reflections present in the given 2θ range [30]. The proposed unit cells must then be checked against the experimental data to verify that all of the reflections can be accounted for with a minimal number of unobserved peaks. If a suitable unit cell has been identified, the lattice parameters (and therefore, unit cell volume) can be fit using XRDA, as described above. The final step in determining the structure is to identify the space group. The different space groups are characterized by the symmetries and positions of the atoms within the unit cell that lead to systematic variations in peak intensities and even absences of reflections. Programs such as Chekcell [31] can assist with this process, but it is important to note that space group assignment may not be possible, especially at high pressures where non-hydrostatic conditions and preferred orientation can cause misleading reflection intensities.

If the space group is known, the parameters extracted from the structural determination can be further refined using full pattern refinement techniques such as the Le Bail [32] and Rietveld [33] methods. These methods converge on a fit by minimizing the difference between observed and calculated patterns using least-squares routines. The full pattern refinements performed in this work were carried out using the FullProf [34] suite. The intricacies of these methods are beyond the scope of this work and are fully detailed elsewhere (reference [35], for example), but a very brief overview is given below.

Instead of just fitting the individual diffraction peaks, the Le Bail procedure refines several parameters to describe the full profile such as the background, the unit cell parameters, and the peak shape parameters. The benefit of the Le Bail method is that the reflection intensities, which are dependent on the structural model, are simply treated as variables. This allows a full pattern fit without any knowledge of the atomic positions. If these positions are known, then a full Rietveld refinement can be performed where now the intensities are calculated from the structural information. This process extracts and refines the same parameters as the Le Bail method, with the addition of the proper intensities and therefore the atomic positions. Since the Le Bail process typically converges much easier, it is common to use the results from the Le Bail fit as starting parameters for the more robust Rietveld refinement. One common difficulty that arises in Rietveld fits of diffraction data acquired using a diamond anvil cell is that the peaks do not have enough intensity to allow the atomic positions to be varied. This is especially true for weak scattering atoms, and in those cases a full Rietveld refinement is usually impossible, and thus the best possible full pattern fit to the experimental data would be achieved using a Le Bail fit.

References

[1] C.E. Wier, E.R. Lippincott, A. van Valkenburg, and E.N. Bunting, *J. Res. Natl. Bur. Stand.* **63A**, 55 (1959).

[2] J.C. Jamieson, A.W. Larson, and N.D. Nachtrieb, *Rev. Mod. Phys.* **30**, 1016 (1959).

[3] M.I. Eremets, *High Pressure Experimental Methods* (Oxford University Press, New York, 1996).

[4] J. Xu and H. Mao, *Science* **290**, 783 (2000).

[5] J. Xu, H. Mao, R. J. Hemley, E. Hines, *J. Phys.: Cond. Mat.* **14**, 11543 (2002).

[6] J. Xu, S. Yeh, J. Yen, E. Huang, *J. Raman Spec.* **27**, 823 (1996).

[7] J. Xu, J. Yen, Y. Wang, E. Huang, *High Press. Res.* **15**, 127 (1996).

[8] D.M. Adams, and A.C. Shaw, *J. Phys. D: Appl. Phys.* **15**, 1609 (1982).

[9] D.M. Adams, A.G. Christy, and A.J. Norman, *Meas. Sci. Tech.* **4**, 422 (1993).

[10] A. Jayaraman, *Rev. Mod. Phys.* **55**, 65 (1983).

[11] K. Syassen, *High Press. Res.* **28**, 75 (2008).

[12] R.A. Forman, G.J. Piermarini, J.D. Barnett, and S. Block, *Science* **176**, 284 (1972).

[13] G J. Piermarini, S. Block, J.D. Barnett, and R.A. Forman, *J. Appl. Phys.* **46**, 2774 (1975).

[14] H.K. Mao, P.M. Bell, J.W. Shaner, and D.J. Steinberg, *J. Appl. Phys.* **49**, 3276 (1978).

[15] H.K. Mao, J.A. Xu, and P.M. Bell, *J. Geophys. Res. B* **91**, 4673 (1986).

[16] W.B. Holzapfel, *High Press. Res.* **25**, 87 (2005).

[17] P.F. Bernath, *Spectra of Atoms and Molecules*, 2nd ed. (Oxford University Press, New York, 2005).

[18] N.W. Ashcroft and N.D. Mermin, *Solid State Physics* (Thomson Learning, Inc., New York, 1976).

[19] J.I. Langford and D. Louër, *Rep. Prog. Phys.* **59**, 131 (1996).

[20] B.L. Henke, E.M. Gullikson, and J.C. Davis, *Atomic Data and Nuclear Data Tables* **54**, 181 (1993).

[21] M. Eriksson, *J. Synch. Rad.* **4**, 111 (1997).

[22] C. Kunz, *J. Phys.: Cond. Mat.* **13**, 7499 (2001).

[23] V. Honkimäki, J. Sleight, and P. Suortti, *J. Appl. Crys.* **23**, 412 (1990).

[24] Canadian Light Source (2009). *What is a synchrotron anyway?* Retrieved June, 2010 from http://www.lightsource.ca/education/whatis.php

[25] R.D. Deslattes, E.G. Kessler Jr., P. Indelicato, L. de Billy, E. Lindroth, and J. Anton, *Rev. Mod. Phys.* **75**, 35-99 (2003).

[26] J.S. Smith and S. Desgreniers, *J. Synch. Rad.* **16**, 83 (2009).

[27] A.P. Hammersley, S.O. Svensson, M. Hanfland, A.N. Fitch, and D. Häusermann, *High Press. Res.* **14**, 235 (1996).

[28] S. Desgreniers and K. Lagarec, J. Appl. Crys. **27**, 432 (1994); **31**, 109 (1998).

[29] R. Shirley, *The* CRYSFIRE *System for Automatic Powder Indexing: User's Manual* (The Lattice Press, Surrey, England, 2002).

[30] P.M. de Wolff, *J. Appl. Crys.* **1**, 108 (1968).

[31] J. Laugier and B. Bochu, *LMGP-Suite Suite of Programs for the interpretation of X-ray Experiments*, http://www.inpg.fr/LMGP

[32] A. Le Bail, H. Duray, and J.L. Fourquet, *Mater. Res. Bull.* **23**, 447 (1988).

[33] H. M. Rietveld, *Acta Cryst.* **21**, A228 (1966).

[34] J. Rodriguez-Carvajal, Physica B **192**, 55 (1993).

[35] R.A. Young, *The Rietveld Method (IUCr Monographs on Crystallography)* (Oxford University Press, Oxford, 1995).

Chapter 4

Cyanuric Triazide

The first compound studied in the present work is the molecular azide 2,4,6-triazido-1,3,5-triazine, commonly known as cyanuric triazide (CTA). This section will outline the preparation and stability of the CTA sample, followed by a presentation and discussion of the results of high pressure vibrational Raman spectroscopy and powder x-ray diffraction experiments.

4.1 Sample Preparation

4.1.1 Chemical synthesis

The small-scale chemical synthesis of cyanuric triazide was performed[†] by preparing a solution of 46 mg (0.25 mmol) cyanuric chloride ($C_3N_3Cl_3$) in 30 mL of acetone. To this solution, 52 mg (0.8 mmol) of sodium azide (NaN_3) was added. The mixture was then refluxed for 30 minutes and subsequently slowly cooled back down to ambient temperature. The resulting products were filtered to remove the sodium chloride (NaCl), leaving the cyanuric triazide (C_3N_{12})

[†] The chemical synthesis was performed by Didier Savard, graduate student (Department of Chemistry, University of Ottawa).

dissolved in the acetone mother liquor. This synthesis was carried out to a 48 mg (96%) yield.

Note: cyanuric triazide is very shock-sensitive and should be handled with the appropriate care.

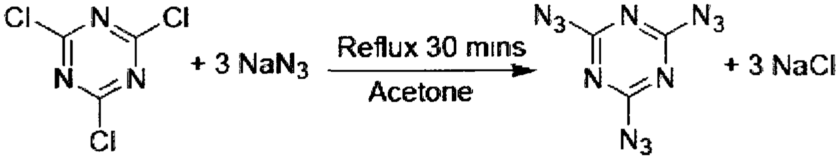

Figure 4.1: Reaction scheme for the synthesis of cyanuric triazide.

4.1.2 Sample preparation and loading into the diamond anvil cell

Using a Pasteur pipette, a small droplet of the cyanuric triazide dissolved in acetone was placed on a glass slide. The mother liquor was allowed to dissolve, leaving a residue on the slide. This residue was found to contain a mixture of polycrystalline aggregates, very small single crystals, and longer fibrous (needle) crystals, as shown in Figure 4.2 below.

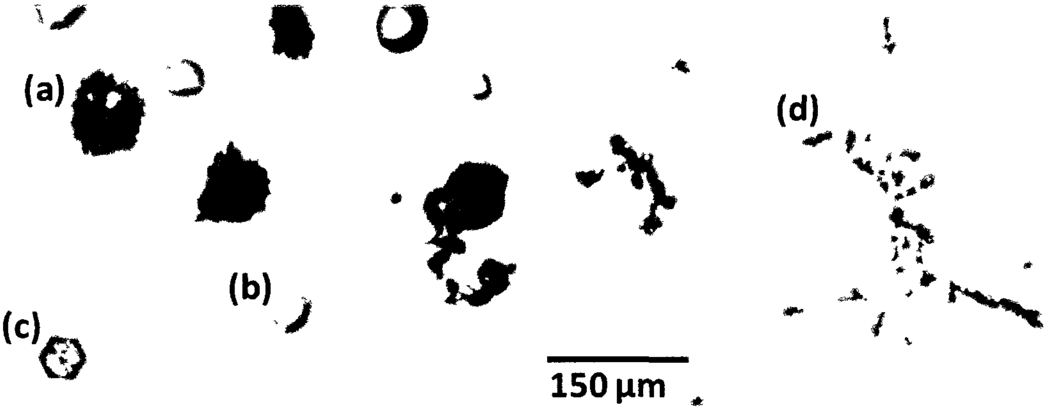

Figure 4.2: Two photomicrograph of cyanuric triazide residue on a glass slide after evaporation of acetone showing a mixture (a) polycrystalline aggregates, (b) droplets of solvated product, (c) small single crystals, and (d) fibrous needle crystals.

The polycrystalline aggregates were dislodged from the glass slide, broken up into small, thin flakes, and collected together to form a powder. In this form, cyanuric triazide was found to be significantly less shock-sensitive. While it should still be handled with the utmost care, the minute quantity of powder used in this work fortunately never detonated during tests to establish its sensitivity. Once in powder form, the sample was carefully loaded into a prepared gasket hole mounted on the diamond anvil cell. Care was taken to ensure that the material was well-packed and completely filled the sample chamber in order to maintain a sufficiently large sample volume upon the application of pressure.

4.2 Sample Stability

4.2.1 Laser-induced reaction

Cyanuric triazide, and related high nitrogen content energetic materials, are very sensitive and reactive compounds. Since Raman scattering is intrinsically weak, to collect data with the highest signal-to-noise ratio possible, the excitation laser should be running at a high power for a long exposure time. However, even with moderate laser powers (> 10 mW at the sample) or intermediate exposure times, the cyanuric triazide underwent photo-induced reactions, showing distinct laser "burn spots" (see Figure 4.3a). With even higher powers, or lower powers incident on the sample for prolonged periods (> 1 hr), the laser burned a "hole" right through the sample (see Figure 4.3b). However, since a void cannot be created in a sample under pressure, this is not actually a "hole" through the sample, but rather an area of laser-induced decomposition. Since the reacted area is transparent, it is likely that it contains pure nitrogen (N_2). Using reduced laser power (approximately 5 mW measured at the sample) and short exposure times (typically 2 minutes, though not more than 5 minutes) ensured the damage to the sample material was minimal, such that no discernable reaction occurred.

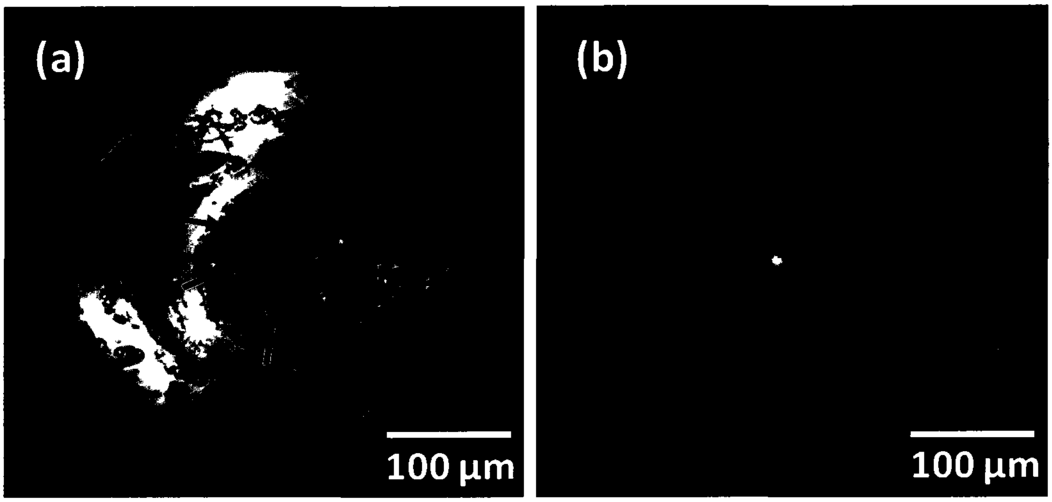

Figure 4.3: Samples of cyanuric triazide photographed in the high pressure diamond anvil cell showing (a) three areas of laser-induced reaction (seen as red spots, marked by the black arrows), and (b) an area of complete laser-induced decomposition due to prolonged laser exposure (approximately 1.5 hours at 5 mW).

4.2.2 Decomposition upon the application of pressure

Upon increasing pressure, there were some instances (approximately half the samples loaded) where the cyanuric triazide would completely decompose. This process occurred at pressures ranging from 8 to 12 GPa, was seemingly instantaneous, and was very easy to detect. There would be a sudden change in sample colour and opacity; before decomposition the sample would appear yellow-orange in transmission, while afterwards it would be black and completely opaque (see Figure 4.4). This was also accompanied by a significant change in Raman signal, from the expected Raman modes of cyanuric triazide to a much weaker broad doublet (see Figure 4.5).

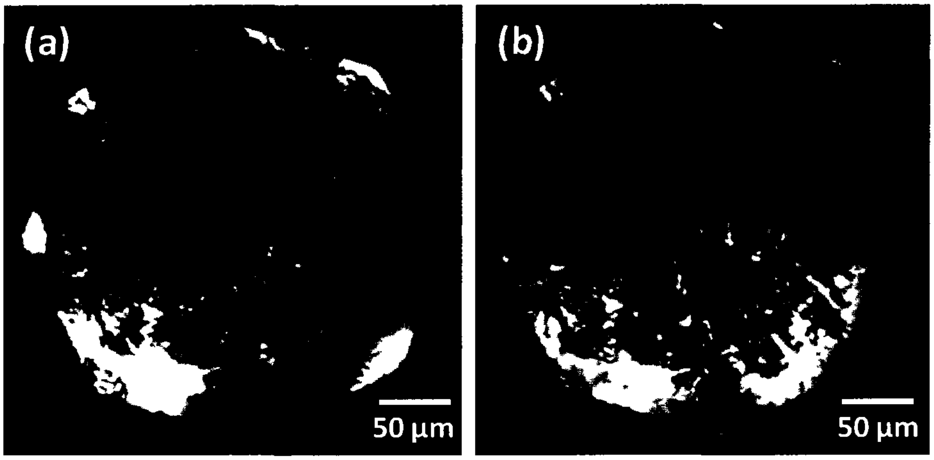

Figure 4.4: A sample of cyanuric triazide photographed in the diamond anvil cell (a) at 6.4 GPa and (b) after decomposition upon increasing the pressure to approximately 8 GPa.

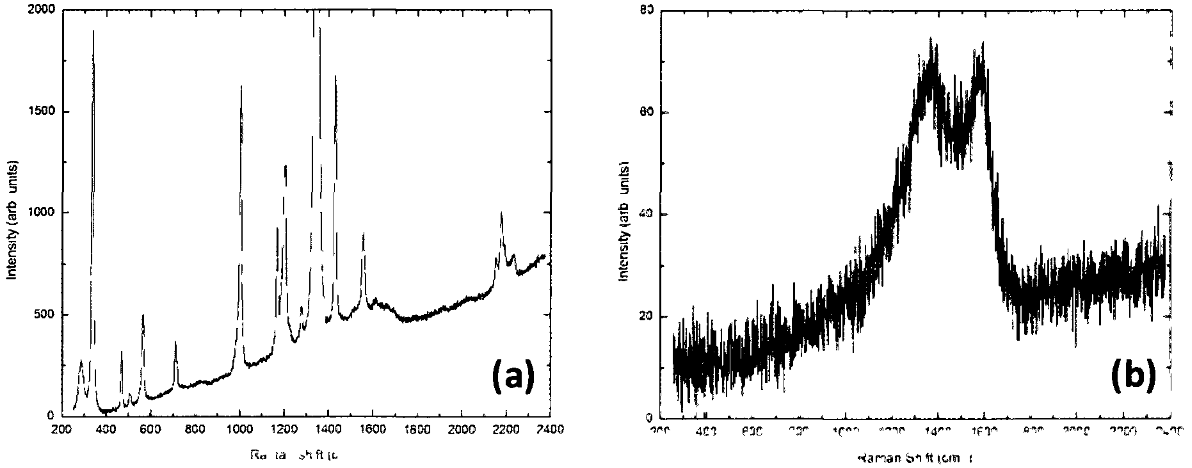

Figure 4.5: Raman spectrum of cyanuric triazide (a) before decomposition at 6.4 GPa and (b) after decomposition at ambient conditions (not in the DAC).

In some instances of decomposition, it was also accompanied by a sudden drop in pressure, where the process of decomposition likely caused the gasket to rupture, and other times it was accompanied by an audible *'crack'*.

To determine the composition of the reaction product, the Raman spectrum (Figure 4.5b) gave a first clue. The weak, broad doublet with peaks at 1370 cm^{-1} and 1580 cm^{-1} shows a striking resemblance to the characteristic disordered D and graphitic G bands of several types of carbon, including graphite, diamond-like carbon films, glassy carbon, and amorphous carbon [1]. In fact, there have been recent studies in the literature of chemical synthesis by the intentional detonation of cyanuric triazide [2 - 4]. There were a variety of different reaction products reported in these experiments including, cyanogen (C_2N_2), amorphous and graphitic carbon nanoparticles, and multi-walled carbon nanotubes [2, 3], as well as nitrogen-rich carbon nitrides (C_3N_x x=4,5) [4].

As a further investigation into its composition, images of the decomposition product in the gasket hole were taken using the JEOS JSM-7500F scanning electron microscope (SEM) located at the Electron Microscopy Facility at the Center for Catalysis Research and Innovation at the University of Ottawa. For an overall view of the material, low magnification images were taken and one example is shown in Figure 4.6. For a more detailed view of the structure, high magnification images were taken with one example being shown in Figure 4.7.

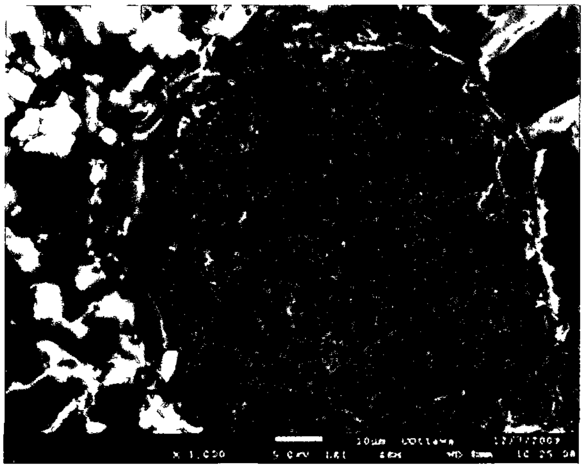

Figure 4.6: SEM image taken at 1000X magnification of the decomposition product inside the compression chamber showing the overall structure and surface features.

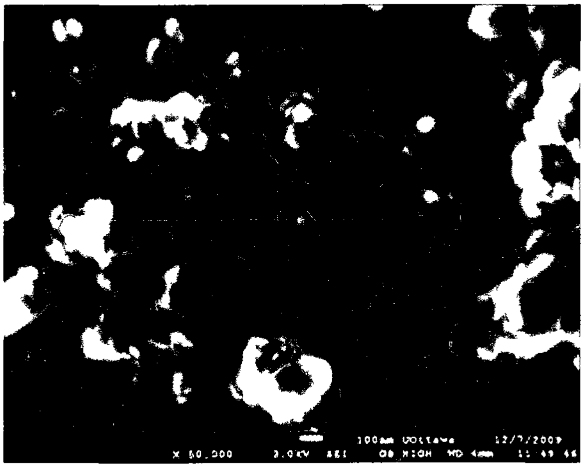

Figure 4.7: SEM image taken at 50,000X magnification of the decomposition product showing its fine structure characterized by nano-scale agglomerates

While SEM images provide an interesting and informative look at the appearance of the decomposition product, they cannot be used to determine the product composition. To this end, energy dispersive x-ray spectroscopy (EDS) microanalysis was performed using the same electron microscope. This technique gave a qualitative picture of the elemental composition. The results of the analysis are presented in Figure 4.8.

The EDS data collected from the gasket surface (Spectrum 1 in Figure 4.8) shows a large percentage of rhenium, as expected, but it also contains a notable amount of carbon, nitrogen and oxygen. Carbon and nitrogen are both common contaminants in these types of experiments; however, the significant amount of carbon and nitrogen observed on the gasket surface cannot be solely the result of contamination. It is most likely attributable to cyanuric triazide residue left on the gasket from the loading process.

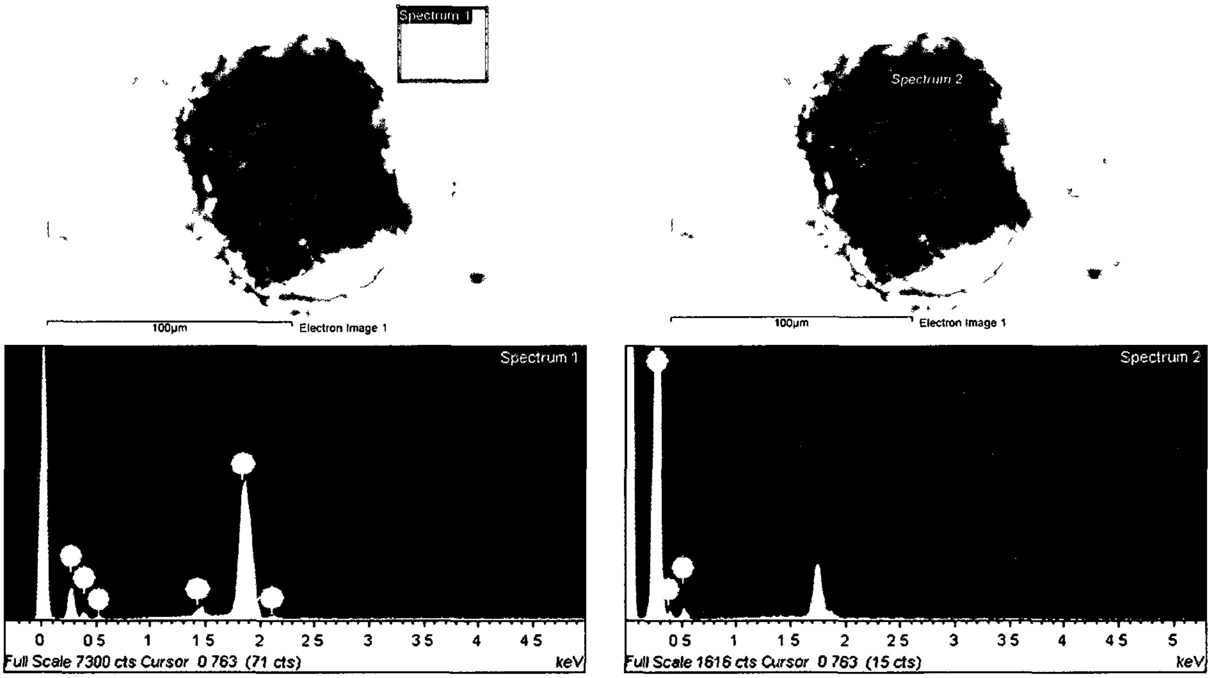

Figure 4.8: Acquired EDS data from the surface of the gasket (Spectrum 1) and the decomposition product (Spectrum 2). The spectra were acquired, calibrated, and plotted using INCAEnergy software (Oxford Instruments).

The data collected from the decomposition product (Spectrum 2 in Figure 4.8) shows a much different elemental composition. Rhenium is still present, though not labelled, but in a much smaller percentage, which may indicate that small rhenium particles became dislodged from the chamber edge. Compared to the cyanuric triazide residue on the gasket, the decomposition product shows a much greater ratio of carbon to nitrogen, suggesting that upon reaction molecular N_2 was produced, leaving behind a mostly-carbon containing product.

Combining the EDS results with the Raman data and the SEM images, it is likely that the cyanuric triazide decomposed primarily into a mixture of carbon nanoparticle and nanotube agglomerates as was seen by Kroke *et al.* [2] and Utschig *et al.* [3]. It is interesting to note that the formation of these reported carbon nanostructures was achieved only in the presence of transition metals (Fe, Ni, Cu, Ti). This may suggest that some small residual particles of rhenium, also a transition metal, from the spark drilling process became dislodged (as suggested by the EDS results) into the sample and catalyzed the decomposition. However, it is still unclear what initiates this reaction, especially since it always occurs within a relatively small pressure window, and why it occurs in some instances but not others.

4.3 Raman Spectroscopy Results

The vibrational Raman and infrared spectra of cyanuric triazide were first characterized at ambient conditions by Shearer *et al.* in 1968 [5]. The molecular symmetry separates the 39 degrees of freedom into 26 characteristic vibrational modes given by the irreducible representation:

$$\Gamma = 9A' + 9E' + 4A'' + 4E'' \tag{4.1}$$

where the modes of A' and E'' symmetries are Raman active, A'' is IR active, and E' is both Raman and IR active. The assignment of these modes is given in Table 4.1 along with approximate descriptions of the associated molecular motions.

It can be seen in Table 4.1 that there are 8 vibrational modes that are associated with the azide (N_3^-) group: the ν_4 and ν_{13} symmetric stretches, the ν_1 and ν_{10} asymmetric stretches, and the ν_7, ν_{16}, ν_{20}, and ν_{24} bends. Following these modes as a function of pressure will be of particular importance in identifying possible pressure-induced phase transformations to either a closed-ring structure (tritetrazole) or an extended nitrogen network (C_3N_{12} solid). The results of such experiments are presented in the following subsections.

Table 4.1: Vibrational mode assignments and descriptions of cyanuric triazide [5]

***A*' (Raman active)**	***E*' (IR, Raman active)**
ν_1 N_3 asymmetric stretch	ν_{10} N_3 asymmetric stretch
ν_2 Ring stretch	ν_{11} Ring deformation
ν_3 >–N stretch[†]	ν_{12} Ring deformation
ν_4 N_3 symmetric stretch	ν_{13} N_3 symmetric stretch
ν_5 Ring deformation	ν_{14} >–N stretch[†]
ν_6 Ring twist	ν_{15} Ring deformation
ν_7 N_3 bend	ν_{16} N_3 bend
ν_8 Ring breathing	ν_{17} >–N bend[†]
ν_9 CN_3 bend	ν_{18} CN_3 bend

***A*" (IR active)**	***E*" (Raman active)**
ν_{19} Ring deformation	ν_{23} Ring deformation
ν_{20} N_3 bend	ν_{24} N_3 bend
ν_{21} N_3 wag	ν_{25} N_3 wag
ν_{22} N_3 twist	ν_{26} N_3 twist

[†] > represents a carbon apex of the triazine ring

4.3.1 Ambient pressure Raman spectrum

When loading the cyanuric triazide sample into the diamond anvil cell, the anvils were brought together just enough to close the cell but not to apply any pressure to the sample. This allowed for the acquisition of the ambient pressure Raman spectrum to verify the composition and purity of the compound. Such a spectrum for CTA is shown in Figure 4.9, and comparing it to the literature spectrum (Figure 4.9, inset), it is clear that the sample is indeed pure.

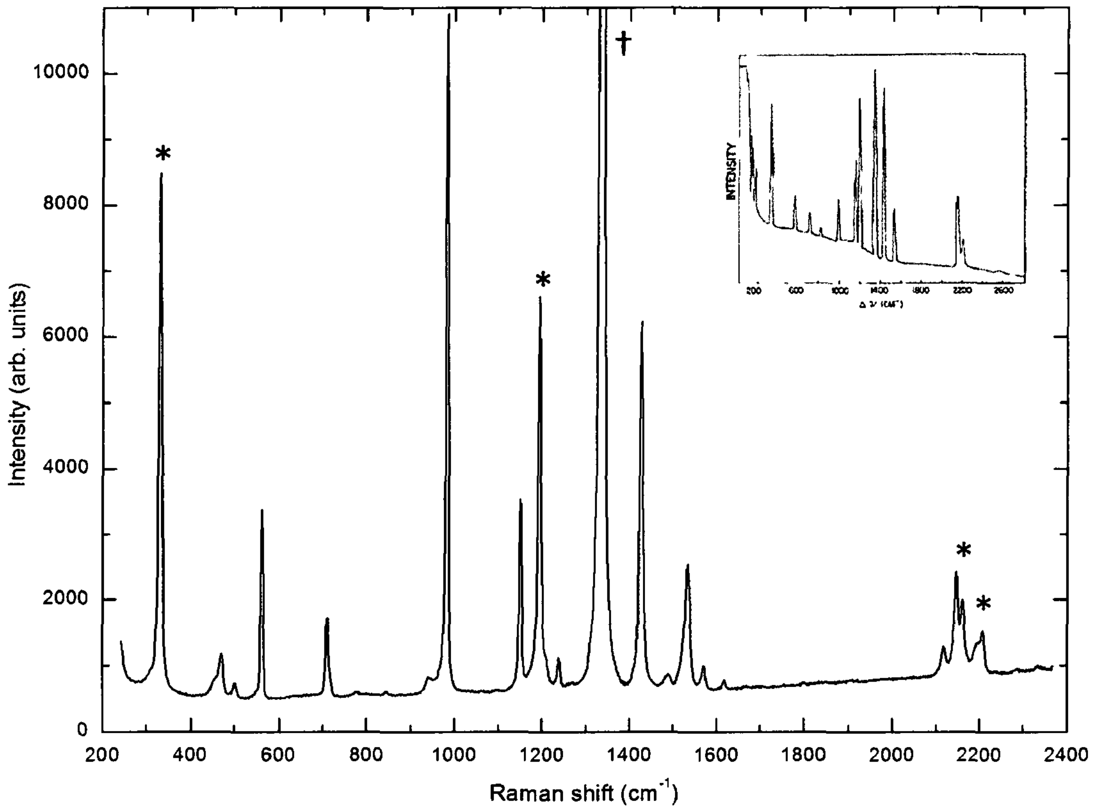

Figure 4.9: Raman spectrum of cyanuric triazide loaded in the diamond anvil cell at ambient pressure. The peak marked with the dagger (†) is the Raman band arising from diamond, while the peaks marked with asterisks (*) are due to vibrational modes associated with the N_3^- group. Inset: Raman spectrum reprinted from ref. [5] shown for comparison.

By comparison with the literature spectrum, the observed Raman peaks in the current work can be assigned to their originating vibrational modes, and are tabulated in Table 4.2. It is apparent that not all the observed peaks have a vibrational assignment, and conversely, some expected vibrational modes have no associated observed peaks. Many of these unassigned lines appear as weak shoulders to larger known modes. The presence of unassigned peaks is common in other symmetrical triazines and has been attributed to crystal-field and/or solvent effects [6, 7]. However, it is more likely that some of these weak bands could be assigned as one of the many allowed combination or overtone bands [5].

Table 4.2: Assignment of Raman bands of cyanuric triazide at ambient conditions

Raman shift (cm^{-1})	**Vibrational assignment and description**
331 (s)	ν_{25} (E'') N_3 wag
455 (sh)	
471 (w)	
501 (w)	
562 (m)	ν_8 (A') Ring breathing
710 (m)	ν_6 (A') Ring twist
717 (sh)	
941 (w)	
983 (s)	ν_{14} (E') >–N stretch
1151 (m)	ν_5 (A') Ring deformation
1194 (s)	ν_{13} (E') N_3 symmetric stretch
1210 (w)	ν_4 (A') N_3 symmetric stretch
1239 (w)	ν_3 (A') >–N stretch
1427 (s)	ν_2 (A') Ring stretch
1489 (w)	
1534 (m)	$\nu_8 + \nu_{14}$ (E') Ring breathing + >–N stretch
1572 (w)	
1619 (w)	
2118 (w)	$\nu_5 + \nu_{14}$ (E') Ring deformation + >–N stretch
2146 (m)	ν_1 (A') N_3 asymmetric stretch
2161 (m)	ν_{10} (E') N_3 asymmetric stretch
2196 (w)	$\nu_4 + \nu_{14}$ (E') N_3 symmetric stretch + >–N stretch
2208 (w)	$\nu_4 + \nu_{14}$ (E') N_3 symmetric stretch + >–N stretch

s = strong, m = medium, w = weak, sh = shoulder

With the sample purity confirmed at ambient conditions, the pressure on the diamond anvil cell was increased and the Raman spectrum was incrementally monitored for any changes which might be indicative of a phase transition.

4.3.2 Low pressure Raman results

The observed evolution of the Raman spectrum at low pressures is shown in Figure 4.10.

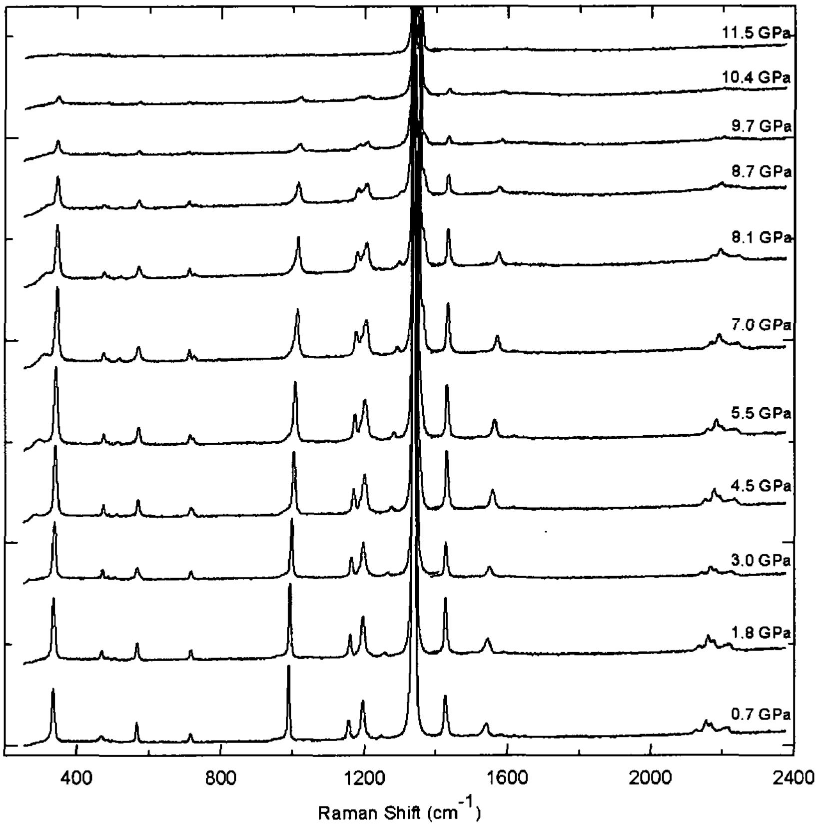

Figure 4.10: Evolution of Raman spectrum of cyanuric triazide at low pressures.

The most noticeable pressure effect seen in Figure 4.10 is the gradual decrease in intensity. The reasons for this decrease are twofold. Firstly, with increased pressure, the sample became thinner which reduced the scattering volume. The CTA sample also became increasingly opaque; in transmission the sample gradually changed from yellow, to orange, to red, and finally to black, as shown in Figure 4.11. With an increased opacity, the incident laser was absorbed, which also effectively reduced the scattering volume.

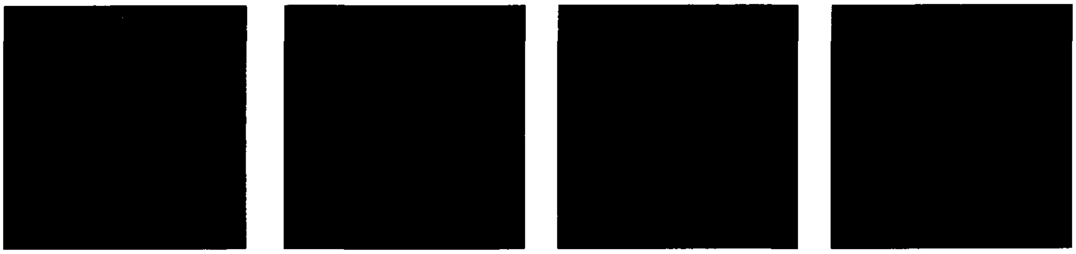

P = 1.8 GPa **P = 5.5 GPa** **P = 8.1 GPa** **P = 11.5 GPa**

Figure 4.11: Effect of pressure on the optical properties of cyanuric triazide. Photomicrographs of the sample seen in transmission show a reddening of the sample with increasing pressure (sample diameter ≈ 90 μm).

The Raman bands seen in Figure 4.10 also broaden with increased pressure due to non-hydrostatic and inhomogeneous pressure conditions. This smears out the peak intensity, giving the appearance of weaker peaks, even though the integrated intensities may remain the same.

A more subtle feature of the acquired low pressure Raman spectra is the evolution of the frequencies of the characteristic vibrational modes. Plotting these evolutions at low pressures shows very smooth relationships, as seen in Figure 4.12, indicative of the stability of the ambient structural phase to at least 30 GPa. A closer look at the effect of pressure on individual modes indicates that some modes are more affected than others. For example, the modes associated with the carbon-nitrogen bond between the triazine ring and the azide group increase by approximately 7 cm^{-1}/GPa, while pressure has very little effect on the ring distortions; the ring breathing modes increase by less than 1 cm^{-1}/GPa. Qualitatively this is logical, as pressure should have the most effect on the most accessible bonds. It is also observed that two modes, the ν_5 ring twist and the ν_6 ring deformation, each split into two modes. This is a solid state effect where the increased pressure, and resulting decreased intramolecular separations, breaks the symmetry associated with the isolated molecular model on which the vibrational mode assignment was made.

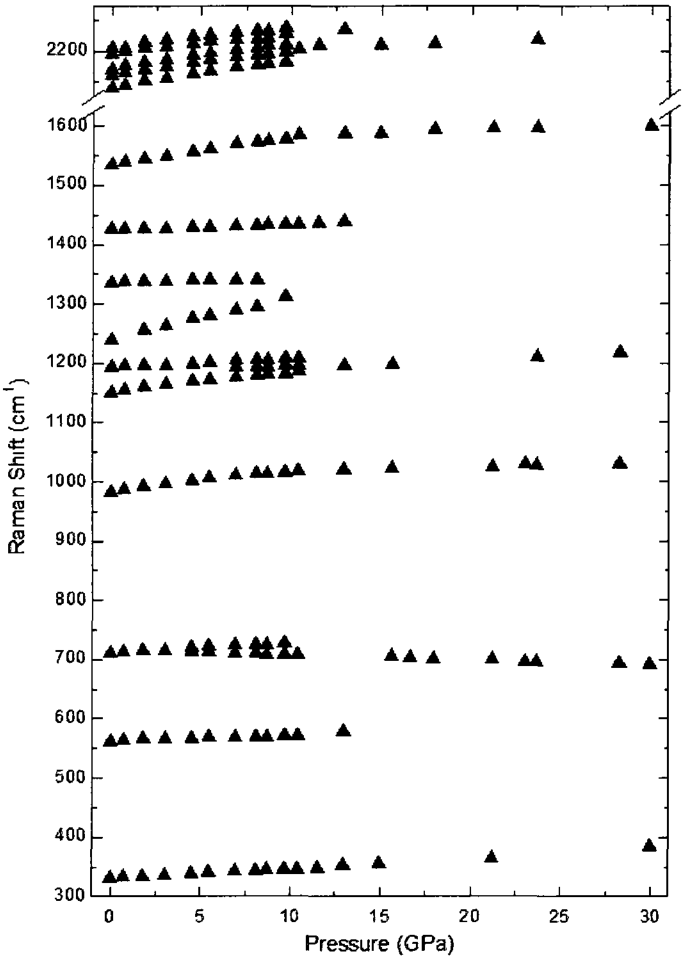

Figure 4.12: Evolution of the characteristic vibrational mode frequencies of cyanuric triazide with increasing pressure.

4.3.3 High pressure Raman results

Once the sample became opaque (little to no transmitted light), the Raman spectrum was rather sparse; the Raman bands were weak and broad, and were barely discernable from the background. This can be seen in Figure 4.10 and Figure 4.12, as many modes became too weak to follow. However, upon further application of pressure, despite no change in opacity, new modes appeared, as shown in Figure 4.13.

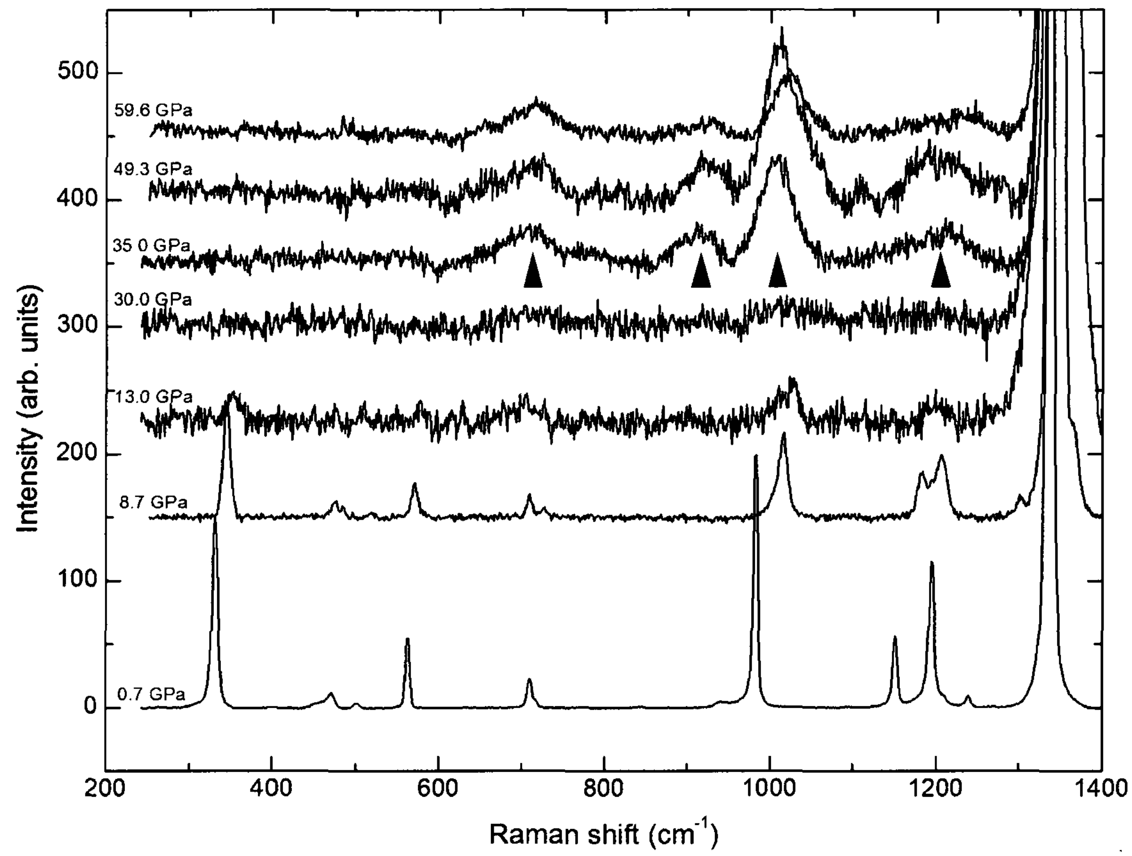

Figure 4.13: Representative evolution of Raman spectrum of cyanuric triazide at high pressures (measured pressures of the associated background-subtracted spectra are given in blue). By 13 GPa the sample is nearly completely opaque resulting in a very weak spectrum. Upon further increase of pressure, four new bands appear (marked by red triangles), suggesting a phase transition has occurred. Note that the intensity has been appropriately scaled in the bottom two traces and offsets have been added for clarity.

When the vibrational frequencies of these newly observed peaks are compared to those of the low pressure phase, there is a clear and drastic change that occurs between 30.0 and 32.6 GPa (see Figure 4.14). These new bands cannot be attributed to the low pressure phase, and thus some bonding pattern change has occurred, likely in the form of a structural phase transition.

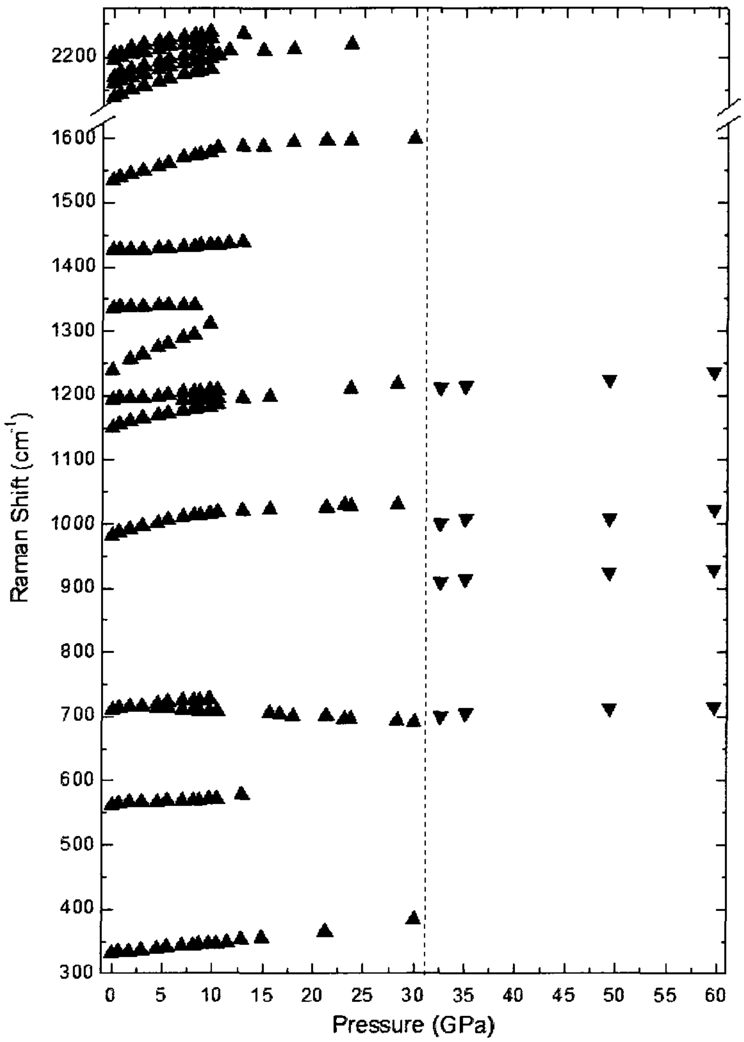

Figure 4.14: Pressure evolution of the vibrational mode frequencies of cyanuric triazide showing a distinct change indicative of a phase transition between 30 and 32.6 GPa.

While the Raman spectroscopic data alone cannot elucidate a structure, it may give an indication of the type of bonding present. As seen in Figure 4.13 and Figure 4.14, the high pressure phase of CTA features four Raman modes: two single modes at about 700 cm^{-1} and 1200 cm^{-1}, and a doublet centered near 1000 cm^{-1}. Intriguingly, this Raman spectrum is quite similar to that predicted for the single bonded cg-N phase of nitrogen (see Figure 2.3c). However, the doublet at 1000 cm^{-1} can also be explained by sp^3-hybridized carbon where the carbon of the triazine ring would form a fourth carbon-nitrogen bond with a neighbouring cyanuric triazide molecule [8], as would be seen for the predicted C_3N_{12} solid phase (see Section 2.4.1). It is clear that any structural determination will be the result of x-ray diffraction measurements.

4.4 Powder X-Ray Diffraction Results

The first report of the ambient pressure crystal structure of cyanuric triazide came in 1934 in the form of a letter written by Sir William Bragg [9] describing the conclusions of his student, Miss Ellie Knaggs. This short letter describes the molecular arrangement as "*a curious resemblance to the arms of the Isle of Man, a row of three nitrogen atoms lying in the position of each leg from knee to ankle*". This arrangement is shown in Figure 4.15.

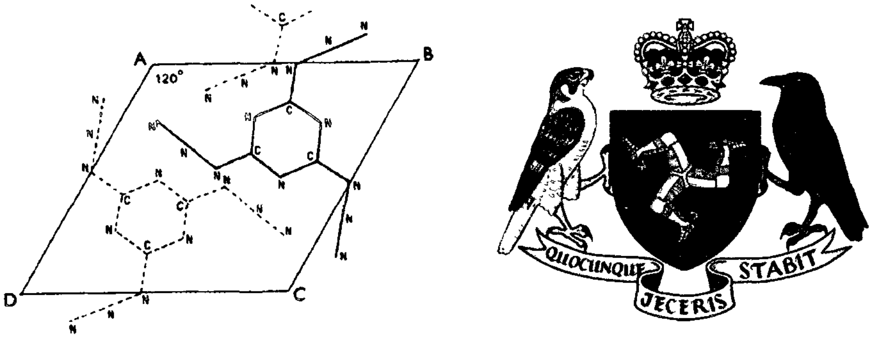

Figure 4.15: Left: Ambient pressure crystal structure of cyanuric triazide reported by Bragg (figure reprinted from ref. [9]). Right: Coat of arms of the Isle of Man [10].

The full report of the crystal structure was published in 1935 [11] and was determined using single crystal x-ray diffraction. Cyanuric triazide was found to be planar, have linear azide groups, and have hexagonal symmetry (belonging to the space group $P6_3/m$) with two molecules per unit cell. More recently, the crystal structure has been refined and improved using modern single-crystal diffraction experimental and analytical techniques [12], and is shown in Figure 4.16. The associated unit cell parameters are given in Table 4.3.

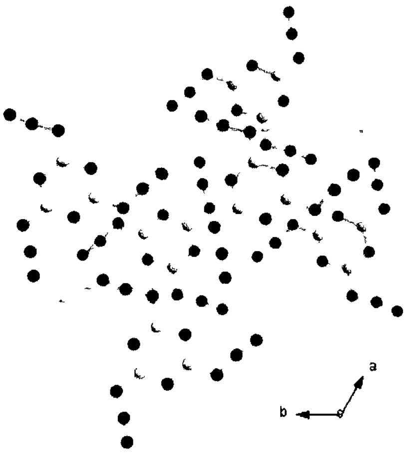

Figure 4.16: Ambient pressure crystal structure of cyanuric triazide determined by Keßenich *et al.* [12] where the blue and white molecules represent nitrogen and carbon, respectively.

Table 4.3: Unit cell parameters of cyanuric triazide at ambient pressure

a (Å)	c (Å)	c/a	V (Å^3)	ref.
8.73	5.96	0.68	393.4	[9]
8.7456(2)	5.8945(3)	0.674	390.44(3)	[12]

4.4.1 Ambient pressure diffraction results

Along with the ambient pressure Raman spectrum, comparing the experimental ambient pressure powder x-ray diffraction results with the above literature results will confirm the purity of the cyanuric triazide sample. A representative diffraction image collected of CTA at ambient pressure is given in Figure 4.17 where the Debye rings are indexed according to the literature crystal structure.

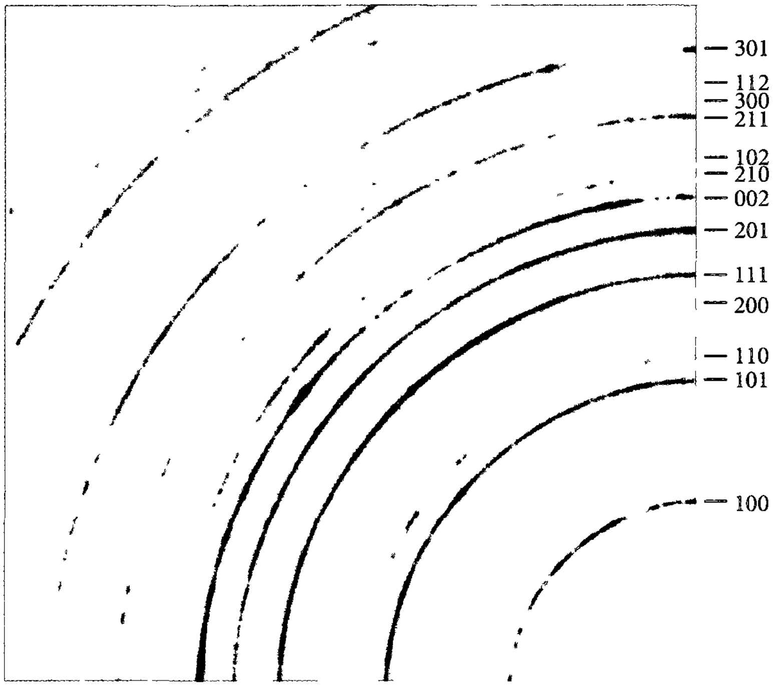

Figure 4.17: Small representative quadrant (equivalent to $0 < 2\theta < 13°$) of the diffraction image of cyanuric triazide at ambient pressure, showing the indexing of the observed Debye rings.

Once the image was integrated, the resulting diffraction pattern was fit using a full pattern Le Bail refinement (see Section 3.4.5). When comparing the observed diffraction peak (Bragg) positions to those associated with the known hexagonal space group of the ambient phase of CTA, it is seen in Figure 4.18 that all the observed peaks are accounted for, with no obvious extraneous peaks. The resulting extracted unit cell parameters given in Table 4.4 also agree with the literature single-crystal parameters given in Table 4.3.

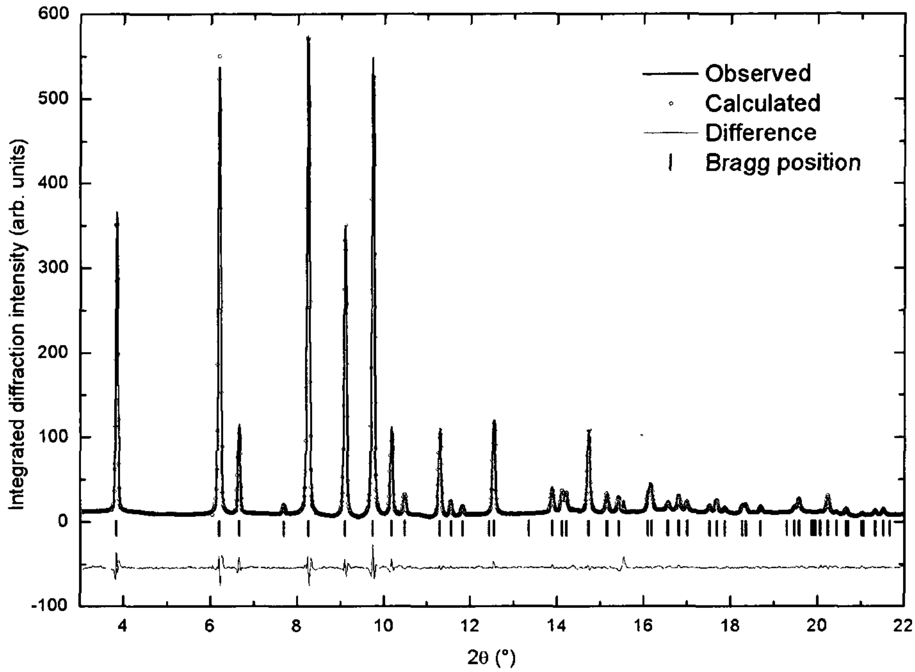

Figure 4.18: Results of Le Bail fit (red open circles) of x-ray diffraction data (black trace) of cyanuric triazide at ambient conditions confirming the crystalline structure and purity of the sample. The blue trace is the difference in intensity between the calculated Le Bail fit and the observed intensities. Diffraction pattern was recorded at the Canadian Light Source.

Table 4.4: Extracted experimental unit cell parameters and calculated volume from the Le Bail fit of cyanuric triazide at ambient pressure (two molecules per unit cell)

a (Å)	c (Å)	c/a	V (Å^3)	ref.
8.7695(5)	5.9928(4)	0.681	399.13(4)	This work

4.4.2 Diffraction results as a function of pressure

In order to corroborate the Raman results and confirm the occurrence of a phase transition between 30 and 32 GPa, high-resolution angle-dispersive powder x-ray diffraction experiments were performed on the CTA sample as a function of pressure. Five successful experiments were performed: one at low pressures (P < 18 GPa), three at high pressures (P < 60 GPa), and one decompression study (P starting at approximately 60 GPa, then decreased to ambient pressure). An overview of the results is best demonstrated by the high pressure studies (Figure 4.19), where diffraction images were acquired in intervals of approximately 3 - 4 GPa.

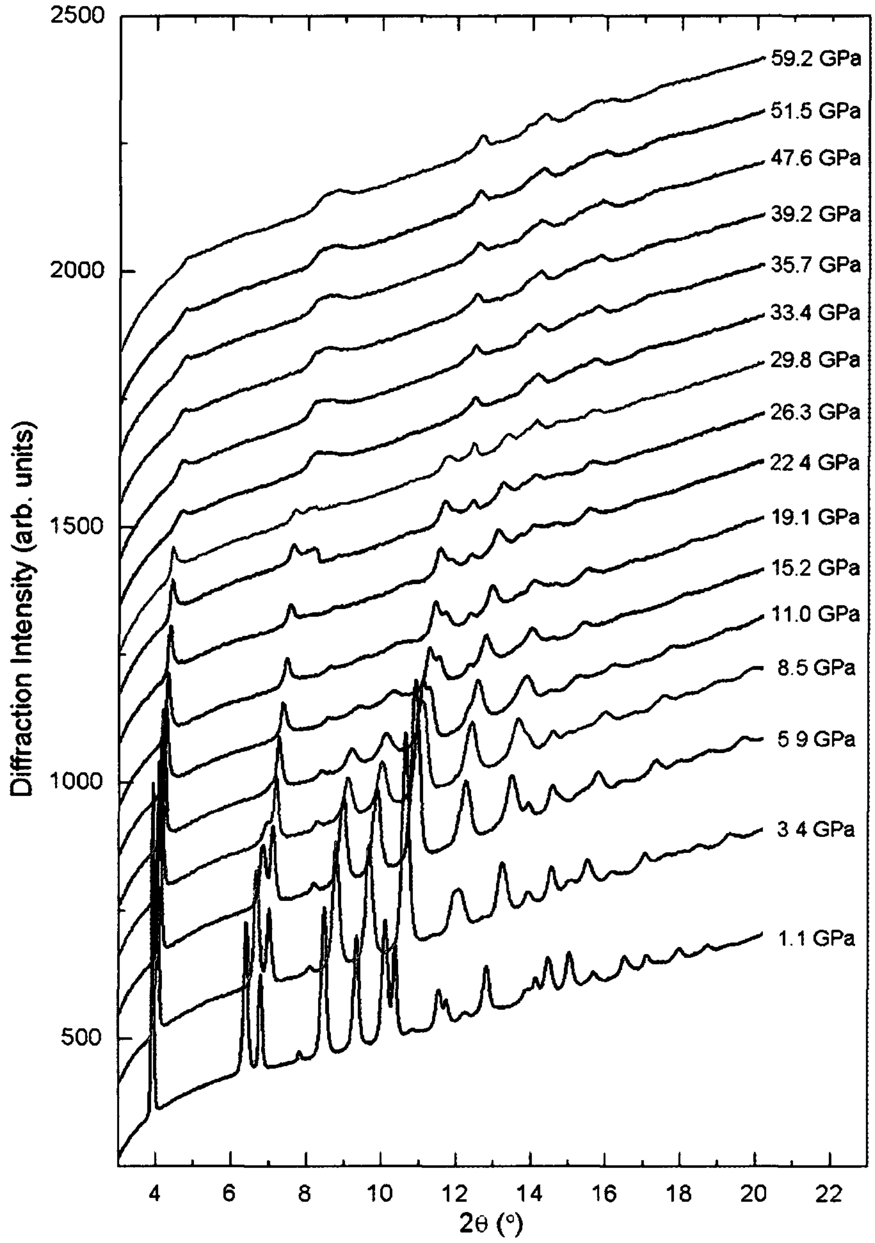

Figure 4.19: Evolution of the diffraction pattern of cyanuric triazide as a function of increasing external pressure showing a distinct pattern change between 29.8 and 33.4 GPa. Vertical offsets have been added for clarity.

The Raman results suggested that a phase transition occurred between 30 and 32.6 GPa, and indeed, examining the difference in the observed diffraction patterns between 29.8 and 33.4 GPa corroborates this conclusion. The difference is quite subtle, mostly due to peak broadening. However, it is clear that there are discontinuities in some peak positions that coincide with the noticeable disappearance of others. These differences are seen in the overview given in Figure 4.19, and are highlighted in Figure 4.20.

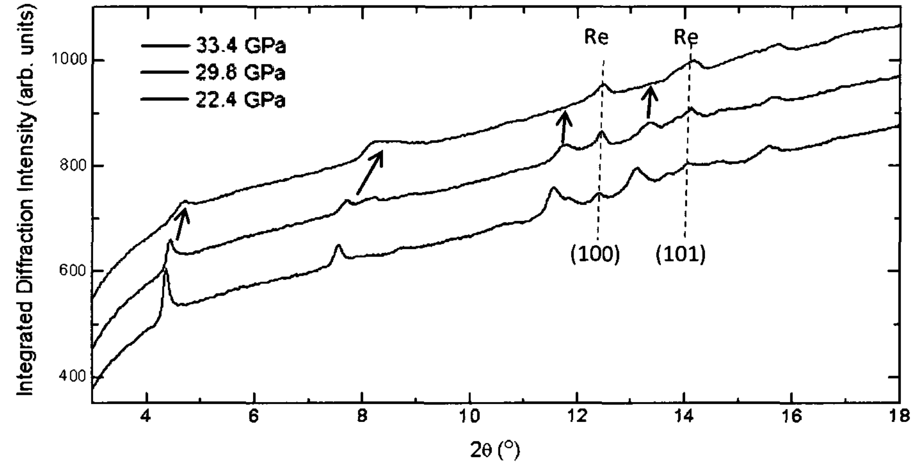

Figure 4.20: Selected region of the pressure evolution of the pXRD results highlighting the differences brought on by a phase transition between 29.8 and 33.4 GPa, including discontinuities (green arrows) and disappearance of peaks (red arrows). Diffraction peaks arising from the rhenium gasket are indexed and marked with the dashed lines.

Since these changes are subtle, the evolution of the observed *d*-spacings with increasing pressure was plotted to help confirm a phase transition. Such a plot is given below in Figure 4.21, which clearly identifies a phase transition. Further investigations of the low pressure and high pressure phases are presented in the following two subsections.

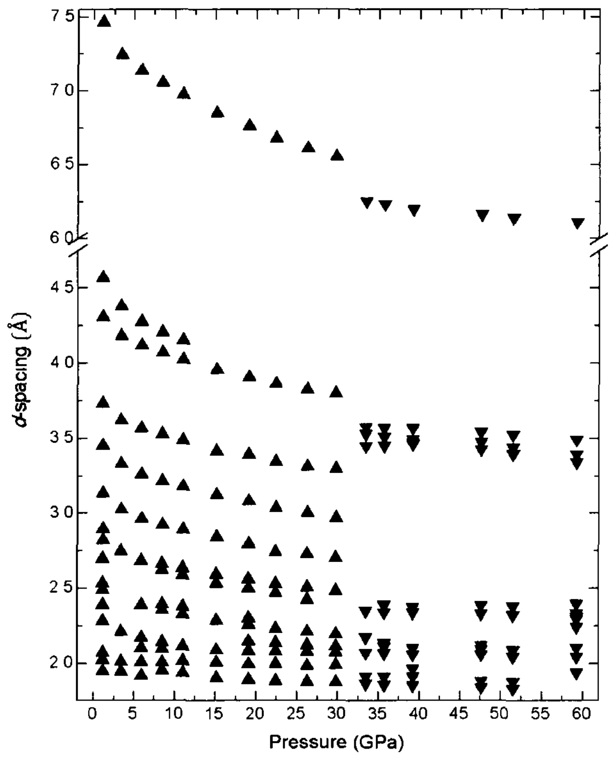

Figure 4.21: Evolution of observed *d*-spacings of cyanuric triazide with increasing pressure showing the occurrence of a structural phase transition between 29.8 and 33.4 GPa.

4.4.3 Low pressure phase

The ambient pressure structure is stable until approximately 30 GPa, and will be henceforth referred to as phase I. By examining how the hexagonal unit cell associated with this phase changes with pressure, properties of the material can be extracted. By modelling the observed change in unit cell volume with pressure using the third-order Birch-Murnaghan equation of state (see section 2.5.2), the bulk modulus and the pressure derivative of the bulk modulus were determined. These two parameters describe the stiffness of the material, and how that stiffness changes with applied pressure, respectively. The experimental fit is shown in Figure 4.22 and the resultant parameters are given in Table 4.5.

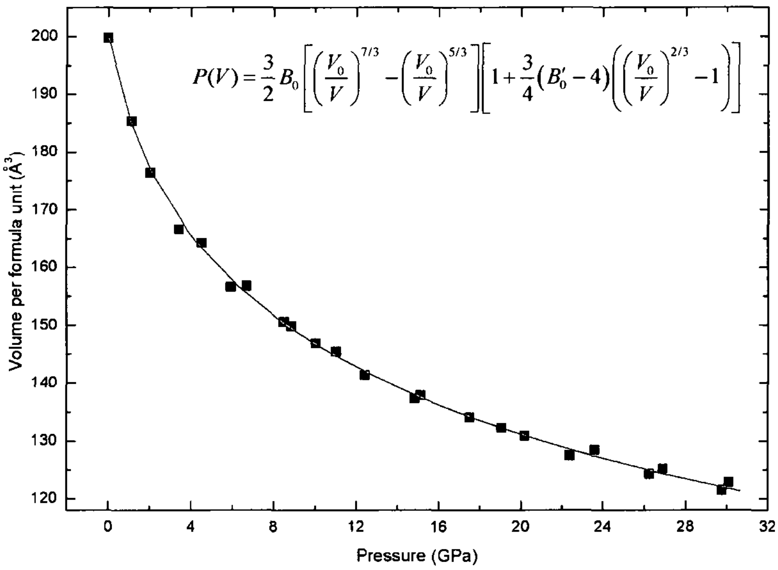

Figure 4.22: Modeling the unit cell volume of phase I of cyanuric triazide using the third-order Birch-Murnaghan equation of state (inset). The resulting best fit is given by the solid line with parameters given in Table 4.5.

Table 4.5: Parameters extracted from EOS fit of phase I of cyanuric triazide

Bulk modulus, B_0 (GPa)	**Pressure derivative of bulk modulus, B'_0**	**Initial volume per formula unit, V_0 (Å^3)**
10.5	7.9	199.84

Cyanuric triazide is shown to have a relatively small bulk modulus with a large pressure derivative, and therefore, is very compressible material that stiffens very rapidly with pressure. This is a common characteristic of energetic materials; a comparison of cyanuric triazide to other such materials is given in the discussion (Section 4.5.1).

4.4.4 High pressure phase

As is seen in Figure 4.19 and Figure 4.20, the new high pressure phase of cyanuric triazide observed above 33.4 GPa (henceforth referred to as phase II), is not an easy one to characterize. The observed diffraction peaks were sparse, weak, and very broad. There was also a significant contribution from the rhenium gasket surrounding the sample since, at high pressures, the rhenium thins out and its x-ray absorption correspondingly attenuates. For these reasons, the definite structure of phase II has not yet been determined. However, from the limited data collected, two possible unit cells are being proposed, one hexagonal and one orthorhombic.

The possibility of a hexagonal unit cell was first explored due to the similarity between the low-angle diffraction profiles of phases I and II. As it turned out, phase II showed good agreement with a hexagonal unit cell, as shown graphically in Figure 4.23 and quantitatively in Table 4.6. All of the phase II patterns were subsequently fit to this proposed cell, and the extracted unit cell parameters and volumes are given in Table 4.7.

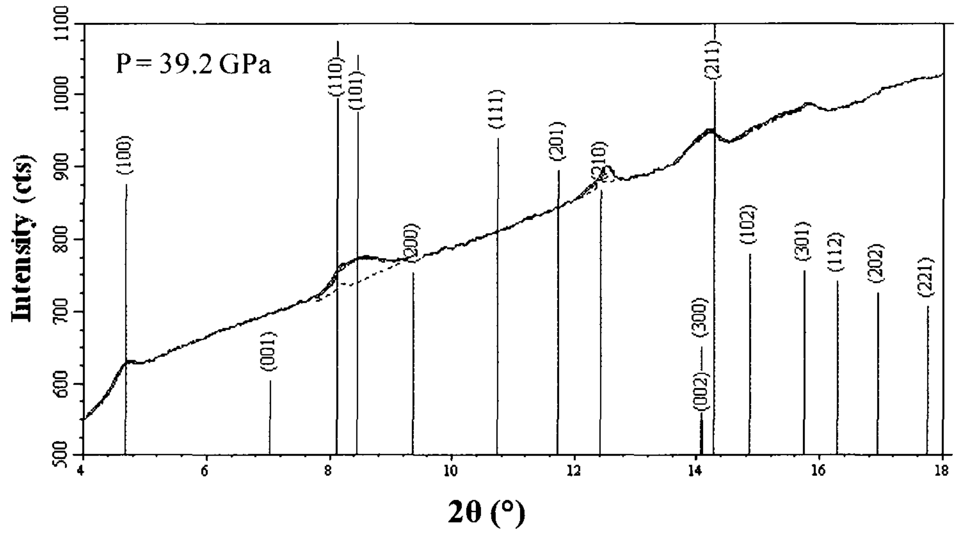

Figure 4.23: Example of results of a hexagonal unit cell fit to phase II of cyanuric triazide. Vertical bars represent the calculated *d*-spacings of the expected reflections of the fitted unit cell, and are a good match to the observed peaks.

Table 4.6: Results of a hexagonal unit cell fit of cyanuric triazide at 39.2 GPa

(*hkl*)	2θ observed (°)	*d*-spacing observed (Å)	*d*-spacing calculated (Å)	Difference d_{obs}-d_{calc} (Å)
100	4.702	6.2333	6.2593	-0.0260
110	8.190	3.5652	3.5581	0.0071
101	8.372	3.4876	3.4892	-0.0016
210	12.516	2.3355	2.3324	0.0031
300	14.221	2.0567	2.0509	0.0058
301	15.819	1.8501	1.8472	0.0029

Table 4.7: Extracted unit cell parameters for proposed hexagonal unit cell for phase II of CTA

Pressure (GPa)	a (Å)	c (Å)	Volume (Å^3)
33.4	7.174	4.282	191.03
35.7	7.155	4.252	188.54
39.2	7.145	4.220	186.69
47.6	7.103	4.203	183.95
51.5	7.073	4.153	180.92
59.2	7.042	4.081	175.31

The P,V data points for the hexagonal unit cell were used along with the data from phase I to examine the transitional volume collapse. The P,V curve assuming a hexagonal unit cell for phase II is given in Figure 4.24, and the volume change is calculated to be approximately 17%.

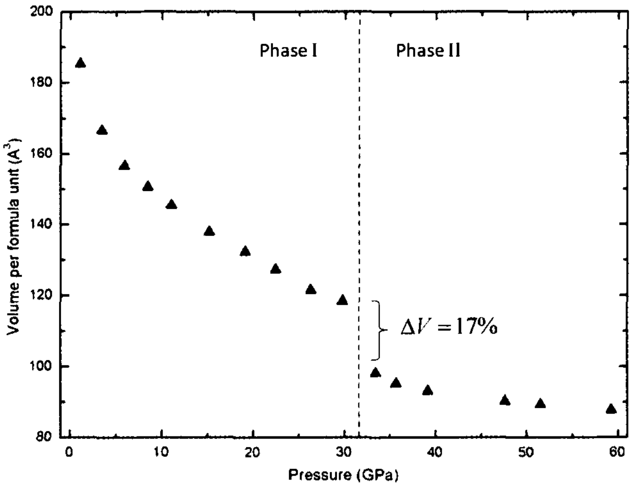

Figure 4.24: Experimental P,V curve for cyanuric triazide assuming a hexagonal unit cell for phase II. The transitional volume collapse is shown and calculated to be approximately 17%.

A completely analogous analysis was performed using the proposed orthorhombic unit cell. This unit cell also showed very good agreement with the observed diffraction patterns, as shown graphically in Figure 4.25 and quantitatively in Table 4.8. The phase II patterns were subsequently fit, and the extracted unit cell parameters and volumes are given in Table 4.9.

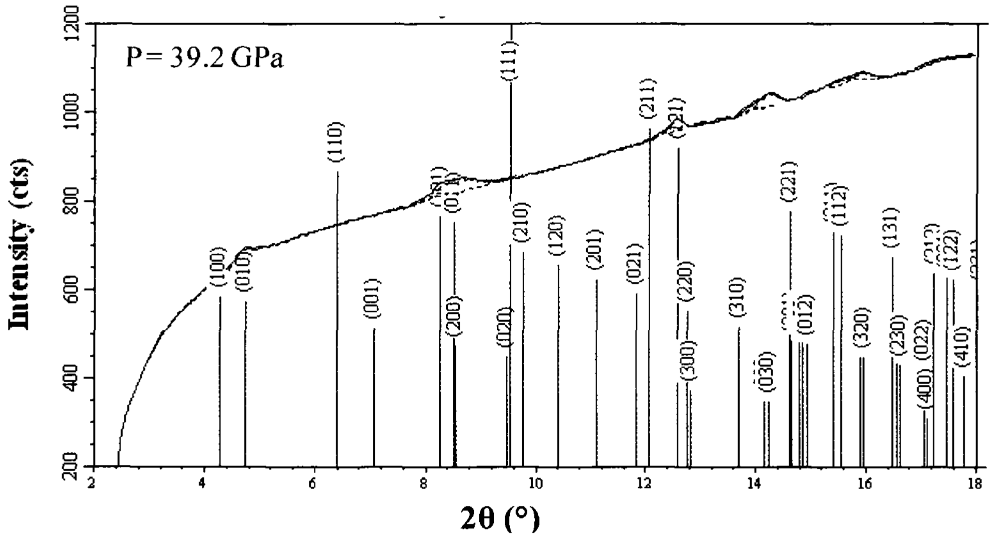

Figure 4.25: Example of results of an orthorhombic unit cell fit to phase II of cyanuric triazide. Vertical bars represent the calculated *d*-spacings of the expected reflections of the fitted unit cell, and are a good match to the observed peaks.

Table 4.8: Results of an orthorhombic unit cell fit of cyanuric triazide at 39.2 GPa

(*hkl*)	**2θ observed (°)**	***d*-spacing observed (Å)**	***d*-spacing calculated (Å)**	**Difference d_{obs}-d_{calc} (Å)**
010	4.702	6.2333	6.2017	0.0316
101	8.190	3.5652	3.5692	-0.0040
200	8.472	3.4876	3.4844	0.0032
121	12.516	2.3355	2.3208	0.0147
320	15.819	1.8500	1.8504	-0.0004
212	17.188	1.7037	1.6960	0.0077

Table 4.9: Extracted unit cell parameters for proposed orthorhombic unit cell for phase II of cyanuric triazide

Pressure (GPa)	**a (Å)**	**b (Å)**	**c (Å)**	**Volume (Å^3)**
33.4	7.103	6.262	4.133	183.84
35.7	6.922	6.241	4.161	179.73
39.2	6.884	6.247	4.158	178.81
47.6	6.844	6.170	4.136	174.65
51.5	6.796	6.148	4.113	171.93
59.2	6.702	6.128	4.092	168.07

Like for the previously considered hexagonal unit cell, the P,V data points for the proposed orthorhombic unit cell were used along with the data from phase I to examine the transitional volume collapse. The P,V curve assuming a orthorhombic unit cell for phase II is given in Figure 4.26, and the volume change is calculated to be approximately 21%.

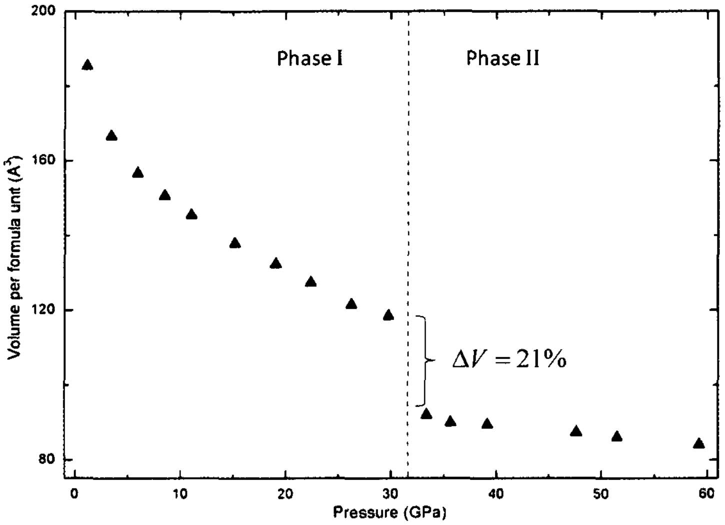

Figure 4.26: Experimental P,V curve for cyanuric triazide assuming an orthorhombic unit cell for phase II. The transitional volume collapse is shown and calculated to be about 21%.

Both unit cells provide reasonable explanations of the observed x-ray diffraction patterns for phase II of CTA. However, due to the non-hydrostatic pressure conditions, the extreme line broadening, and intrinsically weak intensities, a definite structural solution of phase II was not possible. Further experiments and computational studies are needed, and will be discussed in more detail in Chapter 6 (Summary and Future Work).

4.4.5 Decompression studies

Even without a definite structural solution, the retention of phase II to ambient conditions would be a strong indication of the formation of either the closed-ring tritetrazole structure or the single-bonded C_3N_{12} solid. Furthermore, the recovery of a material containing a single-bonded nitrogen network would be of significant experimental value.

The pressure on a sample of cyanuric triazide was increased to approximately 55 GPa to allow for a study of the behaviour of phase II upon decompression. The pressure was reduced incrementally, and the recorded diffraction patterns are shown in Figure 4.27.

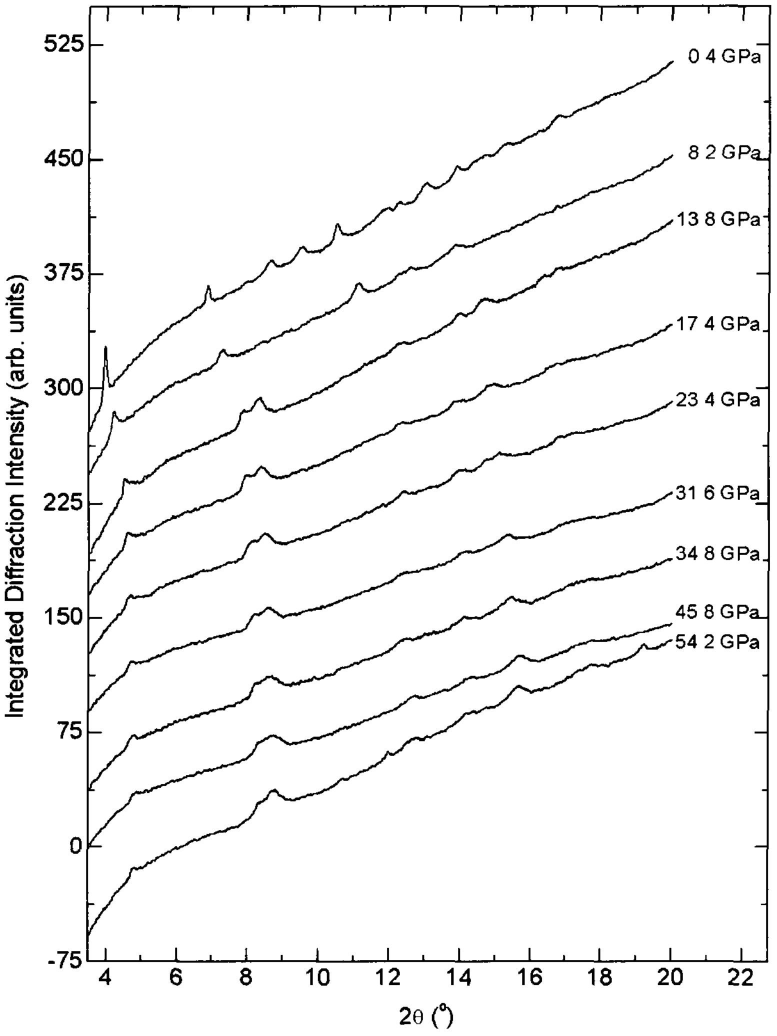

Figure 4.27: Powder x-ray diffraction patterns of cyanuric triazide upon decreasing pressure. Experiment started at 54.2 GPa (bottom trace) and ended at 0.4 GPa (top trace). It is clearly seen that there is a transformation from phase II back to phase I between 13.8 and 8.2 GPa. Patterns belonging to phase II are in black, while patterns belonging to phase I are in blue.

Phase II was retained over a large pressure range, that is, it exhibits a very large hysteresis. However, the transition was found to be reversible; between 13.8 and 8.2 GPa, the high pressure phase II transformed back to the low pressure phase I.

4.5 Discussion

4.5.1 Phase I

Both the vibrational Raman spectroscopy and powder x-ray diffraction experiments indicated that cyanuric triazide undergoes a first order structural phase transition between 30 and 32 GPa. As pressure is increased, phase I (ambient to 30 GPa) gradually changed from pale yellow to deep red, and eventually black. This change in optical properties is attributed to a narrowing of the material's band gap, and resulted in a weakening of the Raman spectra.

The pressure, volume (P,V) data collected for phase I was fit to a third-order Birch-Murnaghan equation of state (EOS). The parameters extracted from this fit gave a bulk modulus of 10.5 GPa, and a pressure derivative of the bulk modulus of 7.9, indicating that CTA is a very compressible material (small B_0) but stiffens rapidly upon increasing pressure (large B'_0). These types of values are commonly seen for energetic materials. The comparison of the equation of state parameters for a selection of common energetic materials to the parameters of CTA obtained in this work is given in Table 4.10.

It is important to note that the development of the Birch-Murnaghan equation of state assumes hydrostatic pressure conditions, and thus RDX and HMX were both studied using argon as a pressure-transmitting medium and were correctly modeled using the third-order Birch-Murnaghan EOS. The ambient structural phase of another common energetic material, CL-20, is only stable up to 0.7 GPa, and with such a small pressure range, the pressure derivative of the bulk modulus could not be properly determined and was thus given a fixed value of 4 (equivalent to using a second-order Birch-Murnaghan EOS).

Table 4.10: Properties of selected energetic materials in comparison to cyanuric triazide

Material	Bulk modulus, B_0 (GPa)	Pressure derivative of bulk modulus, B'_0	Reference
RDX (in Ar)	13.9	5.8	[13]
HMX (in Ar)	12.4	10.4	[14]
CL-20	18.9	$4^{\dagger}$	[15]
LiN_3	19.1	7.3	[16]
CTA	10.5	7.9	this work

† Fixed value

Qualitatively, CTA is very similar to other common energetic materials. However, since the high pressure CTA experiments were performed without a pressure-transmitting medium, the extracted parameters of a third-order Birch-Murnaghan EOS are not the most accurate representation of the material properties. Nevertheless, the parameters do provide a good approximation, which can be qualitatively used in a meaningful way.

4.5.2 Phase II

While both the vibrational Raman spectroscopy and powder x-ray diffraction experiments clearly identified the occurrence of a phase transition between 30 and 32 GPa, the extreme line broadening observed in both Raman spectroscopy and x-ray diffraction results, brought on by non-hydrostatic pressure conditions, has precluded any definite characterization of phase II. Even determining possible unit cells that describe the observed diffraction patterns was a challenge. There are very few peaks, and those which can be discerned from the background are very broad. However, this is to be expected. Without a hydrostatic pressure-transmitting medium such as argon or helium, at high pressures the sample experiences highly anisotropic stress that not only causes broadening, but can also induce preferred orientation in the powder that can result in the intensities of certain reflections being severely suppressed. Moreover, at these high pressures the sample becomes much thinner (especially since CTA is highly compressible), which reduces the available scattering volume and consequently the observed diffraction intensities. This presented a significant difficulty in determining the appropriate peak positions which are used in the fitting routine. Furthermore, due to the low number of observable peaks, even a small shift of one peak position would result in considerably different unit cell parameters. After careful fitting, two unit cells emerged as possible solutions, one hexagonal and one orthorhombic.

As was shown in Section 4.4.4, both possible unit cells provided a good fit to the observed x-ray diffraction data; neither unit cell failed to explain any observed peaks, but expectantly, both had several predicted peaks that were not observed. In this respect, the hexagonal unit cell has noticeably fewer unobserved reflections than the orthorhombic cell. However, with the difficulties addressed previously, this certainly does not exclude the orthorhombic unit cell, but perhaps slightly favours the hexagonal unit cell.

Both proposed unit cells also both represented significant transitional volume collapses: 17% and 21% for the hexagonal and orthorhombic unit cells, respectively. These types of large volume drops are not uncommon when major chemical bonding changes occur. For comparison, the transition from molecular nitrogen to cubic gauche single-bonded nitrogen is accompanied by a 21% volume collapse. Again, there is no unambiguous experimental evidence for the preference of one unit cell over the other; further investigations (both experimental and theoretical) are clearly required.

The decompression studies showed a promisingly large hysteresis for phase II, but transformation back to phase I was observed below 13 GPa. It was computationally predicted that the sought-after C_3N_{12} solid structure would be metastable and recoverable at ambient conditions (see Section 2.4.1). Thus, the reversible nature of the observed phase transition then perhaps indicates that phase II is *not* the anticipated carbon nitride structure. However, since there is no definitive indication one way or the other from the high pressure Raman and powder XRD studies, any concrete conclusions would be unsubstantiated and highly speculative.

References

[1] J.L. Lauer. Raman Spectra of Quasi-Elemental Carbon. In I.A. Lewis and G.M. Edwards (Eds.) *Handbook of Raman Spectroscopy* (Marcel Dekker Inc., New York, 2001).

[2] E. Kroke, M. Schwarz, V. Buschmann, G. Miehe, F. Fuess, R. Riedel, *Adv. Mater.* **11**, 158 (1999).

[3] T. Utschig, M. Schwarz, G. Miehe, E. Kroke, *Carbon* **42**, 823 (2004).

[4] E. Gillan, *Chem. Mater.* **12**, 3906 (2000).

[5] S.J. Shearer, G.C. Turrell, J.I. Bryant, and R.L. Brooks III, *J. Chem. Phys.* **48**, 1138 (1968).

[6] W.J. Jones and W. Orville Thomas, *Trans. Faraday Soc.* **55**, 203 (1959).

[7] W. Sawdony, K. Niedenzu, and J. Dawson, *J. Chem. Phys.* **45**, 3155 (1966).

[8] A. Hu, personal communication (May 26, 2010).

[9] W.H. Bragg, *Nature* **134**, 138 (1934).

[10] Isle of Man Government (2010). *Island Facts.* Retrieved July 2010, from http://www.gov.im/isleofman/facts.xml

[11] I.E. Knaggs, *Proc. Roy. Soc. London A* **150**, 576 (1935).

[12] E. Keßenich, T.M. Klapötke, J. Knizek, H. Nöth, and A. Schulz, *Euro. J. Inorg. Chem.* **1998**, 2013 (1998).

[13] C.S. Yoo, H. Cynn, W.M. Howard, and N. Holmes, *Proceedings of the Eleventh International Detonation Symposium*, Snomass, Colorado, 951 (2000).

[14] C.S. Yoo, and H. Cynn, *J. Chem. Phys.* **111**, 10229 (1999).

[15] J.C. Gump, and S.M. Peiris, *Proceedings of the Thirteenth International Detonation Symposium*, Norfolk, Virginia, 1045 (2007).

[16] S.A. Medvedev, I.A. Trojan, M.I. Eremets, T. Palasyuk, T.M. Klapötke, J. Evers, *J. Phys.: Condens. Matter* **21**, 195404 (2009).

Chapter 5

Ammonium Azide

The second compound studied in the present work is the ionic ammonium azide (AA). This section will outline the preparation and stability of the AA sample, followed by a presentation and discussion of the results of high pressure vibrational Raman spectroscopy and powder x-ray diffraction experiments.

5.1 Sample Preparation

5.1.1 Chemical synthesis

The small-scale chemical synthesis of ammonium azide was performed‡ according to a modified known synthetic pathway [1]. The pathway used in this work is shown in Figure 5.1. 5.0 g (0.075 mol) of sodium azide was added to 5 mL of distilled water. The solution was stirred until the sodium azide had completely dissolved (approximately 5 minutes), then 9 mL of a 30% solution of ammonium hydroxide in water (0.077 mol NH_4OH) was quickly added. This mixture was stirred for an additional 5 minutes while being cooled to 0 °C in an ice water bath.

---

‡ The chemical synthesis was performed by Didier Savard, graduate student (Department of Chemistry, University of Ottawa).

To remove the sodium ion from the final product, it was precipitated out as sodium bicarbonate ($NaHCO_3$) using solid CO_2 (dry ice). The dry ice was added in small amounts (2 - 3 g) in 5 minute intervals, for a total of approximately 50 g. The resulting precipitate was filtered using a cold filtration system, and the addition of dry ice was repeated twice more to ensure complete removal of the sodium ion. The product, ammonium azide (NH_4N_3) in a distilled water mother liquor, was then placed in a 2 - 8 °C refrigerator for slow evaporation, allowing long, clear needle crystals to form. The yield of this reaction could not be calculated due to the very rapid sublimation of the product when removed from the mother liquor.

$$\mathrm{NaN_3 + NH_4OH \xrightarrow{CO_2(s)} NH_4N_3 + NaHCO_3}$$

Figure 5.1: Reaction scheme for the synthesis of ammonium azide.

5.1.2 Sample preparation and loading into the diamond anvil cell

The sample of ammonium azide was prepared by removing a single crystal from the mother liquor. To remove any impurities, the crystal was washed by repeated dragging it through distilled water. The crystal was then crushed on a clean glass slide to create a fine powder, which could then be loaded into the sample chamber of the diamond anvil cell.

However, a small challenge was encountered during the loading process that required using a modified sample loading technique; ammonium azide sublimates into ammonia (NH_3) and hydrazoic acid (N_3H) at room temperature [2, 3]. The entire loading process was performed in a custom glove bag that was purged and subsequently filled with argon to provide an inert atmosphere. Furthermore, to avoid sublimation, both the glass slide containing the ammonium azide and the diamond anvil cell were placed on dry ice inside the glove bag during the sample loading process. As was the case for cyanuric triazide, care was taken to ensure that the material was well-packed and completely filled the sample chamber in order to maintain a sufficiently large sample volume upon the application of pressure. The excess ammonium azide on the glass slide was placed in a resealable plastic bag purged and filled with helium that was kept inside a freezer for later use.

5.2 Sample Stability

Except for sublimation into NH_3 and N_3H, ammonium azide is a stable salt, especially in polycrystalline form, and no shock decomposition was ever observed during handling. Contrary to cyanuric triazide, no photo-induced reaction with the incident laser during Raman studies was ever observed. This allowed for the use of higher laser powers, up to approximately 17 mW at the sample. Also unlike CTA, ammonium azide never decomposed upon increasing pressure.

This observed stability of ammonium azide compared to cyanuric triazide is not unexpected. The trend of increasing instability of azide compounds with increasing covalent character has been long known, as it was described in Linus Pauling's milestone textbook "*The Nature of the Chemical Bond*" [4]. Cyanuric triazide is classified as an organic covalent azide, while ammonium azide is an ionic azide (salt). While ammonium azide is thus more stable than cyanuric triazide, it is less stable than other alkali-metal azides such as sodium azide (NaN_3) due to the presence of N-H···N hydrogen bonds between the ammonium and azide ions.

5.3 Raman Spectroscopy Results

An infrared (IR) vibrational study of ammonium azide was first reported by Dows *et al.* [5] in 1955, which was shortly followed by a combined Raman and IR study by Gray and Waddington [2] in 1957, and was then further refined and expanded by Iqbal and Malhotra [6] in 1971. For a large part, the basics of the vibrational spectrum of ammonium azide can be understood by treating the NH_4^+ and N_3^- ions separately.

The tetrahedral ammonium NH_4^+ cation has four fundamental modes, two N-H stretches and two N-H bends, all of which are both Raman and IR active [7]. The linear triatomic azide N_3^- anion has three fundamental modes: a Raman active symmetric stretch, an IR active bend and an IR active asymmetric stretch [7]. In the solid state, the ammonium ion also processes a torsional oscillation (librational) mode along with translational lattice modes [5, 6] and the azide ion is also expected to have many lattice vibrations [6]. Furthermore, in the crystalline form of ammonium azide, formation of N-H···N hydrogen bonds breaks the symmetry of the azide ion, and thus causes a splitting of its vibrational modes. Therefore, by correlating the individual ion symmetries discussed above with the crystal site symmetries (a process known as factor group analysis), the vibrational mode assignments of crystalline ammonium azide can be made. These assignments are given with their associated molecular motions in Table 5.1.

Table 5.1: Vibrational mode assignments and descriptions of ammonium azide [6]

Modes associated with N_3^- anion		
ν_1^- (A_g)	N_3^- symmetric stretch	Raman active
ν_1^- (B_{1g})		
ν_2^- (A_u)	N_3^- bend	IR active
ν_2^- (B_{1u})		
ν_2^- (B_{2u})		
ν_2^- (B_{3u})		
ν_3^- (B_{2u})	N_3^- asymmetric stretch	
ν_3^- (B_{3u})		
Modes associated with NH_4^+ cation		
ν_1^+ (A)	N-H symmetric stretch	Raman, IR active
ν_2^+ (A)	N-H bend	
ν_3^+ (B)	N-H symmetric stretch	
ν_4^+ (B)	N-H bend	
ν_6^+	NH_4^+ libration	IR active

$^-$ and $^+$ superscripts are only used to distinguish vibrational modes associated with the anion and cation, respectively

5.3.1 Ambient pressure Raman spectrum

Before loading the ammonium azide sample into the diamond anvil cell, some polycrystalline powder was placed on a glass slide so that the ambient pressure Raman spectrum could be acquired without the interference from the Raman mode from diamond. The observed Raman spectrum was then compared to the literature spectrum to verify the purity and composition of the compound. Such a spectrum for the azide vibrational mode region of AA is shown in Figure 5.2, and comparing it to the literature spectrum (Figure 5.2, inset), it is clear that the prepared sample was pure, and ready to be loaded into the diamond anvil cell. Note that there is a systematic shift of about 5 cm^{-1} between the acquired and literature spectra. This is most likely a matter of calibration, but is difficult to establish as the experimental details of the published results do not include their precision or accuracy of measurements.

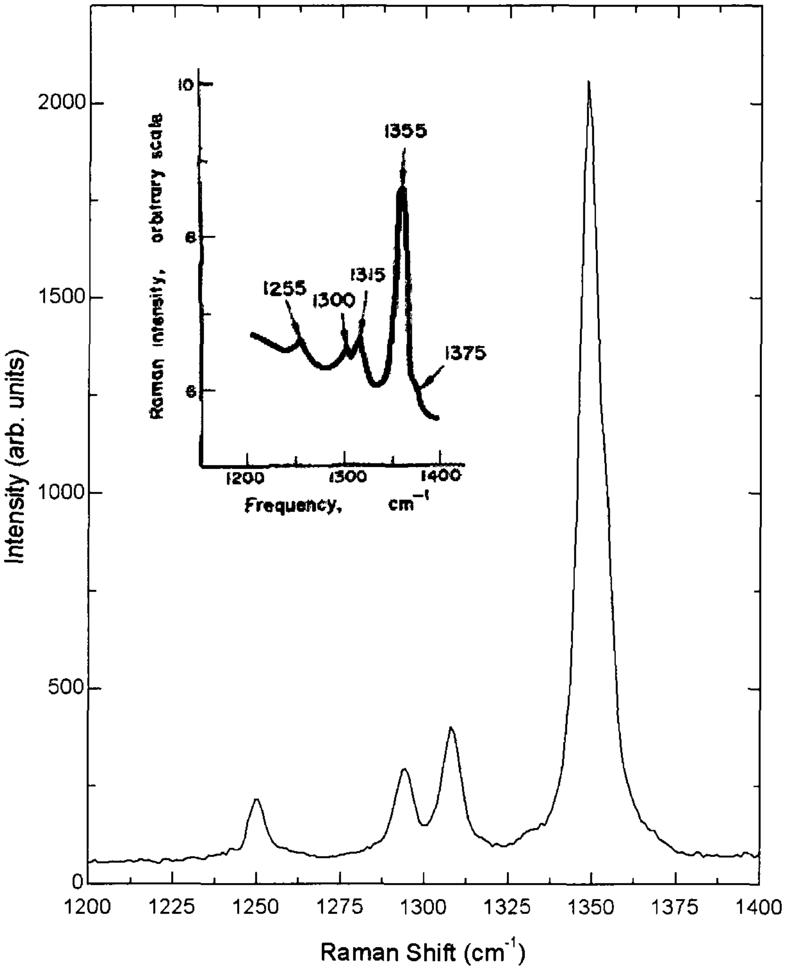

Figure 5.2: Azide (N_3^-) vibrational mode region of the Raman spectrum of ammonium azide at ambient pressure and temperature. Inset: Raman spectrum reprinted from ref. [6] shown for comparison.

By comparison with the literature spectrum, the observed Raman peaks were assigned to their originating vibrational modes, and are tabulated in Table 5.2.

Table 5.2: Assignment of Raman bands of ammonium azide at ambient conditions

Raman shift (cm^{-1})		**Vibrational assignment and description**	
1250	(m)	$2\nu_2^-$ (B_{1u})	Harmonic of N_3^- bend
1294	(m)	$2\nu_2^-$ (B_{2u})	Harmonic of N_3^- bend
1302	(m)	$2\nu_2^-$ (B_{3u})	Harmonic of N_3^- bend
1348	(s)	ν_1^- (A_{1g})	N_3^- symmetric stretch
1353	(sh)	ν_1^- (B_{1g})	N_3^- symmetric stretch
1420	(w)	ν_4^+ (B)	N-H bend
1670	(w)	ν_2^+ (A)	N-H bend
1823	(w)	ν_4^+ (B) + ν_6^+	N-H bend + NH_4^+ libration

s = strong, m = medium, w = weak, sh = shoulder

All of the observed peaks have been assigned to their known vibrational modes. And thus, with the sample purity confirmed, the ammonium azide powder was loaded into the diamond anvil cell in preparation for high pressure Raman spectroscopy experiments, where the pressure is increased while the Raman spectrum is incrementally monitored for any changes which might be indicative of a phase transition.

5.3.2 High pressure Raman results

Once the ammonium azide was loaded into the diamond anvil cell at low pressure and the Raman spectrum was acquired, it was clear that the first order Raman mode of diamond would significantly interfere with the observation of the AA Raman modes. The Raman mode of diamond is orders of magnitude more intense than the AA modes, and happens to have nearly the same frequency as the strongest ν_1^- mode of AA. A comparison of the Raman spectrum recorded at ambient conditions and at low pressure inside the DAC is given in Figure 5.3.

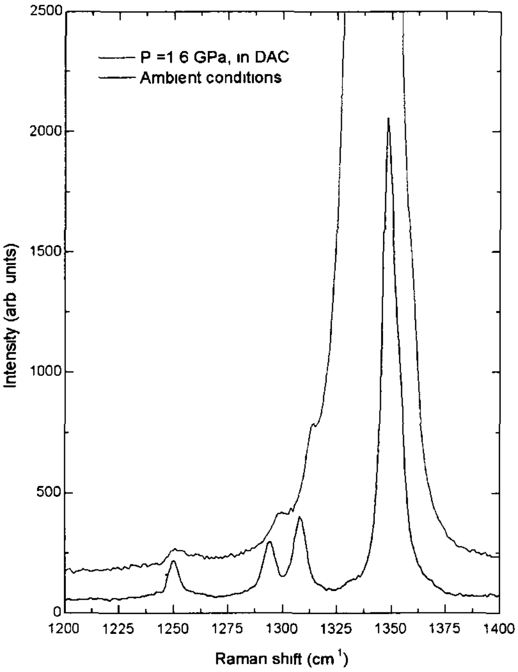

Figure 5.3: Effect of Raman band of diamond on the observed Raman spectrum of ammonium azide. The bottom trace is at ambient conditions while the top trace is taken in the diamond anvil cell at 1.6 GPa. The Raman band due to diamond is significantly more intense and obscures the ammonium azide Raman bands.

The evolution of the lattice modes (low frequency) and the azide modes of ammonium azide up to 65 GPa is shown in Figure 5.4. In this plot it can be seen that the ν_1^- mode of ammonium azide at low pressures is obscured by the Raman band of diamond. However, since pressure has a greater effect on the ν_1^- mode than it does on the diamond mode, at higher pressures (starting at approximately 3.5 GPa), the ν_1^- mode moves out from leading edge of the diamond mode and becomes easily identifiable. The $2\nu_2^-$ modes also shift to higher frequencies and consequently become indistinguishable from the diamond peak. Beginning at 12.6 GPa, the intensity of the ν_1^- (B_{1g}) mode begins to noticeably increase, while simultaneously the intensity of the ν_1^- (A_{1g}) mode decreases. Above 20.3 GPa, the ν_1^- (A_{1g}) mode is no longer observed. These properties are highlighted by plotting the mode evolutions as a function of pressure, as seen in Figure 5.5.

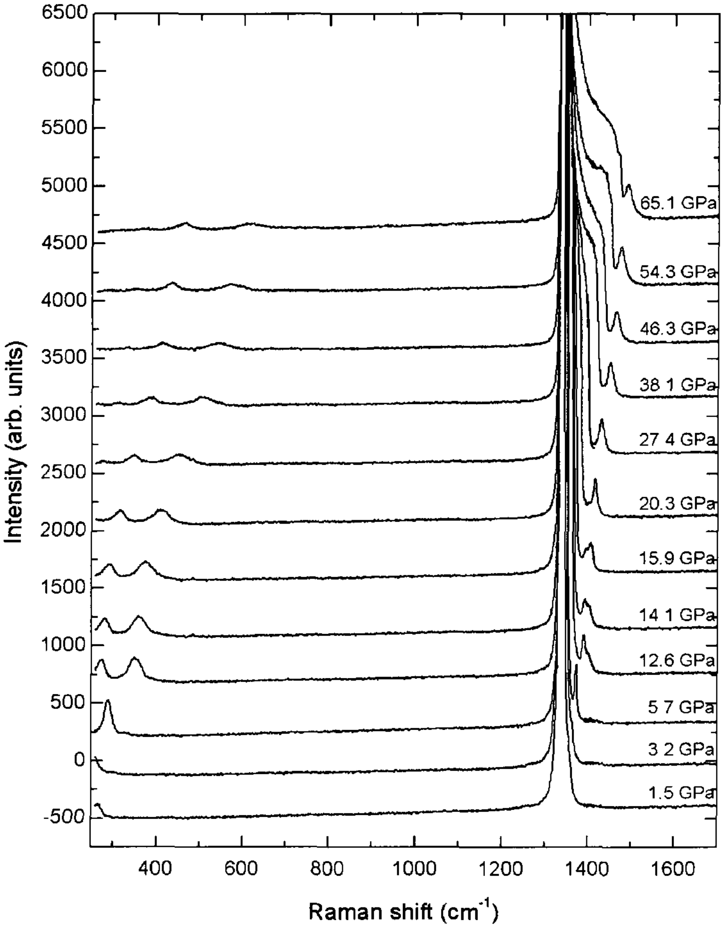

Figure 5.4: Representative evolution of the Raman spectrum of ammonium azide.

Despite the change in intensity between the two ν_1^- modes, the Raman modes vary smoothly with increased pressure. This suggests that no major bonding rearrangement of ammonium azide occurred up to the highest pressure studied (65.1 GPa).

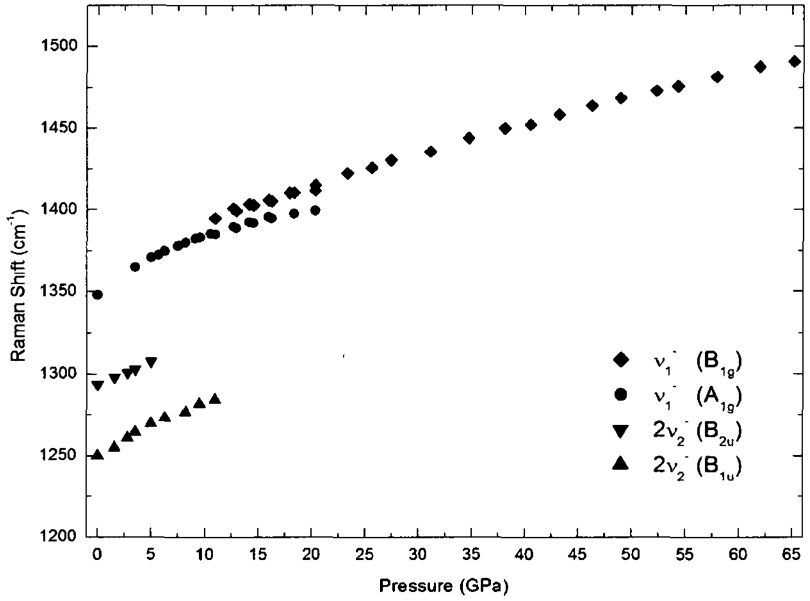

Figure 5.5: Evolution of the characteristic vibrational mode frequencies of the azide group within ammonium azide with increasing pressure

5.4 Powder X-Ray Diffraction Results

Like cyanuric triazide, the crystal structure of ammonium azide at ambient conditions has long been known. It was first reported by Frevel in 1936 [8] and was determined using single-crystal x-ray diffraction: Ammonium azide was found to have linear azide ion (N_3^-) chains that were hydrogen bonded to the ammonium cations through N-H···N bonds, and have orthorhombic symmetry (belonging to the space group *Pmna*) with four molecules (four NH_4^+ cations and four N_3^- anions) per unit cell. The crystal structure was further refined in 1978 by Prince and Choi using single-crystal neutron diffraction which allowed for more accurate measurement of the hydrogen atomic positions [9], and is shown in Figure 5.6. The associated unit cell parameters are given in Table 5.3.

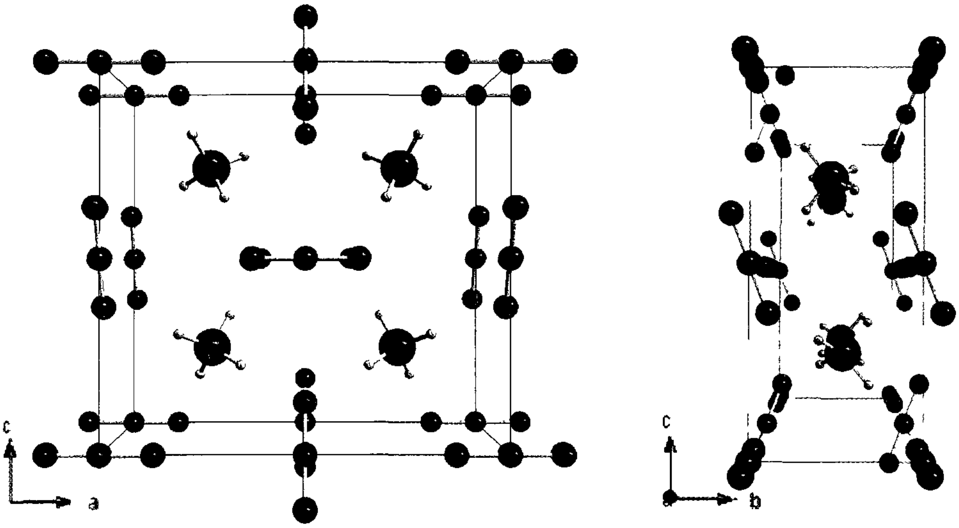

Figure 5.6: Ambient pressure crystal structure of ammonium azide determined by Prince and Choi [9] where the blue and white molecules represent nitrogen and hydrogen, respectively. Left: view looking down the **b** axis. Right: view looking along the **a** axis.

Table 5.3: Unit cell parameters and volume of ammonium azide at ambient pressure

a (Å)	b (Å)	c (Å)	V (Å^3)	ref.
8.930(3)	3.800(2)	8.642(3)	293.26	[8]
8.948(3)	3.802(2)	8.659(3)	295.05	[9]

As seen in Figure 5.6, there are two distinct types of azide groups, those which lie parallel to the **a** axis (type 1), and those which are tilted off the **c** axis and when looking down the **a** axis, appear to form a herringbone pattern (type 2). The bonding associated with both types of azide groups are similar; the N-N distance within the azide group is 1.168(4) Å and 1.171(4) Å, and the N-H···N (hydrogen bond) distance is 1.936(9) Å and 1.981(9) Å, for type 1 and type 2, respectively [9]. The tilt of the type 2 azide groups off of the **c** axis is measured at 20.9(2)°.

5.4.1 Near-ambient pressure diffraction results

Along with the ambient pressure Raman spectrum, comparing the experimental ambient pressure powder x-ray diffraction results with the literature results will confirm the purity of the ammonium azide sample. However, due to the rapid ambient condition sublimation of AA, a diffraction image could not be acquired at ambient pressure. The diamond anvil needed to be closed and a small amount of pressure needed to be exerted to ensure that the sample would remain intact. The lowest pressure studied was 0.7 GPa, and so while direct comparisons to the ambient pressure literature results cannot be made, it can still be used to confirm the sample composition. The room temperature x-ray diffraction image collected of ammonium azide at 0.7 GPa is given in Figure 5.7, where the Debye rings are indexed according to the literature crystal structure.

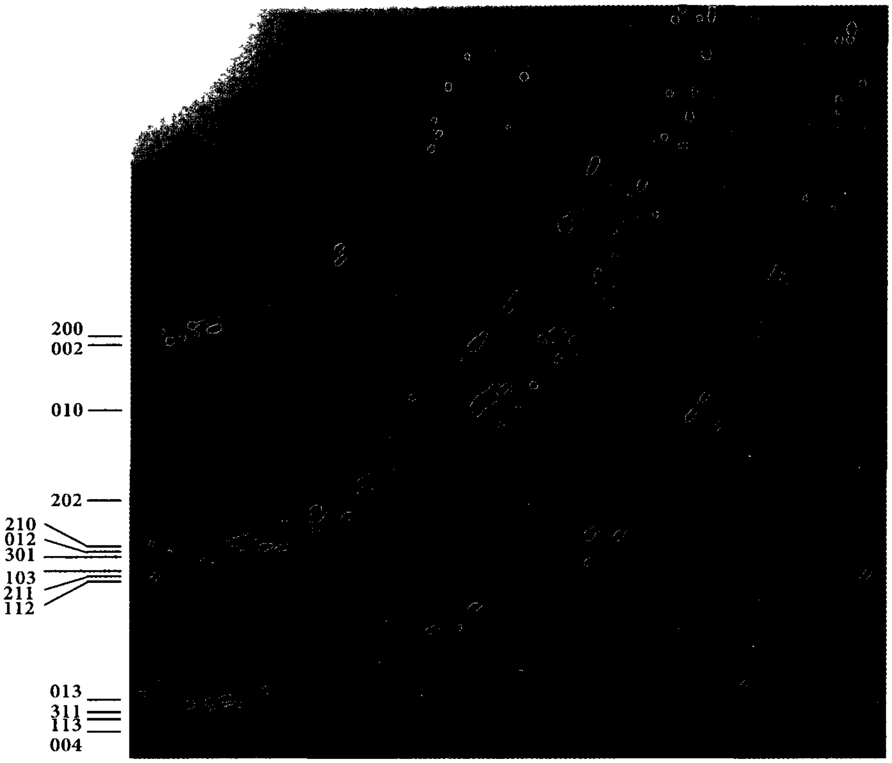

Figure 5.7: Small representative quadrant (equivalent to 0 < 2θ < 14°) of the diffraction image of ammonium azide at 0.7 GPa, showing the indexing of the observed Debye rings.

Note that, especially in comparison to cyanuric triazide, the observed Debye rings are much more "spotty" (i.e., the intensity is non-uniform along the ring). This indicates that ammonium azide sample is made of many small crystallites, and as such, is a poor powder. This is not unexpected since the ammonium azide sample was prepared from crushing a single crystal. While this had an inconsequential effect on the observed *d*-spacings, the observed diffraction intensities were significantly affected.

Once the image was integrated, the resulting diffraction pattern was fit using a full pattern Le Bail refinement (see Section 3.4.5). The observed x-ray diffraction peak (Bragg) positions were compared to those associated with the known orthorhombic *Pmna* unit cell of the ambient phase of AA. As seen in Figure 5.8, all the observed peaks are accounted for, with no obvious extraneous peaks. The extracted unit cell parameters are given in Table 5.4, and while they cannot be directly compared to the ambient cell parameters given in Table 5.3 due to the pressure difference, they are indeed consistent with the orthorhombic ambient phase.

Table 5.4: Extracted experimental unit cell parameters from the Le Bail fit and calculated volume of ammonium azide at 0.7 GPa (four molecules per unit cell)

a (Å)	b (Å)	c (Å)	V (Å^3)	ref.
8.8417(4)	3.7242(2)	8.6163(4)	283.72(2)	This work

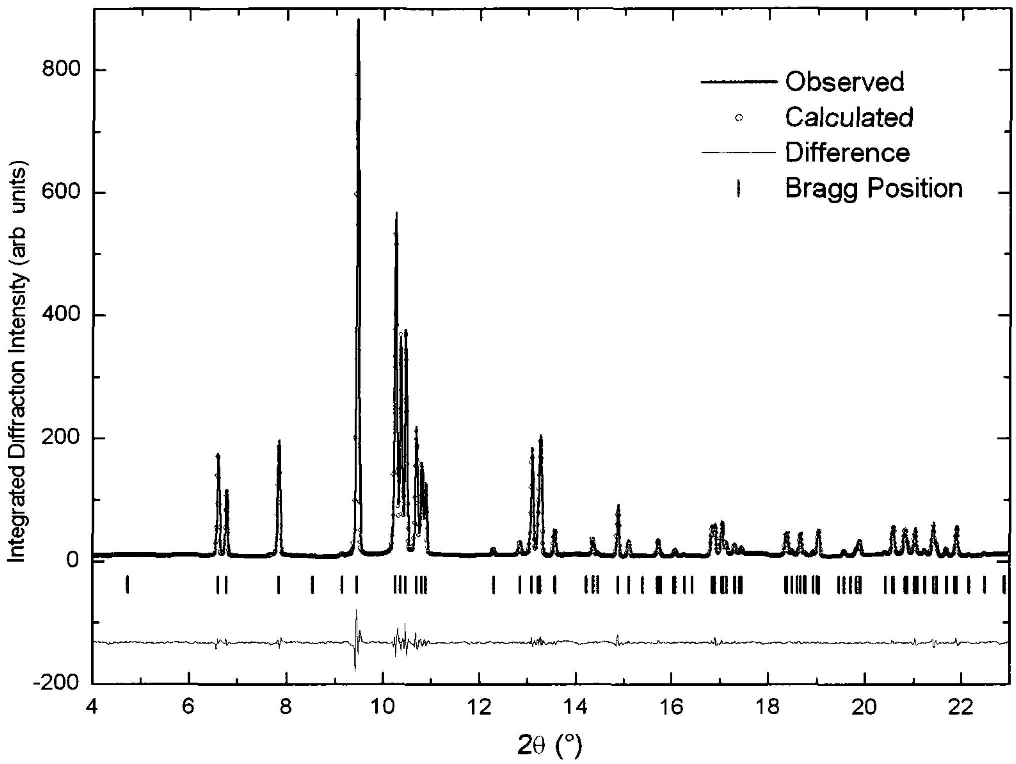

Figure 5.8: Results of Le Bail fit (red open circles) of x-ray diffraction data (black trace) of ammonium azide at 0.7GPa confirming the crystalline structure and purity of the sample. The blue trace is the difference in intensity between the calculated Le Bail fit and the observed intensities. Diffraction pattern was recorded at the Canadian Light Source.

5.4.2 Diffraction results as a function of pressure

Even though the Raman results indicated that no bonding rearrangement of ammonium azide takes place up to 65 GPa, powder x-ray diffraction experiments can still provide valuable information on the properties of AA. Three successful experiments were performed: one at low pressures ($P < 12$ GPa), and two at moderate pressures ($P < 30$ GPa). An overview of the results is given in Figure 5.9.

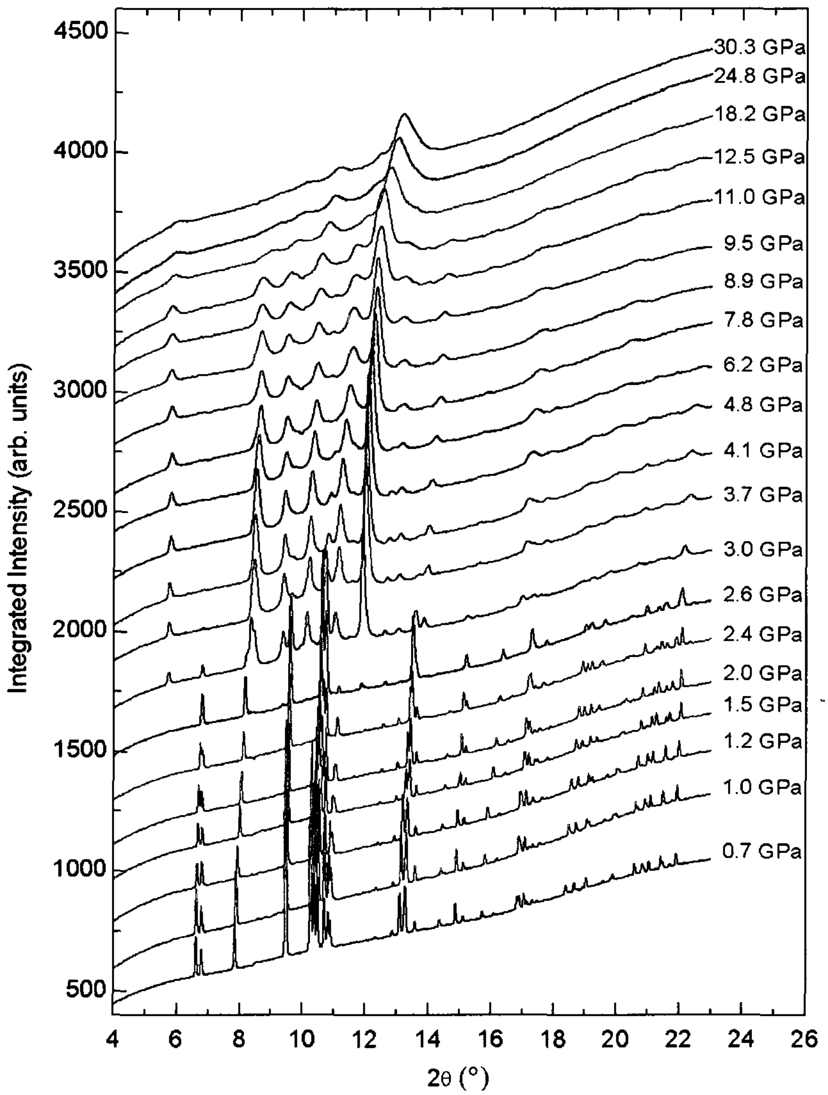

Figure 5.9: Evolution of the diffraction pattern of ammonium azide as a function of increasing external pressure showing a distinct pattern change at 3.0 GPa. Vertical offsets have been added for clarity.

The x-ray diffraction results surprisingly showed the occurrence of a structural phase transition at 3.0 GPa. While seemingly in contradiction to the Raman results, it should be recalled that the Raman band of diamond obscured most of the Raman modes of ammonium azide up to 3.5 GPa. Furthermore, it is possible that a structural transition occurred to a phase in which the bonding remains largely unchanged. The dramatic change in x-ray diffraction pattern through the phase transition can be seen in the overview given in Figure 5.9, and is highlighted in Figure 5.10.

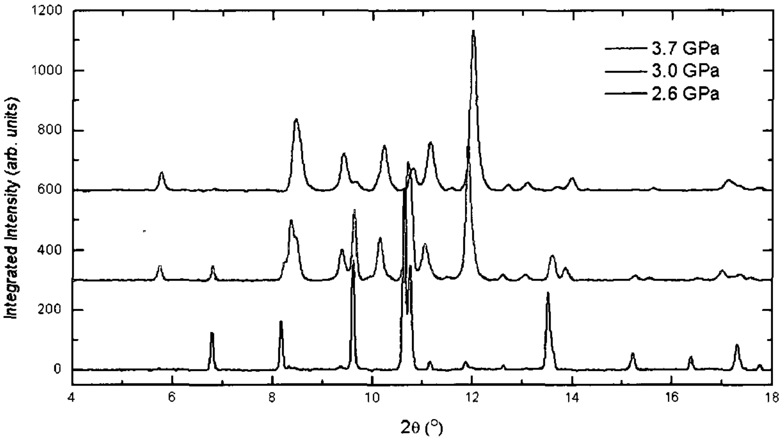

Figure 5.10: Selected region of the pressure evolution of the pXRD results highlighting the differences brought on by a phase transition at 3.0 GPa. Very small hints of the new phase appear in the bottom trace (black) at 2.6 GPa, the middle trace (red) at 3.0 GPa presents a mixture of both phases, and the top trace (blue) at 3.7 GPa is predominately the new phase with some persistence of the ambient pressure phase.

Weak hints of the most intense reflections of the new dense phase of ammonium azide began to appear at 2.6 GPa, by 3.0 GPa there was a nearly equal phase mixture, and at 3.7 GPa only the strongest reflections of the ambient phase were present. These strong reflections of the ambient phase persisted up to 5.8 GPa. These trends are most easily seen by following the observed *d*-spacings with increasing pressure. Such a plot is given below in Figure 5.11, which clearly identifies a phase transition along with the persistence of the ambient phase. Further investigations of the low pressure and high pressure phases are presented in the following two subsections.

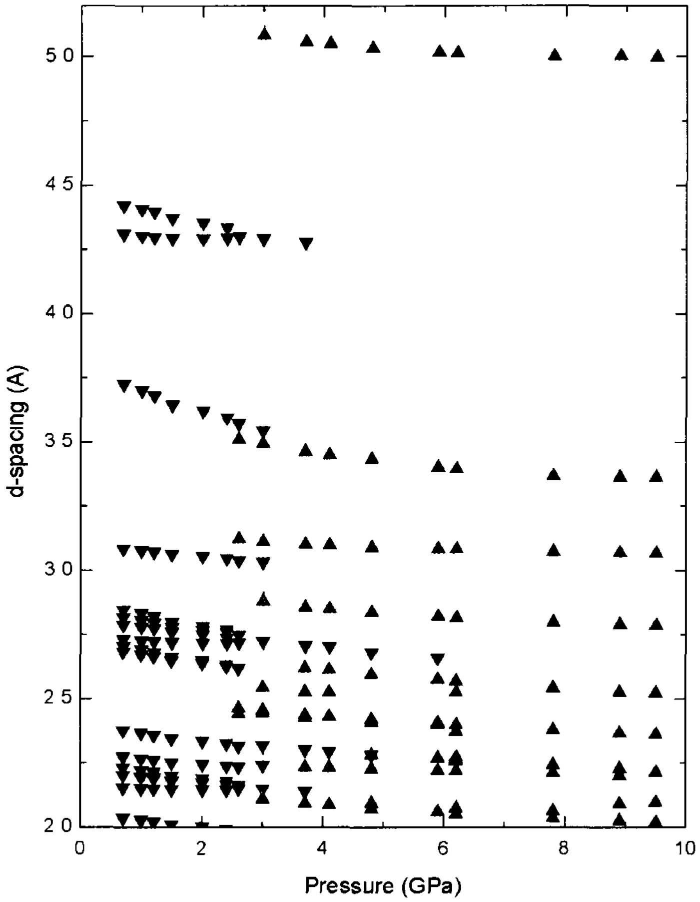

Figure 5.11: Evolution of the observed *d*-spacings of ammonium azide with up to 10 GPa showing the occurrence of a structure phase transition at 3.0 GPa, and the persistence of the low pressure phase up to 5.8 GPa.

5.4.3 Low pressure phase

The ambient pressure structure is stable up to 3.0 GPa, and persists up to approximately 6 GPa, and will henceforth be referred to as phase I. By examining how the orthorhombic unit cell associated with this phase changes with pressure, properties of the material can be extracted. Due to the small pressure range over which this phase is stable, the second-order Birch-Murnaghan equation of state was used to model the phase behaviour (see section 2.5.2). The experimental fit is shown in Figure 5.12 and the resulting parameters are given in Table 5.5.

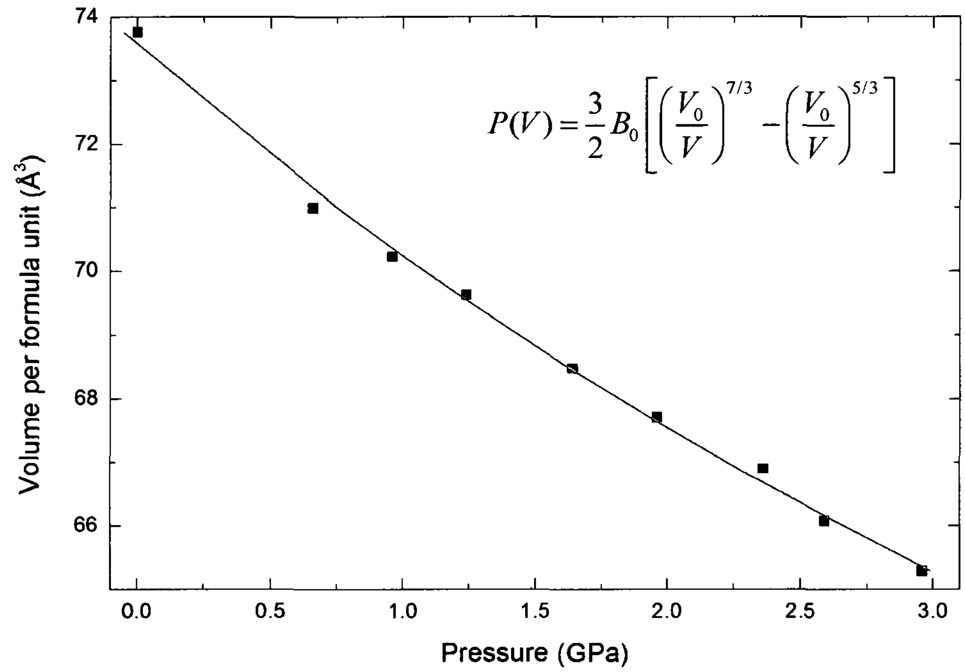

Figure 5.12: Modeling the unit cell volume of phase I of ammonium azide using the second-order Birch-Murnaghan equation of state (inset). The resulting best fit is given by the solid line with parameters given in Table 5.5.

Table 5.5: Parameters extracted from EOS fit of phase I of ammonium azide

Bulk modulus, B_0 (GPa)	**Pressure derivative of bulk modulus, B'_0**	**Initial volume per formula unit, V_0 (Å^3)**	**Initial unit cell volume (Å^3)**
19.8	4 (fixed)	73.6	294.4

Ammonium azide is shown to have a fairly small bulk modulus, and therefore, is a rather compressible material. The extracted initial unit cell volume is consistent with the known ambient pressure volume (Table 5.3).

5.4.4 High pressure phase

Strain induced broadening, along with hysteresis of phase I, made the structural identification of the new high pressure phase of ammonium azide (henceforth referred to as phase II) difficult. Since ammonium azide has a low melting point (160 °C at ambient pressure [10]) and the phase transition occurs at a relatively low pressure, heating the sample in the diamond anvil cell to even moderate temperatures can anneal the material. Annealing a sample can relax the strain within the sample which reduces the diffraction line width, and can also homogenize the sample, which reduces the hysteresis of the low pressure phase. This process is thus highly beneficial in identifying the structure, as the peaks belonging to phase II can be distinguished and more clearly resolved. Annealing experiments of phase II of ammonium azide were performed by placing the entire diamond anvil cell in at oven at approximately 140 °C for 8 - 12 hours. The effect of annealing on phase II of AA is shown in Figure 5.13.

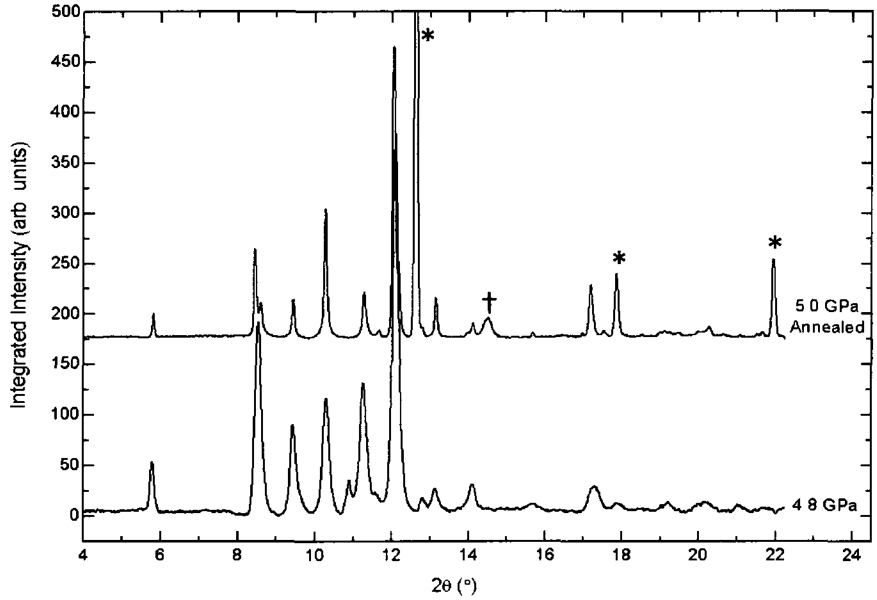

Figure 5.13: Effect of annealing on phase II of ammonium azide. The annealed sample (top trace, blue) contains water contaminant as indicated by diffraction resulting from Ice VII (*). Diffraction resulting from the gasket material is also observed in the annealed sample (†).

With significant help from the diffraction data from the annealed sample, the proposed unit cell for this new dense phase II of ammonium azide is a monoclinic cell (space group *P*2) with two molecules per unit cell. The unit cell fit provided an excellent match to the observed patterns. An example of one such fit, for an annealed sample with a measured pressure of 2.8 GPa, is given in Table 5.6.

Table 5.6: Results of a monoclinic unit cell fit of ammonium azide at 2.8 GPa (annealed) for $2\theta < 20°$

(*hkl*)	**2θ observed (°)**	***d*-spacing observed (Å)**	***d*-spacing calculated (Å)**	**Difference d_{obs}-d_{calc} (Å)**
200	5.709	5.1126	5.1120	0.0006
010	8.320	3.5095	3.5097	-0.0002
10-1	8.440	3.4597	3.4600	-0.0003
101	9.359	3.1205	3.1204	0.0001
210	10.096	2.8935	2.8934	0.0001
30-1	10.972	2.6630	2.6632	-0.0002
400	11.435	2.5554	2.5559	-0.0005
11-1	11.858	2.4646	2.4640	0.0006
310	11.958	2.4440	2.4450	-0.0010
21-1	12.533	2.3325	2.3323	0.0002
40-1	13.018	2.2459	2.2457	0.0002
31-1	13.783	2.1217	2.1220	-0.0003
410	14.156	2.0661	2.0661	0.0000
41-1	15.471	1.8915	1.8916	-0.0001
10-2	16.678	1.7554	1.7552	0.0002
20-2	16.926	1.7300	1.7301	-0.0001
600	17.189	1.7036	1.7040	-0.0004
411	17.476	1.6758	1.6757	0.0001
30-2	17.644	1.6600	1.6602	-0.0002
11-2	18.670	1.5695	1.5698	-0.0003
12-1	18.719	1.5655	1.5651	0.0004
40-2	18.781	1.5604	1.5606	-0.0002
21-2	18.884	1.5519	1.5517	0.0002
22-1	19.157	1.5300	1.5297	0.0003
31-2	19.534	1.5007	1.5007	0.0000
511	19.711	1.4874	1.4877	-0.0003

To further refine the unit cell parameters and to compare the expected diffraction peak (Bragg) positions of the proposed monoclinic cell (space group *P*2) with the observed peaks, the full pattern was fit using Le Bail refinement. The Le Bail fit is shown graphically in Figure 5.14, and the extracted unit cell parameters and volume are given in Table 5.7.

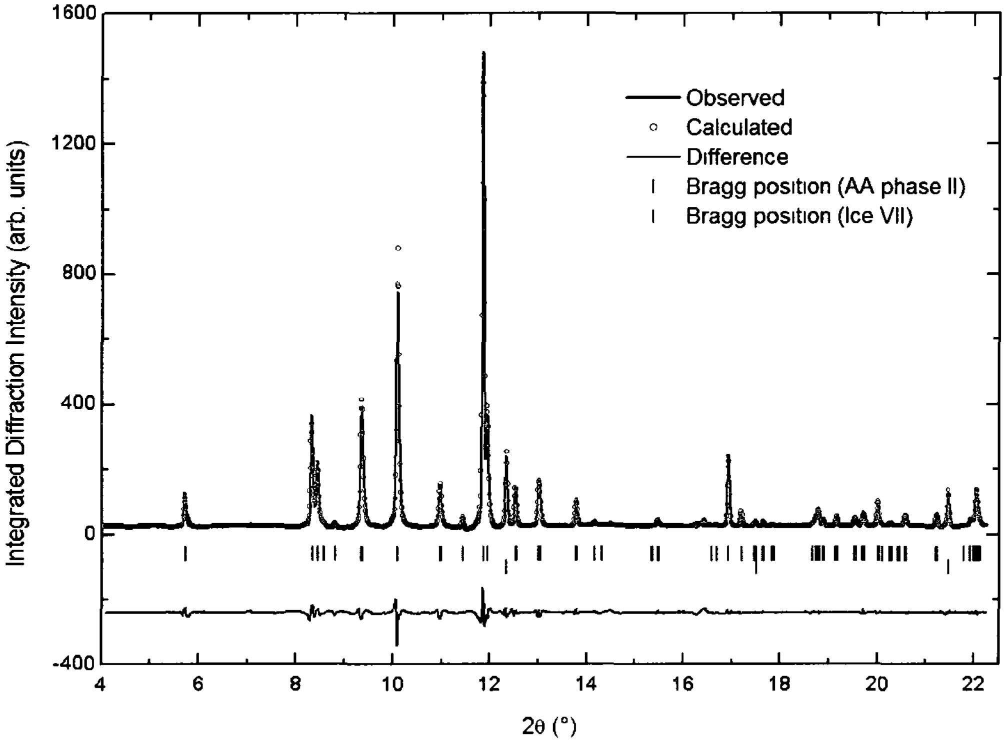

Figure 5.14: Results of the Le Bail fit (open red circles) of x-ray diffraction data (black trace) of phase II of ammonium azide at 2.8 GPa after being annealed. The blue trace is the difference in intensity between the calculated Le Bail fit and the observed intensities. The green and pink bars represent the Bragg positions for phase II of AA and Ice VII, respectively.

Table 5.7: Extracted experimental unit cell parameters and calculated volume from the Le Bail fit of phase II of ammonium azide at 2.8 GPa after being annealed (two molecules per unit cell)

Pressure (GPa)	a (Å)	b (Å)	c (Å)	β (°)	V (Å^3)
2.8	10.3742(7)	3.5093(2)	3.5109(2)	99.891(7)	125.92(1)

It is seen in Figure 5.14 that all the observed peaks are accounted for by either the proposed monoclinic cell or the known water contaminate (at 2.8 GPa and ambient temperature, water exists in the cubic Ice VII phase), and there are only very few expected reflections which were not observed.

With the unit cell determined using the data acquired from annealed sample, the pressure sequence shown in Figure 5.9 was analyzed accordingly in order to study the evolution of this monoclinic cell upon increasing pressure. The generated P,V curve from this data was fit using a third-order Birch-Murnaghan equation of state (see section 2.5.2) to extract the bulk modulus and the pressure derivative of the bulk modulus. The experimental fit is shown in Figure 5.15 and the resultant parameters are given in Table 5.8

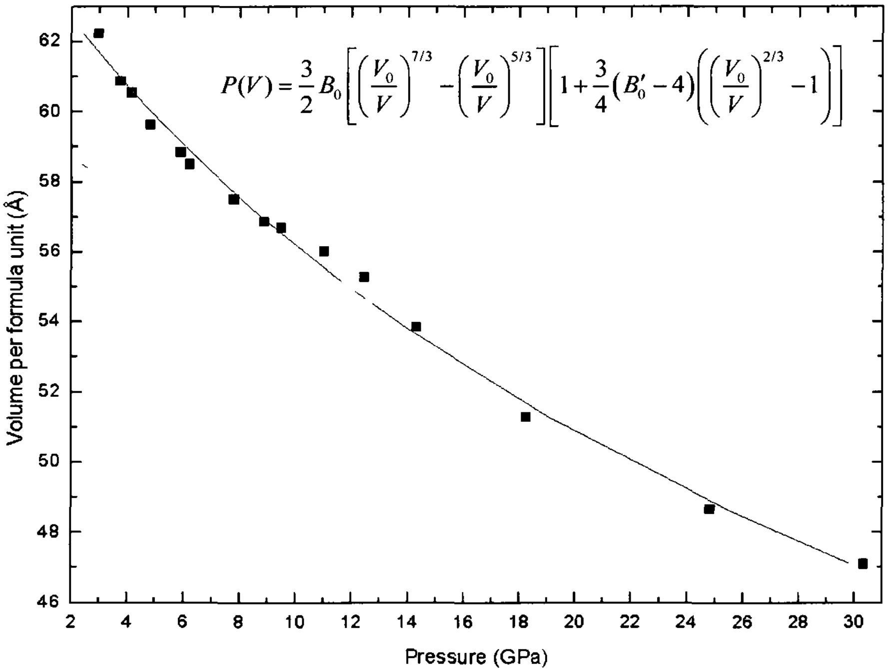

Figure 5.15: Modeling the unit cell volume of phase II of ammonium azide using the third-order Birch-Murnaghan equation of state (inset). The resulting best fit is given by the solid line with parameters given in Table 5.8.

Table 5.8: Parameters extracted from EOS fit of phase II of ammonium azide

Bulk modulus, B_0 (GPa)	**Pressure derivative of bulk modulus, B'_0**	**Initial volume per formula unit, V_0 (Å^3)**
54.6	3.4	64.86

The above data on phase II was combined with the results from the analysis of phase I of ammonium azide to provide a full P,V plot of ammonium azide that clearly shows the phase transition and highlights the difference between the two phases. Such a plot is given in Figure 5.16. The transitional volume collapse was calculated using the unit cell volumes of the two phases which are both present in the x-ray diffraction pattern acquired at 3.0 GPa (middle (red) trace in Figure 5.10), and was found to be 4.8%.

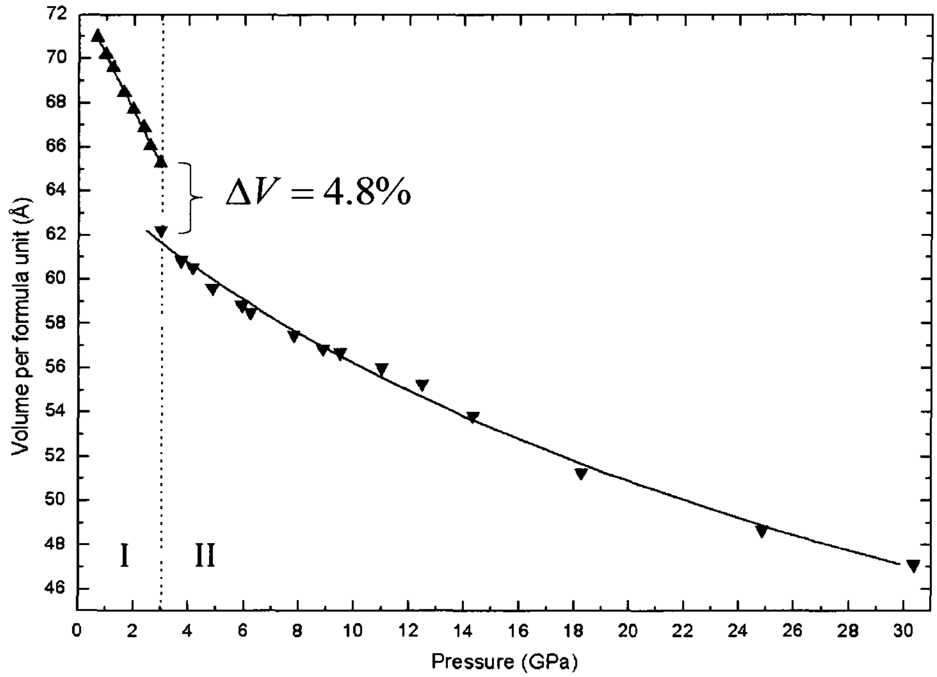

Figure 5.16: Experimental P,V curve of ammonium azide . The transitional volume collapse is shown and calculated to be 4.8%.

The acquired powder x-ray diffraction data for phase II of ammonium azide was successful in determining the unit cell and space group (monoclinic, *P*2), but could not provide information on the atomic positions within the unit cell. This information is typically determined using a Rietveld refinement where the observed diffraction intensities are used to determine the atomic structure. However, with high pressure powder x-ray diffraction this is not always possible; challenges such as preferred orientation and poor powder averaging can result in x-ray diffraction intensities not representative of the crystalline structure.

Without adequate intensity information for a Rietveld refinement, the atomic positions can be determined using quantum mechanical calculations. In the case of ammonium azide, *ab initio* calculations were performed[§] by constraining the unit cell to the experimentally determined parameters, while allowing the atoms to assume the lowest enthalpy arrangement. The resulting energy-optimized phase II atomic structure at a pressure of 5.0 GPa is shown in Figure 5.17. In this structure, the azide group has slightly deviated from linearity, with the N-N-N bond angle measuring 177.7° and the two N-N bond distances measuring 1.202 Å and 1.200 Å. The N-H distance in the ammonium cation measures 1.054 Å, while the N-H···N hydrogen bond distance varies from 1.813 to 1.859 Å.

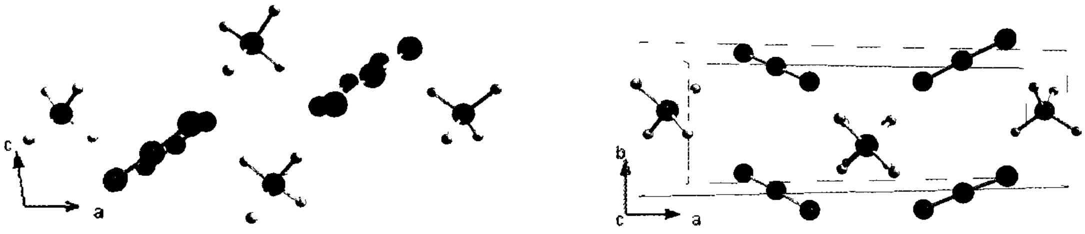

Figure 5.17: Crystal structure of phase II of ammonium azide at 5.0 GPa determined by *ab initio* calculations performed by Hu [11]. The blue and white molecules represent nitrogen and hydrogen, respectively. Left: view along the **b** axis. Right: view along the **c** axis.

[§] All calculations were performed by Dr. Anguang Hu, scientist (Defence Research and Development Canada - Suffield; Medicine Hat, Alberta)

This structure was then used to calculate the expected reflection intensities which were then compared to the observed pattern. As is shown in Figure 5.18, the intensities resulting from calculated atomic structure correctly account for the unobserved reflections seen in Figure 5.14 (in particular, those between 8.5° < 2θ < 9°). There are some notable discrepancies between the observed and calculated intensities (especially between 9° < 2θ < 12°); however, as previously discussed, the observed intensities for high pressure powder x-ray diffraction experiments are prone to inaccuracy.

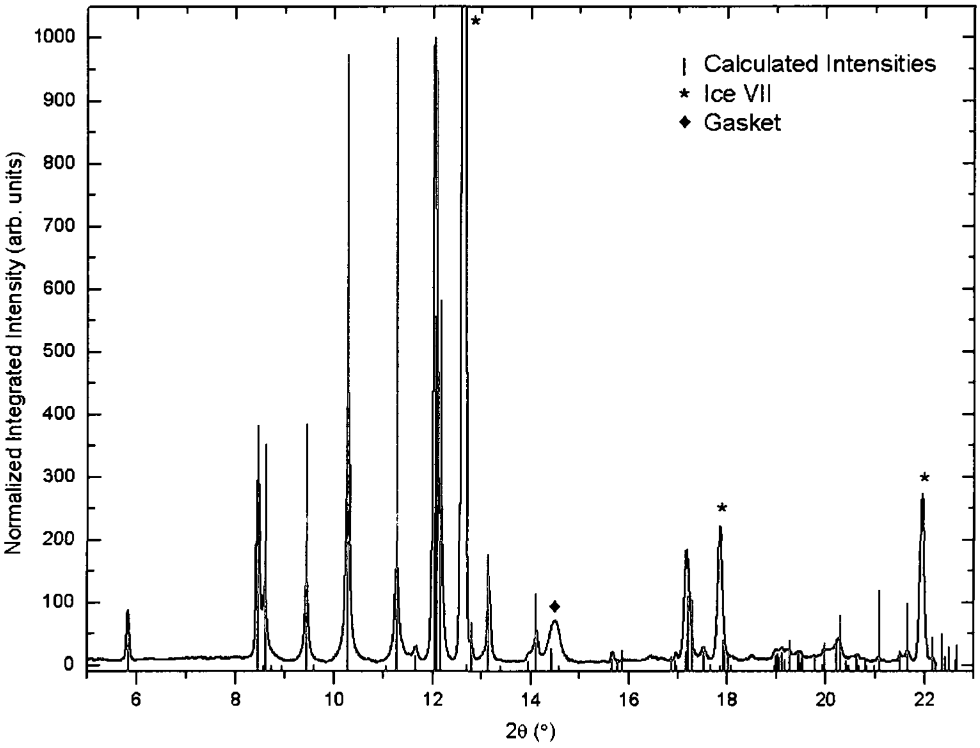

Figure 5.18: Comparison of calculated reflection intensities (red vertical bars) with experimentally observed x-ray diffraction pattern (black trace) of phase II of AA at 5.0 GPa.

5.4.5 Decompression studies

The pressure on ammonium azide was incrementally decreased starting from 30.3 GPa to allow for a study of the behaviour of phase II upon decompression. The recorded diffraction patterns are shown in Figure 5.19.

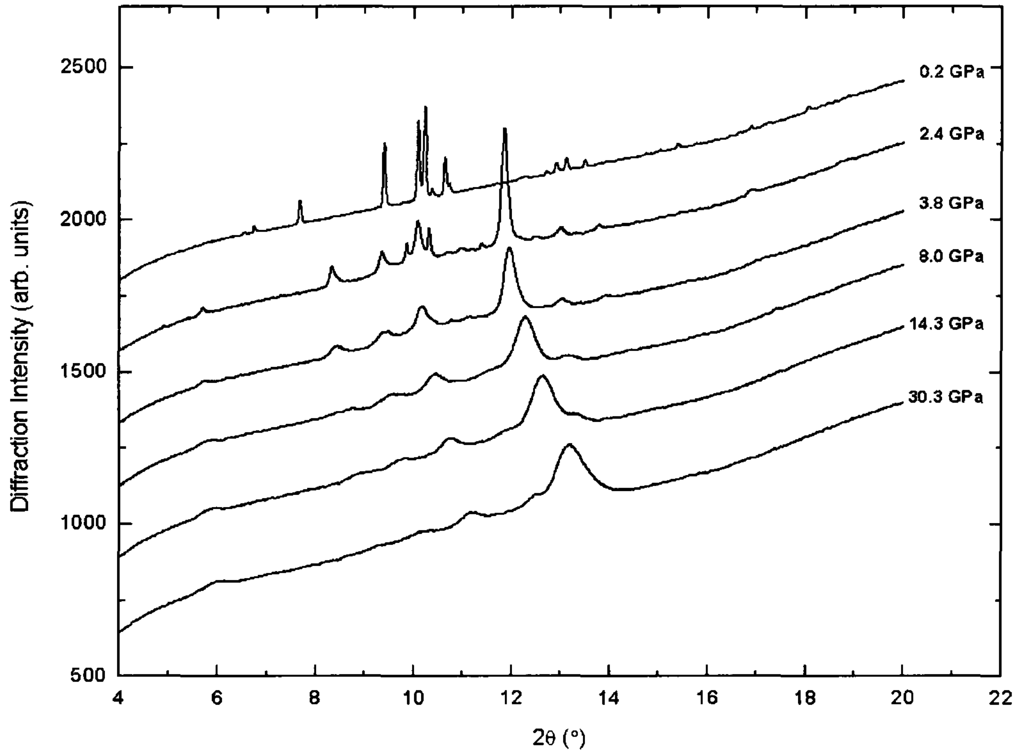

Figure 5.19: Powder x-ray diffraction patterns of ammonium azide upon decreasing pressure. Experiment started at 30.3 GPa (bottom trace) and ended at 0.2 GPa (top trace). It is clearly seen that the transformation from phase II back to phase I has begun at 2.4 GPa and is complete at 0.2 GPa.

Some hysteresis of phase II was observed but the transition was found to be reversible. Upon compression the transition occurred at 3.0 GPa, but the decompression results presented above show the transformation back to phase I had only begun at 2.4 GPa (diffraction profile shows a mixture of phase I and phase II), and was complete at 0.2 GPa.

5.5 Discussion

5.5.1 Phase transition

The powder x-ray diffraction results showed a pressure-induced first order phase transition at 3.0 GPa; however, examining the evolution of the Raman modes upon increasing pressure show no indication of a phase transition. The $2\nu_2^-$ modes exhibit smooth increases in frequency through the known transition. This suggests that the content of the unit cell and the center of symmetry remain unchanged. When investigating the computationally determined structure of phase II (Figure 5.17), the azide and ammonium ions remain intact and no major bonding rearrangement has occurred, which supports the observation of an unchanged Raman spectrum.

In terms of bonding, the differences between the orthorhombic phase I and the monoclinic phase II are minimal. The azide N-N bond lengthened slightly, from 1.17 Å to 1.20 Å, and the hydrogen bond distances shortened, from 1.94 - 1.98 Å to 1.81 - 1.86 Å. Structurally, the phase I - phase II transition sees the unit cell go from having four to two molecules per unit cell, and is accompanied by a 4.8% collapse in volume per formula unit. As seen by comparing Figure 5.6 and Figure 5.17, phase II retains the azide herringbone arrangement seen in phase I, but there are no longer any azide groups which lie parallel to the unit cell edges, they all make up part of the zigzag structure.

Associated with the phase transition was a change in material properties. Phase I was found to be compressible and have a bulk modulus of 19.8 GPa. This is very typical of ionic compounds; for example, lithium azide (LiN_3) and sodium chloride (NaCl) have bulk moduli of 19.1 and 23.84 GPa, respectively [12, 13]. As seen graphically in Figure 5.16, phase II of ammonium azide is less compressible than phase I, as indicated by a bulk modulus of 54.6 GPa. This decrease in compressibility is characteristic of a transition to a denser phase.

5.5.2 Phase II

Upon examination of the P,V curve of phase II of ammonium azide (Figure 5.15), it is seen that the curve is not smooth; between approximately 10 and 12 GPa the curvature notably changes. It is unclear if this discontinuity is a genuine property of ammonium azide, which perhaps indicates a very subtle monoclinic-to-monoclinic phase transition; or, if it is an artefact resulting from poor diffraction patterns. As seen in Figure 5.9, the observed diffraction peaks broaden and lose intensity due to non-hydrostatic pressure conditions and thinning of the sample. This results in very few reflections being used in the unit cell fit, and, especially when multiple reflections are contributing to one observed peak, this can lead to difficulties in the unit cell determination. Even with the discontinuity, the observed P,V data was successfully modeled using a third-order Birch-Murnaghan equation of state. The largest observed deviation in unit cell volume was 1.2 Å^3 at 12.5 GPa, which is only a difference of 1%. Therefore it is not unreasonable to associate the discontinuity with an artefact of the data processing.

However, one interesting observation is that the occurrence of this discontinuity coincides with the switching of intensity between the N_3^- stretching modes in the Raman spectrum (see Figure 5.5). While this may simply be a coincidence, it certainly suggests that the discontinuity in the P,V data of phase II is indeed a genuine property of ammonium azide. Though without improved x-ray diffraction data, any conclusion on the merit of the observed P,V discontinuity is premature.

Assuming that the discontinuity is not due to a phase transition, phase II of ammonium azide is stable up to at least 65 GPa, as shown by x-ray diffraction and Raman spectroscopy results. While phase II is indeed a novel phase of ammonium azide, it does not contain the sought-after single-bonded nitrogen network of the hydronitrogen solid. Furthermore, despite some hysteresis, it is not recoverable at ambient conditions. Of course, that is not to say that the hydronitrogen solid is not attainable starting from ammonium azide, it was just not observed within the experimental parameters of this work (ambient temperature, $P < 65$ GPa).

References

[1] Jared B. Ledgard, *The preparatory manual of explosives*, 3rd ed. (Jared Ledgard, USA, 2007).

[2] P. Gray and T.C. Waddington, *Trans. Faraday Soc.* **53**, 901 (1957).

[3] W.L. Ng and J.E. Field, *Thermochimica Acta* **84**, 133 (1985).

[4] Linus Pauling, *The Nature of the Chemical Bond*, 2nd ed. (Cornell University Press, Ithaca, New York, 1940).

[5] D.A. Dows, E. Whittle, and G.C. Pimentel, *J. Chem. Phys.* **23**, 1475 (1955).

[6] Z. Iqbal and M.L. Malhotra, *Spectro. Acta* **27A**, 441 (1971).

[7] G. Herzberg, *The Infrared and Raman Spectra of Polyatomic Molecules* (Van Nostrand, New York, 1945).

[8] L.K. Frevel, *Zeit. für Kristallograph., Kristallgeo., Kristallphys., Kristallchem.* **94**, 197 (1936).

[9] E. Prince and C.S. Choi, *Acta Crys. B* **34**, 2606 (1978).

[10] G.S. Yakovleva, R. Kh. Kurbangalina, L.N. Stesik, *Combust. Explo. Shock Waves* **13**, 405 (1977).

[11] A. Hu, personal communication (August 2010).

[12] S.A. Medvedev, I.A. Trojan, T. Palasyuk, T.M. Klapötke, J. Evers, *J. Phys.: Condens. Matter* **21**, 195404 (2009).

[13] H. Spetzler, C.G. Sammis, R.J. O'Connell, *J. Phys. Chem. Solids* **33**, 1727 (1972).

Chapter 6

Summary and Future Work

Both vibrational Raman spectroscopy and powder x-ray diffraction experiments performed on cyanuric triazide identified a first order structural phase transition between 30 and 32 GPa. The low pressure phase (phase I) is the well-known ambient hexagonal structure, is highly compressible, and stiffens rapidly with increasing pressure. Due to non-hydrostatic pressure conditions, extreme line broadening precluded a definite structural solution to the newly identified high pressure phase (phase II) that is stable up to at least 60 GPa. Two unit cells for phase II were proposed, one hexagonal and one orthorhombic, each with their own merits. However, any conclusion on the structure of phase II was not possible, and requires further investigations. Despite a large hysteresis, upon decompression the dense phase transformed back to phase I at approximately 13 GPa. This suggests that the sought-after C_3N_{12} solid, characterized by sp^3 carbon and single-bonded nitrogen, was not achieved upon compression to 60 GPa. However, without further investigations, it cannot be ruled out as a possible characterization of phase II. A summary of these conclusions is presented in Table 6.1.

Similar experiments were performed on ammonium azide, and identified a reversible first order structural phase transition at 3.0 GPa. The low pressure phase (phase I) is the well-known ambient orthorhombic structure, and was found to be quite compressible. The novel high pressure phase (phase II) is a less-compressible, monoclinic structure that is not associated with either the formation of the $(NH)_4$ hydronitrogen solid, or the trans-2-tetrazene isomer. Powder x-ray diffraction data showed phase II to be stable up to at least 30 GPa, and Raman data further suggested that it is stable up to at least 65 GPa. A summary of these conclusions is presented in Table 6.1.

Table 6.1: Summary of x-ray diffraction experimental results for CTA and AA

		CTA	**AA**
Phase I	**Bravais Lattice**	Hexagonal	Orthorhombic
	B_0 (GPa)	10.5	19.8
	B_0'	7.9	4†
	V_0 (Å^3)	199.8	73.6
	Pressure range observed (GPa)	ambient - 30.0	ambient - 5.6
Phase II	**Bravais Lattice**	Hexagonal/ Orthorhombic ‡	Monoclinic
	B_0 (GPa)		54.6
	B_0'		3.4
	V_0 (Å^3)		64.86
	Pressure range observed (GPa)	32.6 - 59.2	3.0 - 30.3
Compression Transition Pressure (GPa)		30 - 32.6	3.0
Transition Volume Collapse		17% / 21% ‡	4.8%
Decompression Transition Pressure (GPa)		13.8 - 8.2	2.4 - 0.2

† Fixed (second-order Birch-Murnaghan EOS fit)

‡ Proposed solutions (insufficient data to allow definite characterization)

While the ultimate goal of recovering single-bonded nitrogen at ambient conditions was not achieved, the story of cyanuric triazide and ammonium azide is far from complete. A specialized apparatus is currently being constructed which will allow for the loading of gases such as helium at high densities up to 0.2 GPa, for use as a pressure transmitting medium. This will allow for the study of compounds at very high pressures ($P > 100$ GPa) under hydrostatic conditions, which is highly beneficial for unit cell determination, as the strain-induced broadening of the x-ray diffraction peaks would be substantially reduced. It would also result in more accurate determinations of material properties such as the bulk modulus (equations of state used to extract these parameters assume hydrostatic compression). In regards to the compounds studied in this work, it would be of significant value in determining the unit cell of the high pressure phase of cyanuric triazide, and for resolving the discontinuity in the P,V curve of the high pressure phase of ammonium azide.

A laser heating system is also currently being constructed which uses two 100 W near-IR fibre lasers that will allow for combined high pressure ($P > 100$ GPa), high temperature ($T > 2000$ K) experiments. For both pure nitrogen (N_2) and sodium azide (NaN_3), the single-bonded nitrogen network was only formed upon the application of high temperatures at high pressure. Furthermore, large thermal barriers were found to inhibit the transformation of CTA and AA into their predicted structures containing single-bonded nitrogen. It was predicted that the combination of high pressures and high temperatures would facilitate these transformations. And thus, besides being an entirely new thermodynamic variable to explore, high temperatures represent an exceptional tool to use in working towards the goal of recovering single-bonded nitrogen. Even if the use of laser heating does not bring about any novel phase transformations, it can used to anneal the sample. As was seen for phase II of ammonium azide, annealing can make a substantial difference in the diffraction pattern quality, which makes for an easier, and more convincing, structural determination.

Naturally, cyanuric triazide and ammonium azide are not the only two candidate materials for high pressure synthesis of polymeric nitrogen, and using high nitrogen content energetic materials as precursors is only one avenue towards the ultimate goal. Compounds like trans-2-tetrazene, or any of the many novel high nitrogen content energetic materials; gas mixtures like nitrogen - ammonia (N_2 - NH_3), or nitrogen - hydrazine (N_2 - N_2H_4); or exploring the use of introducing small dopant molecules to pure N_2 to act as stabilizers or catalysts; represent only a very small fraction of what could be on the horizon for polymeric nitrogen research.

On a personal note, I strongly believe that since the goal of recovering single-bonded nitrogen at ambient conditions is in its relative infancy, that the next few years will be a very dynamic and vibrant time. Be it theoretical or experimental, I can only hope this challenge captivates the scientific community as much as it has myself.

Appendix A

Copyright Permissions

Figure 2.2

Copyright (1986) by The American Physical Society.

Figure 2.3 (a), (b); Figure 2.4

Reprinted by permission from Macmillan Publishers Ltd: Nature Materials (*Nat. Mat.* **3**, 558 (2004)), copyright (2004).

License Number: 2550870462175

Figure 2.3 (c)

Reprinted with permission from *App. Phys. Lett*.**93**, 091907 (2008). Copyright 2008, American Institute of Physics.

Licence Number: 255870854478

Figure 2.5

Copyright (2008), U.S. Army Research Laboratory. ATTN: AMSRD-ARL-WM-BD (Jennifer A. Ciezak).

Figure 4.9

Reprinted with permission from *J. Chem. Phys.* **48**, 1138 (1968). Copyright 1968, American Institute of Physics.

Licence Number: 2550870968191

Figure 4.15

Reprinted by permission from Macmillan Publishers Ltd: Nature (*Nature* **134**, 138 (1934)), copyright (1934).

License Number: 2550870589921

Figure 5.2

Reprinted from *Spectrochimica Acta* **27A**, 441 (1971), Copyright (1971), with permission from Elsevier.

Licence Number: 2550820564668